EX - CON

CARDEN

SAND74-8017

Unlimited Release-Patent Caution

Status Report on a High Temperature Solar Energy System

A. C. Skinrood, T. D. Brumleve, C. T. Schafer, C. T. Yokomizo, C. M. Leonard, Jr.

Prepared by Sandia Laboratories, Albuquerque, New Mexico 87115 and Livermore, California 94550 for the United States Atomic Energy Commission under Contract AT (29-1)-789

Printed September 1974

Sandia Laboratories
energy report

Issued by Sandia Laboratories, operated for the United States Energy Research and Development Administration by Sandia Corporation.

SAND74-8017
Unlimited Release - Patent Caution
Printed September 1974

STATUS REPORT ON A HIGH TEMPERATURE SOLAR ENERGY SYSTEM

A. C. Skinrood
T. D. Brumleve
C. T. Schafer
C. T. Yokomizo
C. M. Leonard, Jr.

ACKNOWLEDGMENTS

Many of the Sandia Laboratories staff assisted in particular studies, fabrications, and experiments. Major contributors to this report were J. D. Hankins, C. A. Loveless, D. K. Ottesen, and M. Abrams. Editorial assistance was provided by P. Dean. Members of the staff of Bechtel Corporation provided design and cost information on towers, power plants, and siting.

CONTENTS

ILLUSTRATIONS

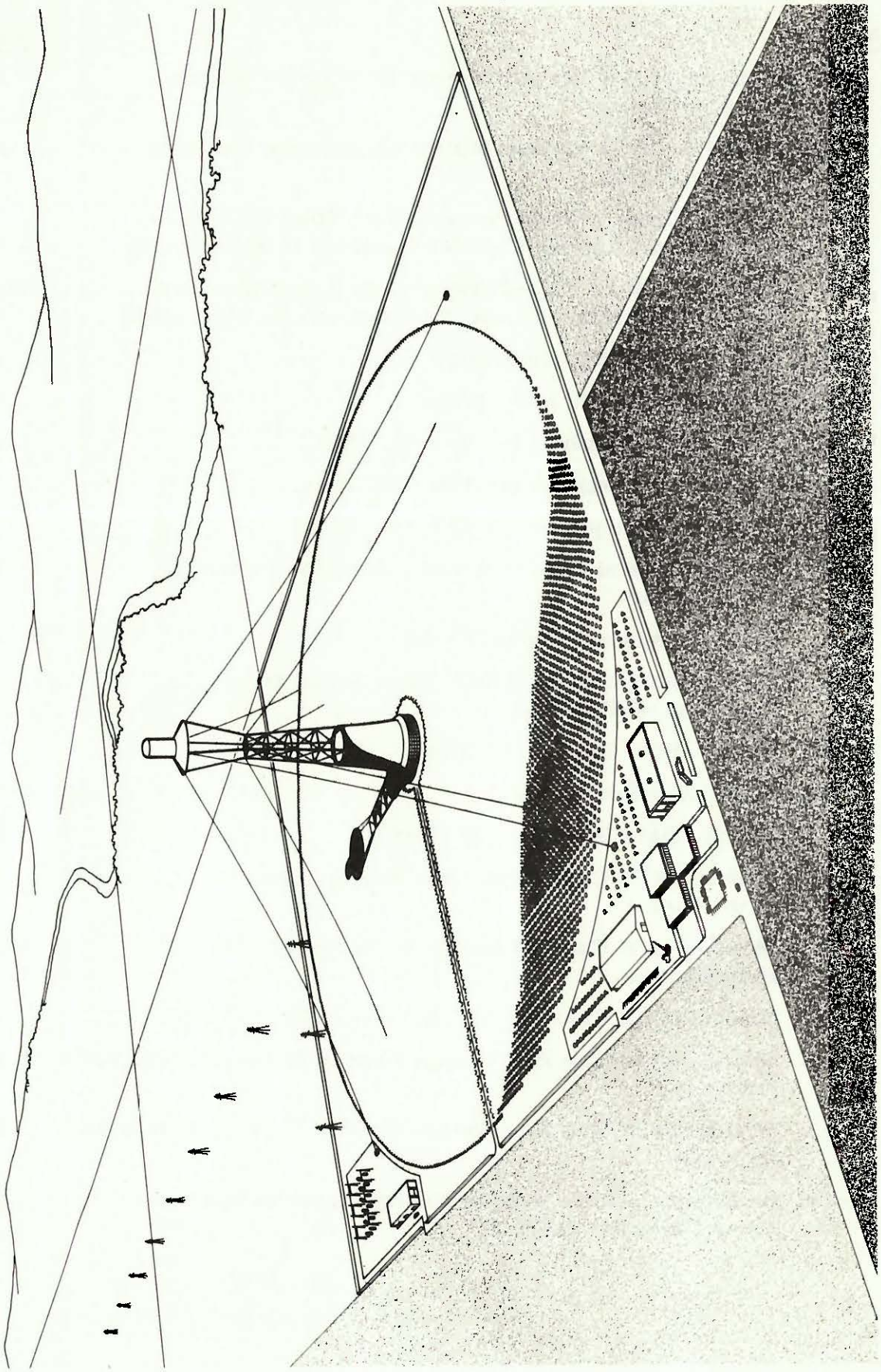

ABSTRACT

A system for collecting large quantities of solar energy at temperatures above 490°C has been under investigation since late 1972 for applications such as electrical power generation, chemical processing, and other industrial uses which benefit from high temperatures and for processes requiring clean energy. The system consists of a large array of individually controlled, nearly flat mirrors which direct solar energy into a well insulated optical cavity absorber located at the top of a centrally located tower. Highly concentrated solar flux enters the cavity from the bottom through a windowless aperture and is absorbed in a working fluid. Results of studies by Sandia Laboratories, Livermore, California are summarized and future investigations are outlined. Emphasized is development of an efficient energy absorbing system for electrical power generation, and design considerations for a working system to verify performance calculations.

The proposed energy absorbing system has several features which offer the prospect of relatively high system efficiency. Its features are:

1. High flux densities are accommodated by direct absorption in the working fluid.

2. Aperture size and thus radiation loss is reduced by the use of a terminal concentrator.

3. Convection losses are minimized by a vertically oriented cavity configuration.

4. No window is required, thus avoiding reflective and absorptive energy losses and operational problems.

Overall system efficiency is high since thermal energy is collected at relatively high temperature (~495°C). Economic studies indicate that in areas of the U.S. which have high insolation, at a mirror cost of $20 to $40 per m^2, the system may be interesting when fossil fuel costs get to about $2.00 per million Btu. Ultimate selection of design characteristics must be based on trade-off studies of a large number of system parameters, experimental results, manufacturing considerations, and economic evaluations.

An early systems experiment is an important element of the program. A meaningful size model (1 to 10 MW_e) will be designed which would involve 4-40 acres of mirrors along with associated hardware. If early development activities continue to look favorable, we would propose construction and evaluation of such a system. Operational data would then be obtained and compared to analytical performance predictions.

1.0 Background and Objectives

In view of the nation's and the world's growing concern with environmental and health/safety factors as well as our limited supply of petroleum and gaseous fuels, it is important to evaluate the potential impact of solar energy use since it is an inexhaustible source of clean energy widely available throughout the world.

This report summarizes the status of a Sandia Laboratories study of a solar energy collection method as an alternate source of high temperature energy for electrical power generation and industrial applications. Although in principle, solar energy could be utilized for almost any energy need now being met by conventional fuels, the diffuse nature of solar energy has made the cost of collection and utilization noncompetitive on an economic basis. We will explore several technical approaches to determine if this can be changed by technology and science.

2.0 System Description and Summary of Investigations

The system is conceived as a large array of individually controlled mirrors which direct solar energy into a well-insulated optical cavity absorber located at the top of a tower. Highly concentrated solar flux enters the cavity from the bottom through a windowless aperture and is absorbed in a working fluid (Figure 2-1. The energy is then transported by the fluid to the base of the tower where it is used for electrical power generation or other industrial processes that can effectively utilize energy at high temperature.

2.1 Energy Absorber With Supporting Tower

The energy absorber in a central tower system has a major impact on the economics of the entire system. While it is true that the major cost in the system is the cost of power plant equipment (Section 9.0), the efficiency of the absorber and the quality of the energy greatly influences the economic competitiveness of the concept.

In Section 4.1, comparative data are presented for several absorber designs. Absorber configurations were examined with either external or internal absorbing surfaces. The criteria for absorber evaluation include:

A. Quality of the energy produced: Must be a prime consideration in any application requiring conversion of heat to work or where a high absolute temperature is a requirement. For example, a one percent improvement in heat-to-work conversion allows about a three percent reduction in the size and cost of the collector system.

B. Efficiency of energy absorption and retention: This is related to the quality, but must be considered on a comparative, economic basis.

C. Engineering feasibility: Emphasis should be on using relatively well developed engineering technology to reduce the time required to reach a practical demonstration system. Research and development efforts should be concentrated on those items which offer significant advantages to system performance or economics.

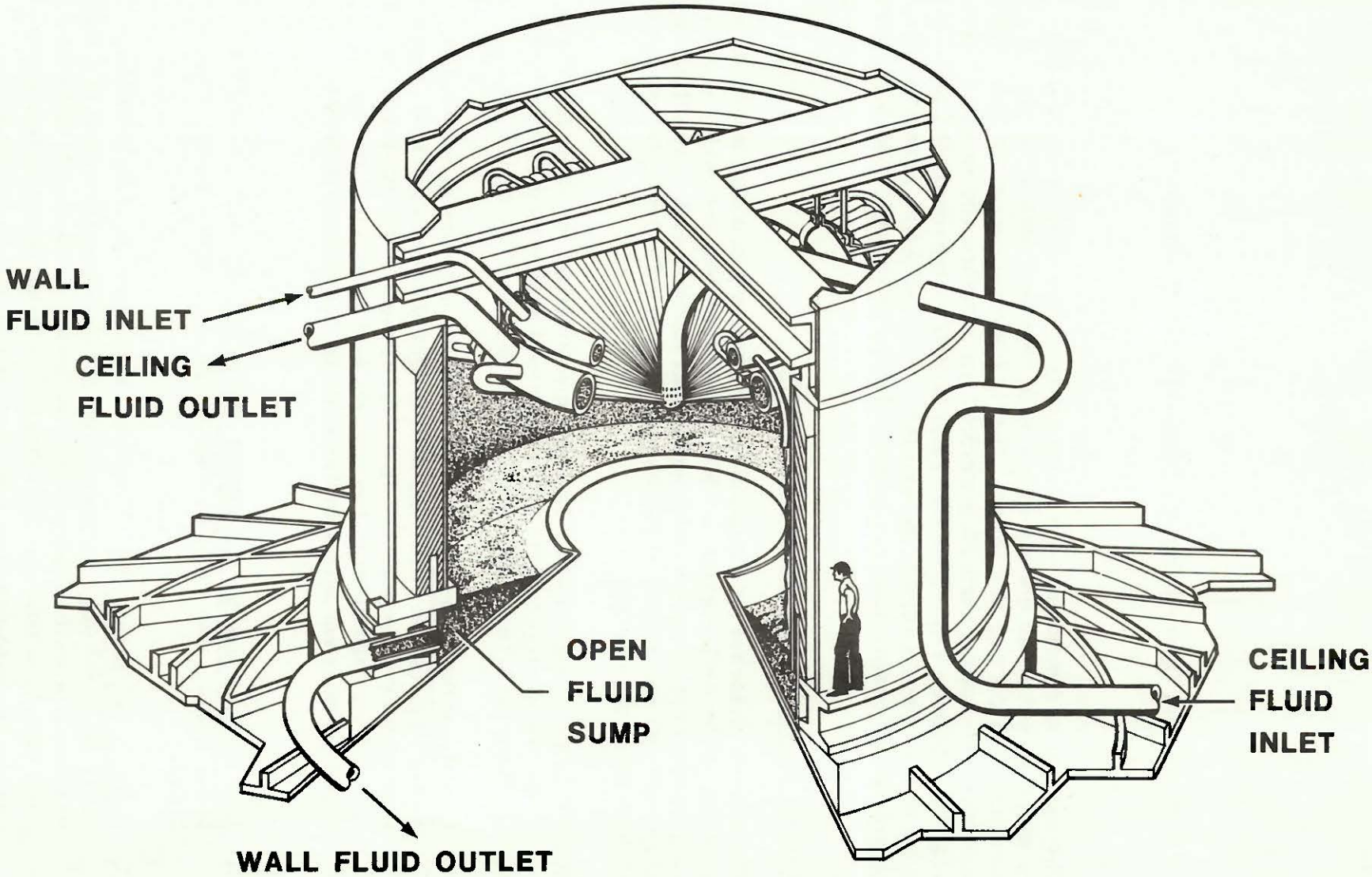

Figure 2-1. Optical Cavity Absorber

D. Maintenance: Maintenance costs and reliability dictate simplicity and selection of options that minimize routine maintenance particularly at the top of the tower.

E. Energy transport: Thermal energy losses and the work required to circulate heat transfer fluid should be minimized.

F. Capital cost: Although the capital cost of this element of the system is not the primary factor, it must not be excessive.

G. Safety: The use of explosive, flammable, and very high pressure fluids should be minimized, and avoided entirely if possible.

Several different types of absorbers have been studied thus far, including externally-irradiated tube boiler configurations with and without windows, and cavity-type radiant tube boilers or heat exchangers. Steam, Hitec,* liquid metals, and other heat transfer fluids were considered for the heat transfer loop. Early in these studies, however, an alternative scheme evolved which seemed to offer a number of system advantages over closed-tube configurations. Rather than being absorbed on a pipe wall or other solid surface and then being conducted into a fluid, the energy is absorbed directly within a heat-transfer fluid in an open cavity, as illustrated in Figure 2-1. The concentrated solar flux enters the cavity through a windowless aperture in the bottom of the cavity and is absorbed in depth within the fluid flowing down the interior walls. The fluid under consideration for electrical power applications is molten Hitec. Though nearly transparent normally, the molten salt is made highly absorptive by doping with a suspension of finely divided particulate material that has high absorptivity.

The combination of direct absorption and the open-cavity configuration appears to offer several potential advantages. Reflection and transmission losses as well as operational problems associated with transmitting high power densities through windows are avoided entirely. Because the solar energy is absorbed directly in the working fluid, the temperature at which the absorber radiates is no higher than the fluid temperature. This method avoids the considerable temperature increment required to conduct heat through pipe walls at high power density, and radiation losses are thus minimized. For a given size aperture, increasing the cavity size increases collection efficiency and decreases flux density at the wall. Problems of hot spots and tube burnouts caused by flux concentrations are also avoided by direct absorption in the circulating fluid, and thermal stress problems

---

*DuPont eutectic mixture of sodium nitrate, sodium nitrite, and potassium nitrate.

can be more easily resolved. The difference between inlet and outlet fluid temperatures can be kept large, thus minimizing mass flow rate, since turbulent flow need not be maintained. Having the aperture at the bottom of the cavity produces a thermally stable condition which tends to inhibit heat loss by convection. Adequate insulation can be used to reduce losses from the outer walls of the cavity to a negligible level.

The system illustrated in Figure 2-1 is one in which energy impinging on the ceiling is absorbed on pipes through which Hitec is circulated; the loop is separate from that of the walls because of the need for turbulent flow in the tubes and a desire for a large temperature difference in the wall loop. In an alternate design, the ceiling loop is eliminated by using an uncooled, conical ceiling made of refractory material with low emissivity. In this simpler design most of the flux incident on the ceiling is reflected or re-radiated to the walls where it is absorbed in the downward flowing film.

Hitec melts at 415 K (288°F) and is stable in air to about 727 K (850°F). It appears that it can be used in this application to about 811 K (1000°F) without excessive decomposition. If advantageous, air can be displaced by maintaining a very slight overpressure of nitrogen within the cavity. While the body of knowledge and experience regarding the use of this fluid is much lower than that for steam, Hitec appears to be better suited for this application. In addition to allowing direct absorption, it can be used at atmospheric pressure, should require less maintenance, and can also be used for thermal storage. While no major problems are presently foreseen, the direct absorption concept will require considerable development. The decomposition and oxidation reactions will be investigated further during the development program to fully characterize the material under anticipated use conditions and to determine practical upper temperature limits. A more detailed discussion of Hitec characteristics is given in Section 4.1. A number of different doping materials are presently under investigation. Oxides of copper and cobalt are among the possible candidates.

Full-scale absorption and fluid flow experiments using a section of a cavity wall are being planned at Sandia's large radiant heat facility. The facility can supply controlled heat fluxes up to 5600 kw_t/m^2 at input power levels up to 5 MW_t sustained and 20 MW_t peak.

A terminal concentrator, which has been devised for use at the aperture entrance, is capable of increasing the system concentration ratio by a factor of about 2.5 with a system rim angle of 60 degrees. It becomes increasingly beneficial for maintaining high collection efficiency with increasing temperature; however, it is not yet clear whether its use will be cost-effective at 811 K (1000°F).

Although the open-cavity, direct-absorption system currently appears to be the most promising, evaluation of other options will continue in parallel for some time.

2.2 Tower

A guyed steel tower has been investigated for support of the cavity absorber. Bechtel Corporation has assisted in preliminary design and costing studies. Designs for costing purposes were done for 200 and 400 m tower heights with interpolation at 300 m. The tower is conservatively designed to survive 368.0 km/hr (230 mph) winds at the 300 m level and to support four times the estimated cavity weight. Tower costs are estimated at 1.1, 2.0, and 3.3 million dollars respectively for heights of 200, 300, and and 400 m. Design characteristics are discussed in Section 5.0.

2.3 Mirror Array

A number of mirror module concepts were screened and a few of the more promising alternatives were investigated further. Different types of mirror surfaces, mounting arrangements, and tracking systems have been studied. Among various fabrication approaches tried for mirrors are laminated honeycomb for substrates and polyurethane foam molding and epoxy spin-casting for dished surfaces with integral structure. It was found that temperature gradients through some of the foam assemblies caused significant distortion of mirror surface contours. Several schemes tried for dishing initially flat surfaces included applying edge moments, pressure differentials, and various combinations of point loads. No single technique has yet emerged as clearly superior. A great deal more design and experimental work on mirror modules will be required before the various approaches can be evaluated realistically. A full-gimbaled mount, constructed to test tracking and control systems and to evaluate mirrors, is shown in Figure 2-2. A prototype closed-loop tracking and control system, using a sensor in the reflected beam, has been fabricated and tested successfully.

A computer program has been developed to determine the mirror spacing and arrangement which minimizes the cost of redirected energy for a range of average mirror density and mirror costs. Initial results indicate that with the same average density, variable spacing may be only slightly better than uniform spacing. Additional parameters for variable spacing are being incorporated which may allow further optimization. A more detailed description of this model is given in Section 6.2.

The feasibility as well as the advisability of varying the contour of the mirror surface as a function of included angle between the sun and the absorber is also being studied. Given a fixed-contour mirror that produces a minimum-size image at the aperture when the sun is nearly in line with the absorber, the image size will increase as the angle between the sun and the absorber increases. On the other hand, if the surface contour can be varied slightly with sun position, the minimum image size can be maintained. If the fixed-contour mirrors are used, it follows that a larger-diameter

Figure 2-2. Experimental Mirror Module

aperture will be required to accommodate this off-axis aberration. The percentage increase is greatest when the aperture is comparatively small relative to the mirror size (as will likely be the case for bench, pilot, and demonstration systems). It is not yet clear whether the additional complexity and cost will ultimately be justified by the improvement in system performance of full-scale systems.

Minimizing cost while maintaining adequate accuracy, reflectivity, and lifetime is a fundamental concern governing the design of the mirror module. Costs are highly dependent upon design, fabrication methods, production quantity, accuracy, lifetime, and other requirements which are closely related to system performance and economics. Sandia design studies, experiments, and system tradeoffs are not yet sufficiently advanced to support anything better than very gross estimates of mirror module cost. Consequently, mirror cost is still being handled on a parametric basis over the range of 20 to 40 dollars per square meter.

2.4 Energy Storage System

Energy storage is desirable for a solar central power station to provide electrical power generation capabilities during cloudy periods and to extend the time of power generation with solar-derived energy past sunset. One of the concepts under consideration is to store thermal energy as sensible heat in molten Hitec in steel tanks. The Hitec in the storage system is isolated by a heat exchanger from the high pressure (gravity head) Hitec in the absorber heat transport loop, and is thereby stored at atmospheric pressure. Reasonably high energy density (~96 kW_e-hr/m^3) is achieved by operating over a rather wide temperature range of 473 to 779 K. Hot and cool fluids are kept separated either by using separate tanks or by storing both hot and cool fluids in the same tank using a thermocline mode of operation.* Based on an estimated cost of $0.15 per lb for Hitec, overall storage cost was estimated at about $9.20 per kW_e-hr.

2.5 Electrical Power Generation System

Electric power is generated in a power plant at the base of a single solar collection system tower or in a central plant served by two or more solar collection systems. The power plant includes a steam generator, the turbine-generator unit, condenser, cooling tower, and in the hybrid system a supplemental fossil fuel firing system. The steam generator is a large heat exchanger in which the energy in hot molten salt is used to produce superheated steam for operating the turbine. This generator may be designed to produce steam at subcritical or supercritical pressure and may provide a reheat for the steam, depending upon the particular power cycle and steam conditions chosen.

---

*Thermocline mode of operation is discussed in "Sensible Heat Storage in Liquids," T. D. Brumleve, SLL-73-0263, July 1974.

The cooling system* for condensing the turbine exhaust steam consists of mechanical draft wet cooling towers located so that the moisture plumes from the towers do not interfere with the solar collection system. In locations where cooling water is unavailable, dry cooling would be used.

A supplemental coal-firing system* is provided so that electrical power output can continue whenever the solar energy portion of the system cannot be used. The coal-firing system consists of two half-capacity coal-fired boilers, coal and ash handling equipment, and a coal storage site. Oil or natural gas could also be used if available and economic.

A number of different methods of interfacing with a conventional steam/electric power plant were compared on the basis of performance, fuel savings, and electrical energy costs. Pure solar and hybrid solar-fossil plants, with and without thermal storage, were compared with conventional fossil-fueled plants for both base load and intermediate load applications. Several simplifying assumptions regarding demand and plant capacity factors were made for the purpose of comparison. It was assumed that the solar systems would be operated whenever possible since marginal energy cost should be very low. A 16-hour per day, year-around demand was assumed for the intermediate cases. Other assumptions and explanations are given in Section 8.0. The pure solar systems require additional capacity elsewhere in the network to compensate for cloudy days, whereas the hybrid systems do not. A nominal 300 MW_t solar collector system was arbitrarily chosen as the basis for comparing the different modes of operation. Because of the economy of scale in power plants, it proved to be cost-effective for systems of this size to cluster a sufficient number of collector systems to supply a single power plant of at least 250 MW_e. In some of the cases considered, thermal storage is provided as sensible heat in molten Hitec at atmospheric pressure operating between 473 K (392°F) and 779 K (942°F). At least 30 minutes storage is provided in all cases to buffer rapid changes in flux rate caused by passing clouds.

In the hybrid systems, fossil fuel (coal in this example) is used to heat Hitec whenever necessary to make up any deficit in solar energy. Hot Hitec is routed through a heat exchanger to produce steam at 767 K (922°F) and 24.1 MPa (3500 psi). A supercritical steam cycle is assumed with an efficiency of 42 percent operating in the solar mode; a lower efficiency of 36 percent is assumed for the fossil mode to account for stack losses.

---

*Suggested by Bechtel Corporation, under contract to Sandia Laboratories.

2.6 Economic Analysis

In order to explore the economic implications of various methods of interfacing with power plants, general characteristics, capital costs, and bus bar energy costs were roughly estimated for nine different combinations. The nine cases included base load and intermediate load operation for fossil, hybrid solar/fossil, and pure solar plants. Thermal storage was included in some cases. All systems were configured at 1000 MW_e name-plate capacity.

Costs for the tower and power plant were estimated based on information supplied by Bechtel. A levelized annual fixed charge of 15 percent of total capital cost was used in each case to cover interest, local taxes, and operating costs. Bus bar costs of electrical energy produced were estimated as a function of fuel cost. Details of the comparisons are discussed in Section 8.0.

With the assumptions and cost estimates used for these comparisons, hybrid systems without thermal storage produced electrical power at the same cost as their fossil counterparts in the fuel cost range of $1.45 to $2.15 per million Btu, and were about 10 to 20 percent higher at $1.00 per million Btu. The hybrids with thermal storage became competitive in the range of $1.30 to $2.60/MBtu, and were about 20 to 60 percent higher at $1.00/MBtu. The pure solar systems appeared to be competitive in the fuel cost range of $1.60 to $2.40/MBtu; but in these cases, energy costs do not reflect the additional costs associated with the incremental backup capacity which would be needed elsewhere in the network during evening and cloudy periods.

Because of the many assumptions used in this comparison, the magnitude of the various costs must be viewed as rough estimates only. The comparison should be reasonably valid, however, since consistent assumptions were used for all systems.

2.7 Program Outline

The research program is summarized in Table 2-1, and a schedule of major milestones is shown in Figure 2-3. Many other activities are also involved such as power plant design and interfacing, tower design, mirror module development, thermal storage evaluation, control system design and economic studies.

During Phase I, which has been completed, design studies were done on all the major elements of the system to evaluate the advantages and disadvantages of the central absorber concept. Several prototype components were constructed and operated. An experimental mirror module for testing mirrors and tracking system is shown in Figure 2-2.

Large cost and technical uncertainties remain for the mirror module and the central absorber with its supporting tower. It is also clear that considerable in-depth design and experimental effort on several elements will be required before the uncertainties can be reduced to acceptable levels.

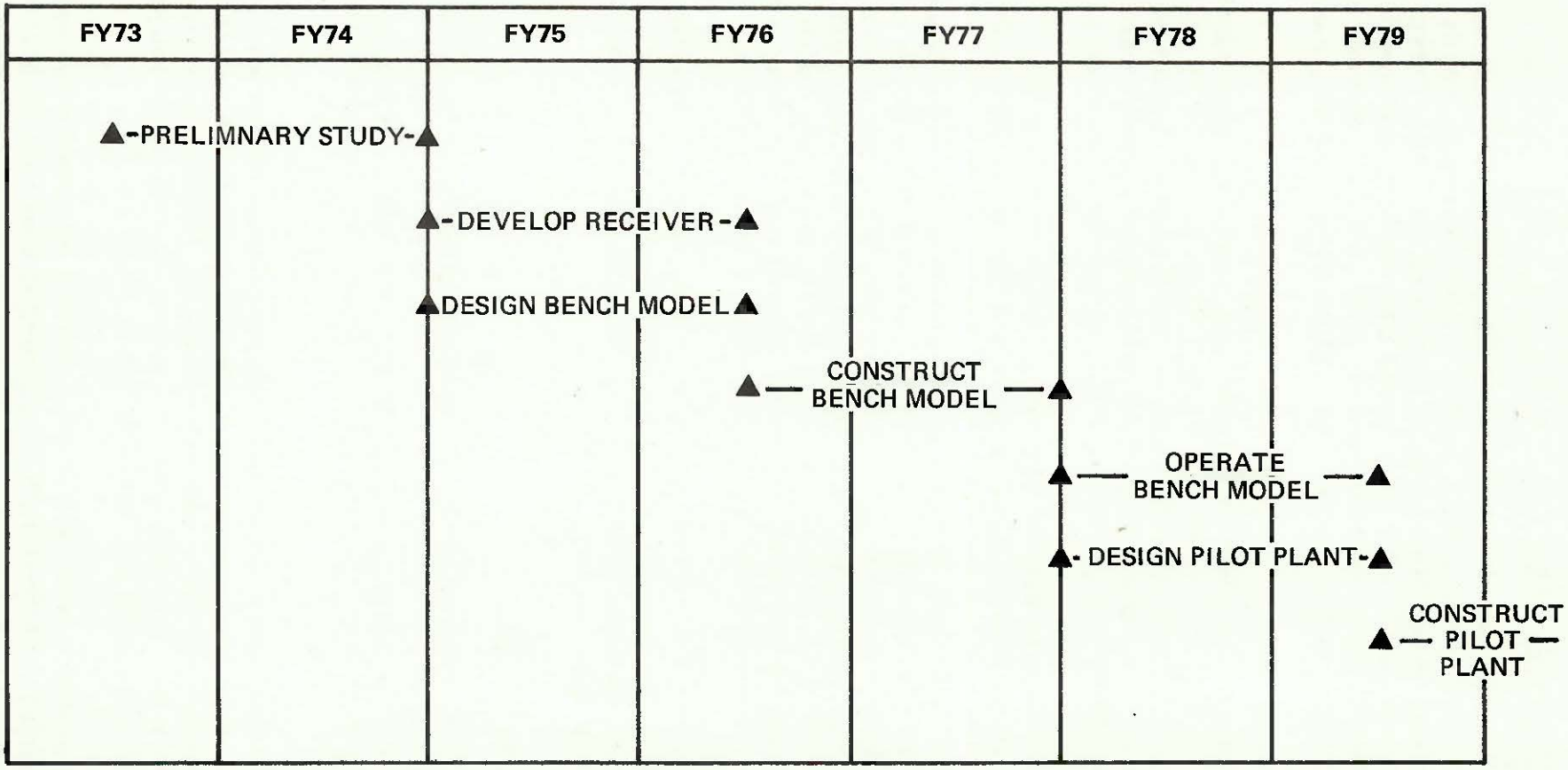

Figure 2-3. Development Schedule

TABLE 2-1

DEVELOPMENT ACTIVITIES

Phase	Description	Duration
I	Preliminary study	18 months (Completed)
II	Develop absorber and heat transport system Design bench model	18 months
III	Construct bench model	18 months
IV	Design and construct pilot plant	3 years

Some of the principal research activities in Phase II are summarized below.

Central Absorber and Heat Transport Loop

Design

Emphasis will be given to developing a practical demonstration model within a limited time scale. An attempt will be made to work within state-of-the-art engineering and do basic research only as necessary for advancement or where justified by the advantages gained.

Selection of the heat transport fluid is very important and has a major influence on the materials and geometry of the absorber. Alternatives will be carefully weighed and a selection made early in the program.

Analysis

Areas of supporting analysis include:

Absorber Coupling to Mirror Field--The goal of this activity is to calculate the distribution of reflected solar flux in the plane of the absorber aperture and to map the reflected flux onto the cavity walls and ceiling. These calculations will start with the parameters previously calculated for

an optimized field, and will use a ray tracing computer program to model the sun as a disc source with limb darkening, the random mirror aiming errors and surface imperfections, and the complex reflections from a terminal concentrator.

Absorber Operation Analytical Model--The goal of this activity is to investigate in detail the relationships affecting absorber operation. This study will model the absorber and its operation--varying the shape and size, the radiation properties and temperatures over the cavity walls, distribution of reflected solar flux on the absorber walls, and the parameters describing the heat transfer fluid.

Testing

Confirmation of Analysis Experiment--An experiment to investigate the parameters affecting radiant energy transfer to the absorber and subsequent energy transfer to a working fluid will be performed. This experiment, now being designed, uses a high temperature lamp in an ellipsoidal reflector to illuminate a test cavity cooled by a suitable working fluid. Relationships will be determined for input flux level, absorber temperature distribution, and working fluid flow rate and temperature distributions. This experiment is described in detail in Section 4.3.

High Temperature Materials--Material survival for many years under the combined effects of high temperature, corrosive environments, high pressure, and cyclic thermal stress is an important area for investigation. The Sandia materials group will investigate and attempt to solve these problems through a combination of analysis and laboratory tests utilizing existing radiant heat facilities and other high temperature, combined-environment test facilities.

Section of Absorbing Cavity--A section of an absorbing cavity will be tested in an existing Sandia Laboratories radiant heat test facility. The facility can input up to 5600 kW/m^2, several times the maximum design flux level. A section of a full-scale cavity will be tested rather than a small scale model since some of the aspects of the problem are not amenable to scaling. The facility is described in Section 4.5.

Systems Design

An early systems experiment is important and the design of a bench model will be started immediately. One of the Phase II activities will be a determination of the most appropriate size and characteristics for this bench model. An example of a consistent set of parameters for a 5 MW_e system is shown in Table 2-2.

TABLE 2-2

POSSIBLE BENCH MODEL PARAMETERS

Electric Power Output	5 MW
Power Generation Efficiency	0.36
Collected Solar Power	14 MW
Tower Height	65 m
Mirror Field Rim Angle	60°
Mirror Field Radius	113 m
Mirror Field Ground Area	40,120 m^2
Overall Mirror Area/Ground Area	0.5
Overall Mirror Area	20,060 m^2

3.0 Solar Collection System Variables

Studies by Sandia Laboratories on solar collection system variables have revealed that the performance of solar collection systems is significantly affected by interactions between certain system variables. These variables can be divided into two groups: those that affect mirror field layout, mirror design, and the reflected solar energy; and those that affect the central absorber and the collected solar energy. The first group includes:

tower height
mirror field rim angle
mirror field shape
overall mirror density
spacing between mirrors
mirror shading and blocking
mirror reflectivity
mirror surface, tracking, and focusing accuracy
system concentration factor

The second group includes:

external or internal energy absorption
receiver geometry
receiver temperature
receiver absorptivity and emissivity

The effects of changes in these variables are examined by studying the performance of a nominal 300 MW_t system whose characteristics are

Tower Height	300 m
Mirror Field Rim Angle	60°
Mirror Field Shape	Circular
Overall Mirror Density	0.50
Mirror Deployment	Uniform
Mirror Reflectivity	0.85
Absorber Type	Cavity

Cavity Aperture Diameter	18.1 m
Cavity Height	21.5 m
Cavity Diameter	20.0 m
Cavity Temperature	1000°F
Cavity Emissivity	0.95
Cavity Energy Collection Efficiency	0.97

System power levels and collected energy totals are determined primarily by system geometry (mirror field rim angle and field shape) and by mirror deployment (the mirror density in the field and whether the mirror spacing is constant or varied over the field). The nominal system is configured with a cavity-type receiver, and has uniform mirror spacing over a circular mirror field. The overall mirror density is also the local mirror density at each point in the field. The effect of variable spacing between mirrors is discussed in Section 6.0. The power levels and collected energy totals for the nominal system, including the effects of shadowing and blocking of solar flux by adjacent mirrors, are shown in Figure 3-1 for a clear spring equinox day and for summer and winter solstice days.

Holding system geometry and mirror deployment constant, the power levels and collected energy from a system are proportional to the mirror field area. Thus with constant system geometry, the power levels and collected energy vary as the square of the system dimensions. For example, the power levels are proportional to the square of the tower height.

For a tower of a given height, increasing the rim angle rapidly increases mirror field area and power level as shown in Figure 3-2; at rim angles above about 60 or 63 degrees, however, cavity dimensions become excessively large. Figure 3-3 shows the effect of varying the rim angle by changing the tower height while holding the mirror field area constant.

System power is also a function of the mirror field overall mirror density. Power levels for the nominal system with various overall mirror densities are shown in Figure 3-4. Power levels for systems having different overall mirror densities, but the same geometry (circular field with 60° rim angle) and total mirror area as the nominal system are shown in Figure 3-5.

The second group of system variables affects the configuration and energy collection efficiency of the central receiver--a cavity which collects the reflected solar energy with high efficiency. Preliminary estimates of cavity efficiency have been obtained using a two-zone cavity model based upon the following assumptions:

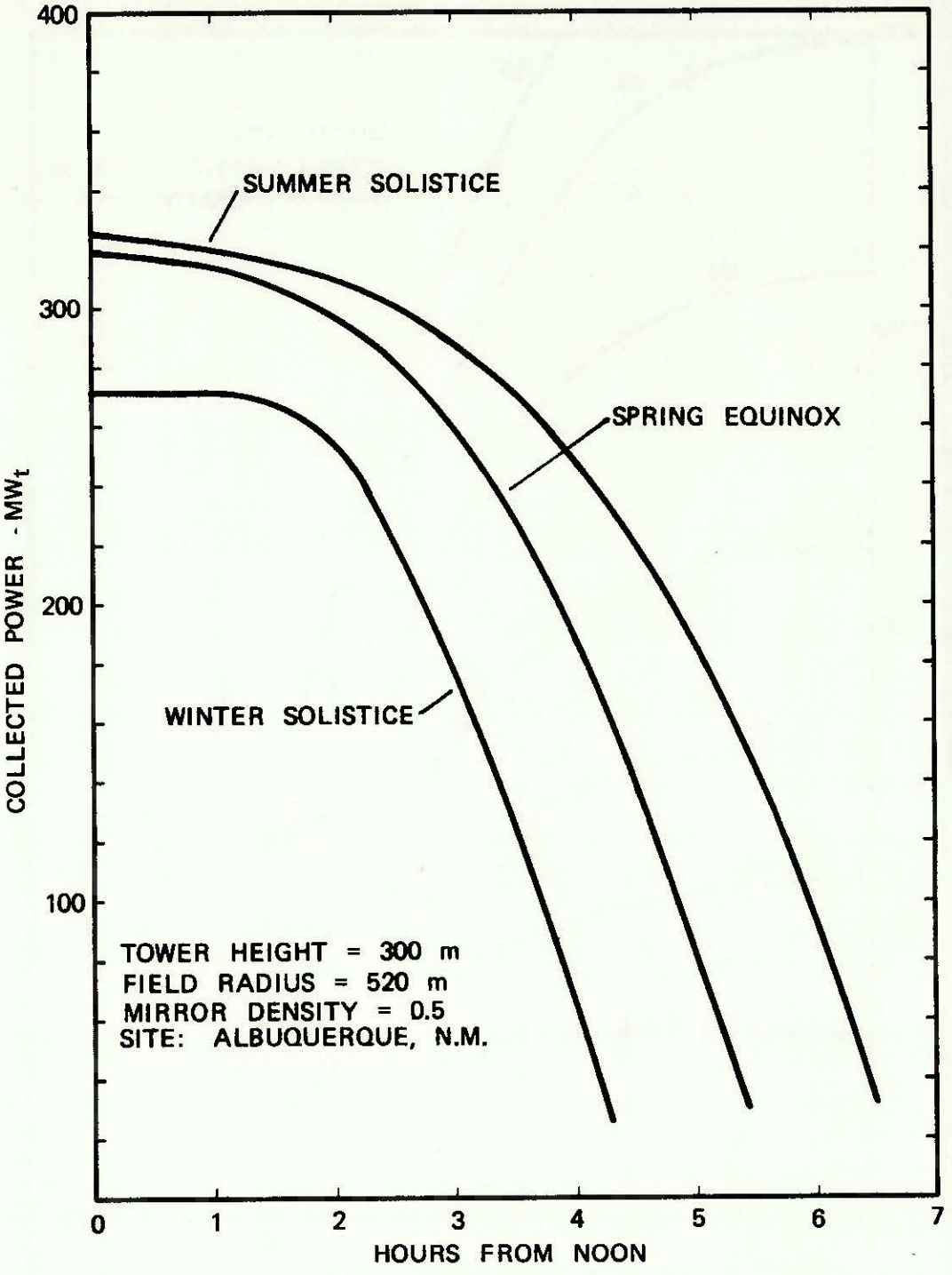

Figure 3-1. Power Collected Versus Time of Day for a Nominal 300 MW_t Point Focus Solar Collection System

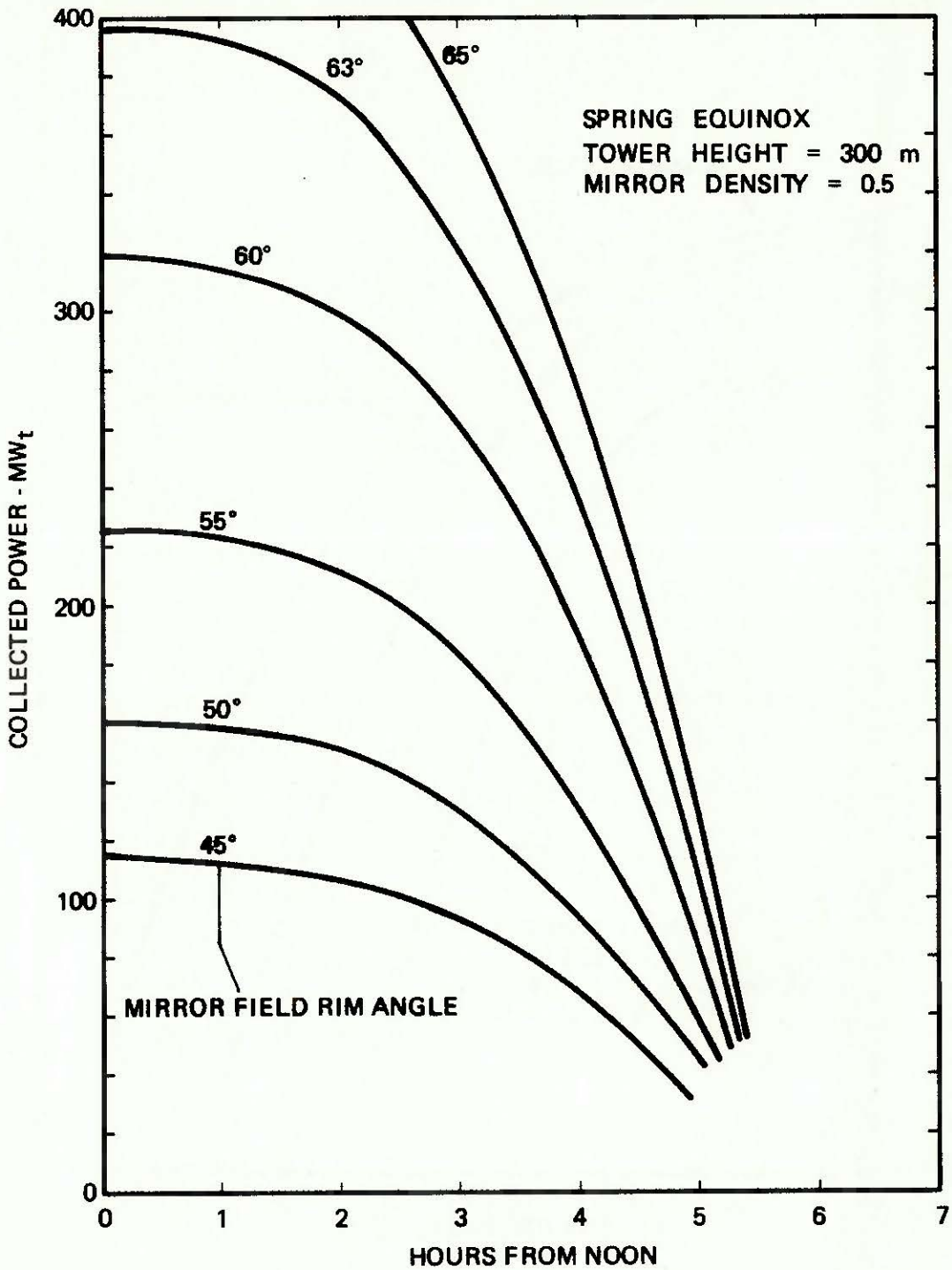

Figure 3-2. Collected Solar Power Versus Time for Systems With Rim Angles Varying From 45° to 65°

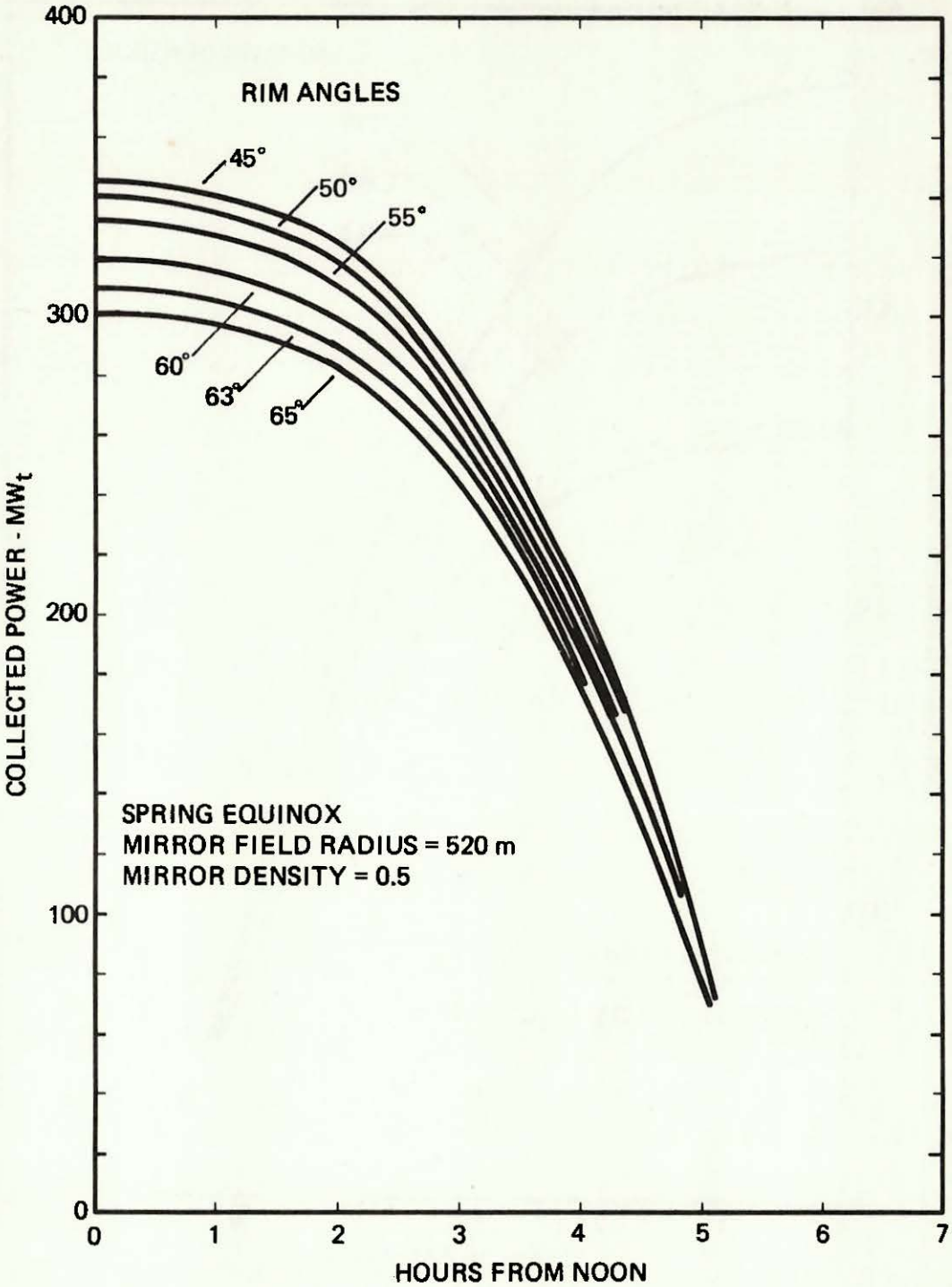

Figure 3-3. Power Collected Versus Time for Systems With Equal Mirror Area and Mirror Density and With Varying Rim Angles

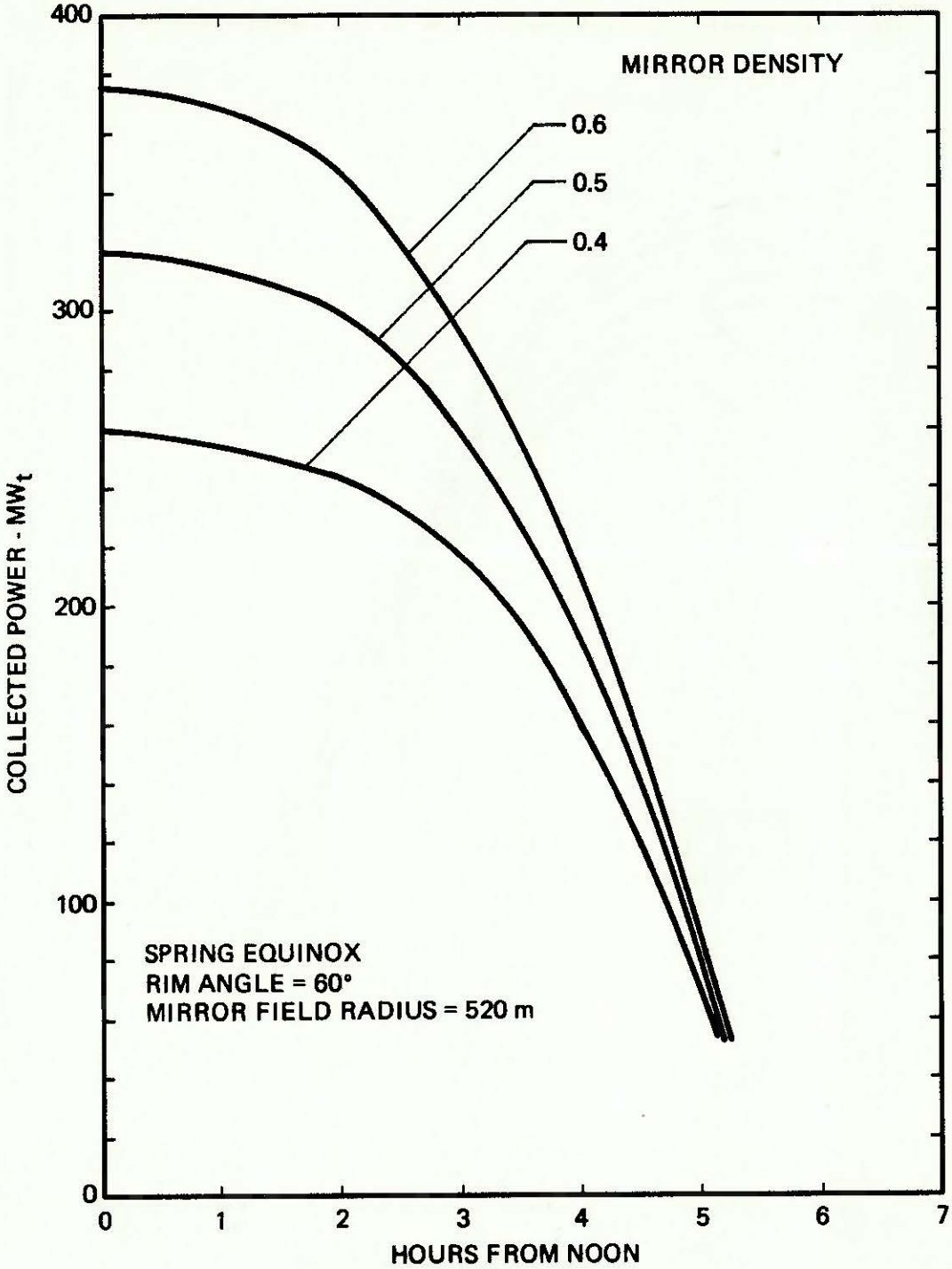

Figure 3-4. Power Collected Versus Time for Systems Having Equal Tower Heights and Mirror Field Radii and With Varying Mirror Densities

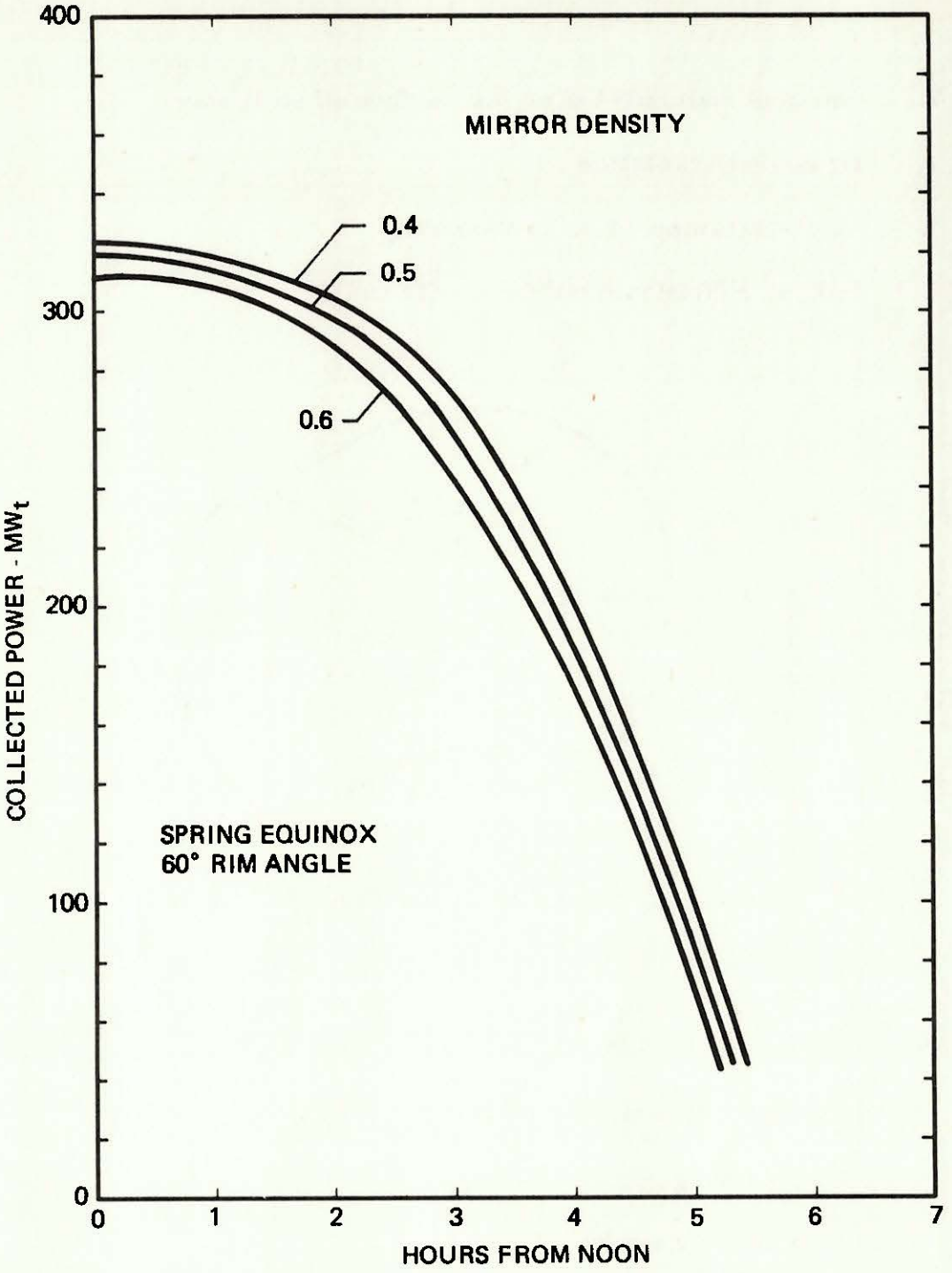

Figure 3-5. Power Collected Versus Time for Systems With Equal Mirror Area and Varying Mirror Density

1. Uniform radiosity* over the surface of each zone

2. Gray-body radiation

3. Uniform temperature in the cavity

4. Diffuse radiation from the cavity walls

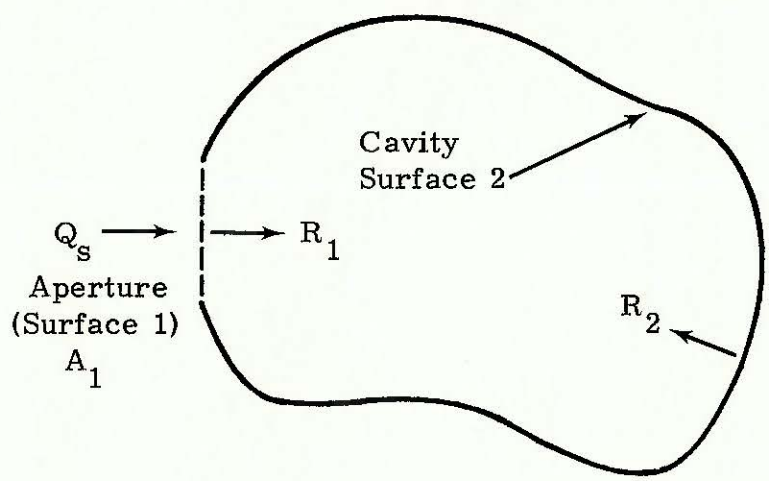

Figure 3-6. Model of a Two-Zone Enclosure

Using the following nomenclature:

Q_s - Incident concentrated solar flux

R_1 - Flux leaving surface 1 = Q_s

R_2 - Flux leaving surface 2

F_{12} - Fraction of energy leaving surface 1 which is directly incident on surface 2.

*The sum of the emitted and reflected energy leaving a surface.

F_{21} - Fraction of energy leaving surface 2 which is directly incident on surface 1

F_{22} - Fraction of energy leaving surface 2 which is directly incident on surface 2

A_1 - Area of surface 1

A_2 - Area of surface 2

ϵ_2 - Emissivity of surface 2

ρ_2 - Reflectivity of surface 2

T_2 - Temperature of surface 2

σ - Stefan-Boltzmann constant

The cavity efficiency is defined as:

$$\eta_c = \frac{\text{net energy passing through the aperture*}}{\text{Incident solar energy}} \tag{1}$$

$$\eta_c = \frac{Q_s A_1 - R_2 A_2 F_{21}}{Q_s A_1} = 1 - \frac{R_2 A_2}{Q_s A_1} F_{21} \tag{2}$$

It is a property of radiating surfaces** that

$$F_{12} A_1 = F_{21} A_2$$

and since in this case, $F_{12} = 1$, $F_{21} = \frac{A_1}{A_2}$, $F_{22} = 1 - \frac{A_1}{A_2}$

then,

*This definition is useful for characterizing normal daytime operation; however, it is not directly applicable to startup or other transient conditions.

**Reciprocity for configuration factors between finite areas, pg. 188, "Thermal Radiation Heat Transfer," R. Segel and J. R. Howell, McGraw-Hill, 1972.

$$\eta_c = 1 - \frac{R_2}{Q_s} \tag{3}$$

$$R_2 = \epsilon_2 \sigma T_2^4 + \rho_2 (R_1 F_{21} + R_2 F_{22})$$

Substituting and solving for R_2,

$$R_2 = \frac{\epsilon_2 \sigma T_2^4 + \rho_2 Q_s A_1 / A_2}{1 - \rho_2 (1 - A_1/A_2)}$$

Using the gray-body assumption $\rho_2 = 1 - \epsilon_2$ and substituting,

$$R_2 = \frac{\epsilon_2 \sigma T_2^4 + (1 - \epsilon_2) Q_s A_1 / A_2}{\epsilon_2 + (1 - \epsilon_2) A_1 / A_2}$$

substituting into Equation (3)

$$\eta_c = 1 - \frac{\epsilon_2 \sigma T_2^4 / Q_s + (1 - \epsilon_2) A_1 / A_2}{\epsilon_2 + (1 - \epsilon_2) A_1 / A_2}$$

Using $\Theta = A_1/A_2$, and $Q_s = CQ_R$ where C is a solar collector flux concentrator factor and Q_R is the solar flux reflected from the collector mirrors,

$$\eta_c = \frac{\epsilon_2 \left(1 - \frac{\sigma T_2^4}{CQ_R}\right)}{\epsilon_2 + (1 - \epsilon_2)\Theta} \tag{4}$$

Dropping the subscripts for simplicity,

$$\eta = \frac{\epsilon (1 - \sigma T^4 / CQ_R)}{\epsilon + (1 - \epsilon)\theta} \tag{5}$$

where

η = cavity efficiency

ϵ = cavity internal surface emissivity = α = absorptivity*

T = cavity internal temperature

C = system concentration ratio

Q_R = reflected solar flux per mirror area

θ = aperture area/cavity internal area

σ = Stefan-Boltzmann constant

Dispersion of the reflected energy due to mirror surface errors and mirror tracking and focusing errors means that a larger cavity aperture is required. A larger aperture results in increased energy losses from the cavity and lower cavity energy collection efficiencies.

The effects of the variables ϵ, T, θ, and C on cavity efficiency are shown in Figures 3-7 through 3-10 where one of the four variables is varied while the other three are held constant at the values used for the nominal system. Cavity internal emissivity has a strong effect on cavity efficiency as shown in Figure 3-7. Internal temperature also strongly affects cavity efficiency as shown in Figure 3-8.

The cavity geometry and shape are represented by the ratio of the aperture area to the cavity internal area. This ratio is affected by both the cavity size and shape, which determine cavity internal area, and by the mirror surface, tracking and focusing errors which spread the reflected beams and determine the necessary aperture diameter. With high emissivity, the ratio of aperture area to cavity area has a small effect on cavity efficiency; at lower emissivities the effect is more pronounced as is shown in Figure 3-9.

The effect of system concentration ratio on cavity efficiency is shown in Figure 3-10. The concentration ratio may be varied by changing the mirror field rim angle and thereby changing the mirror field radius, mirror area (assuming a constant mirror density), and required aperture diameter and area.

The concentration ratio may be increased with a terminal concentrator reflector configured as a flared skirt around the aperture. This device reflects and folds incoming beams from regions near the rim of the field and allows a decrease in the required aperture diameter thereby increasing

*Gray-body radiation assumed (ϵ constant for all wavelength bands of interest).

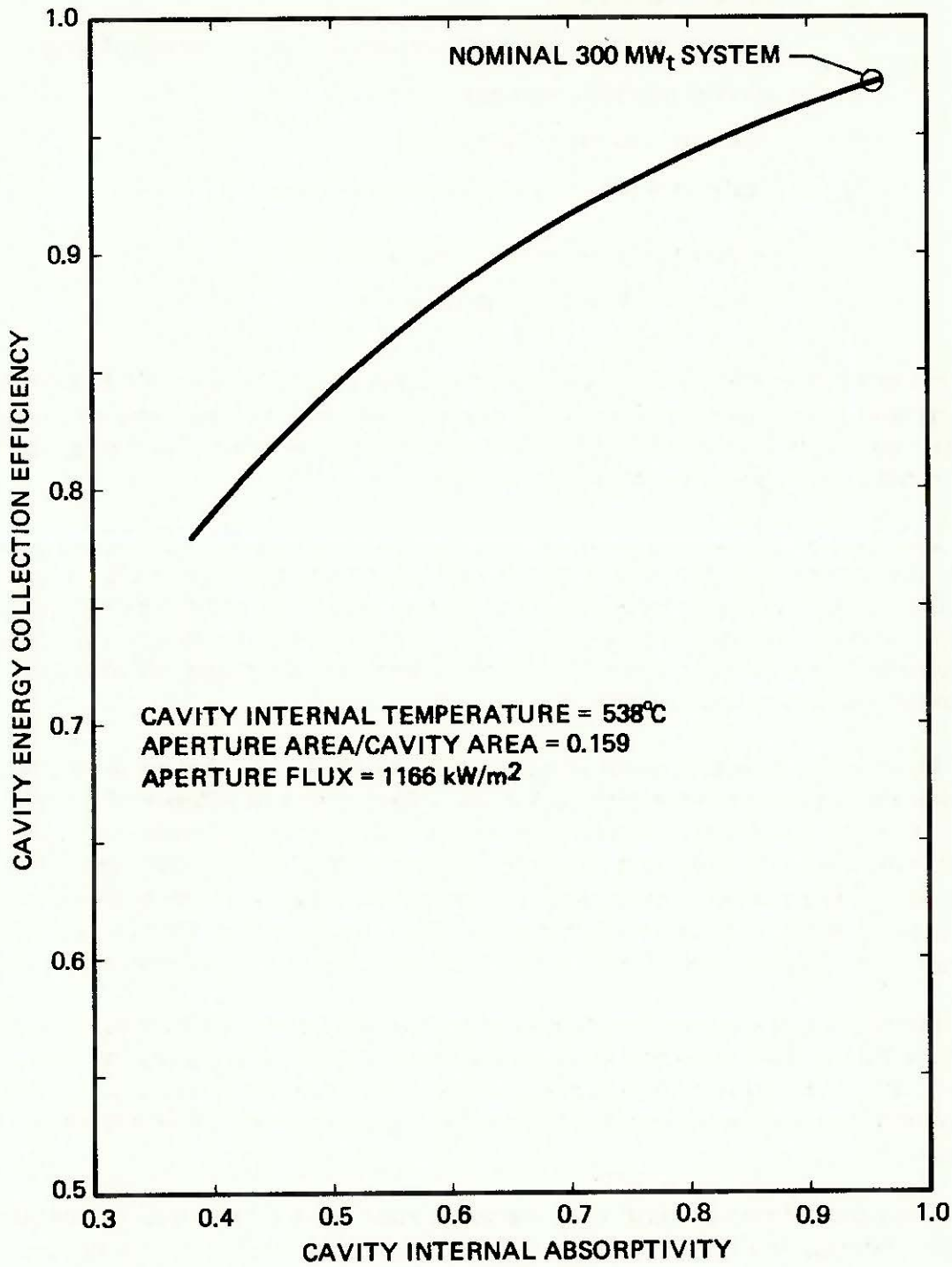

Figure 3-7. Cavity Energy Collection Efficiency Versus Cavity Internal Absorptivity

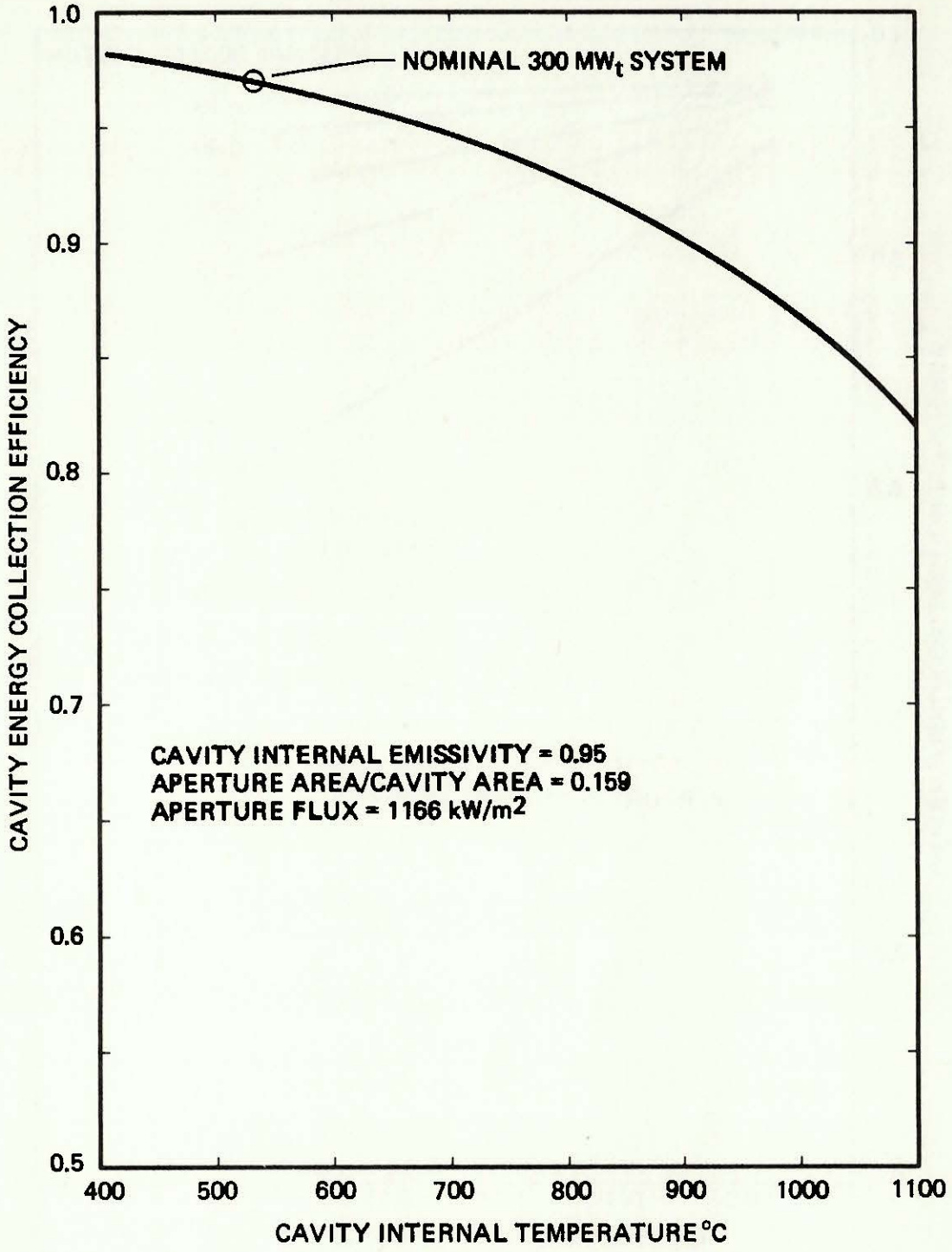

Figure 3-8. Cavity Energy Collection Efficiency Versus Cavity Internal Temperature

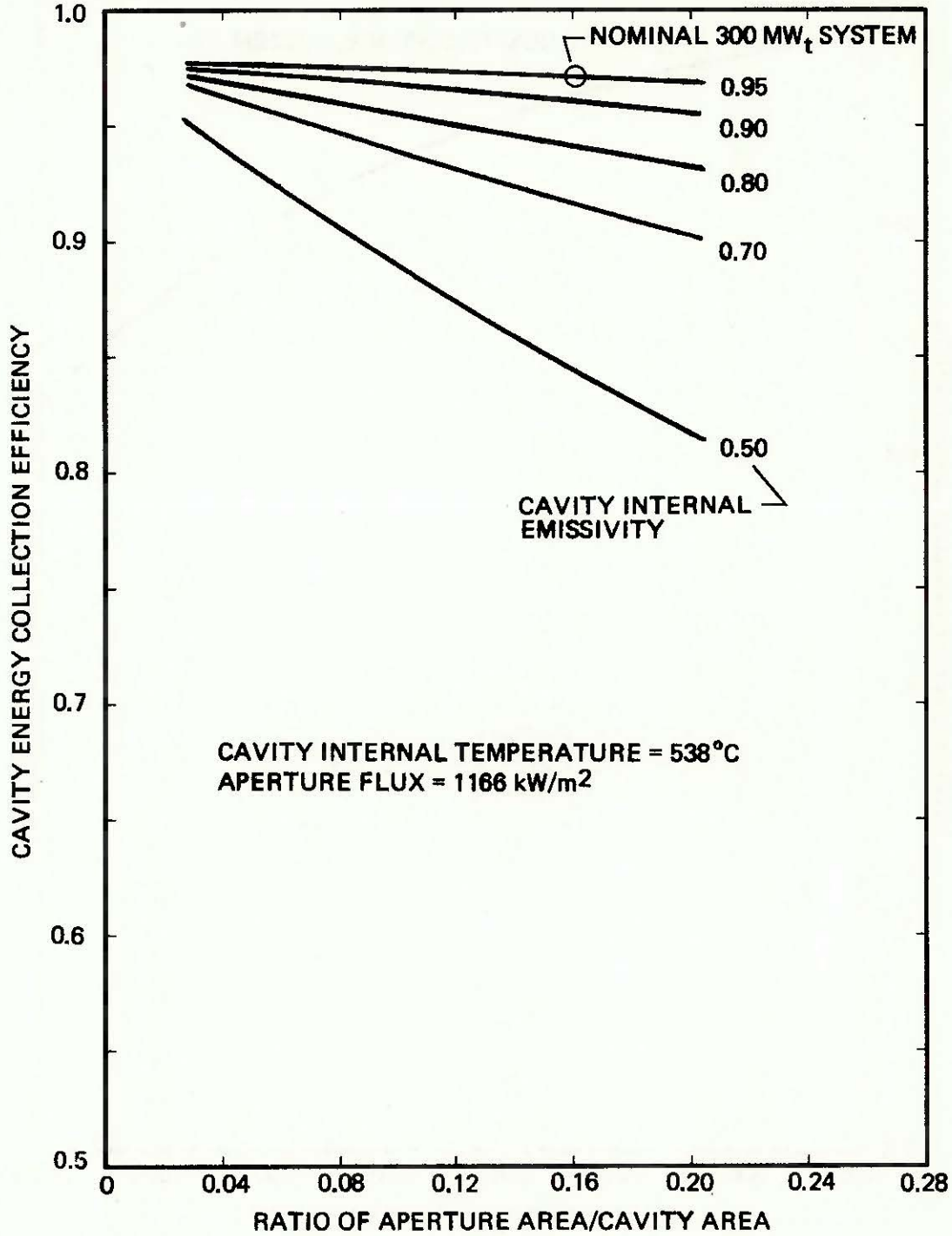

Figure 3-9. Cavity Energy Collection Efficiency Versus Aperture Area/Cavity Area

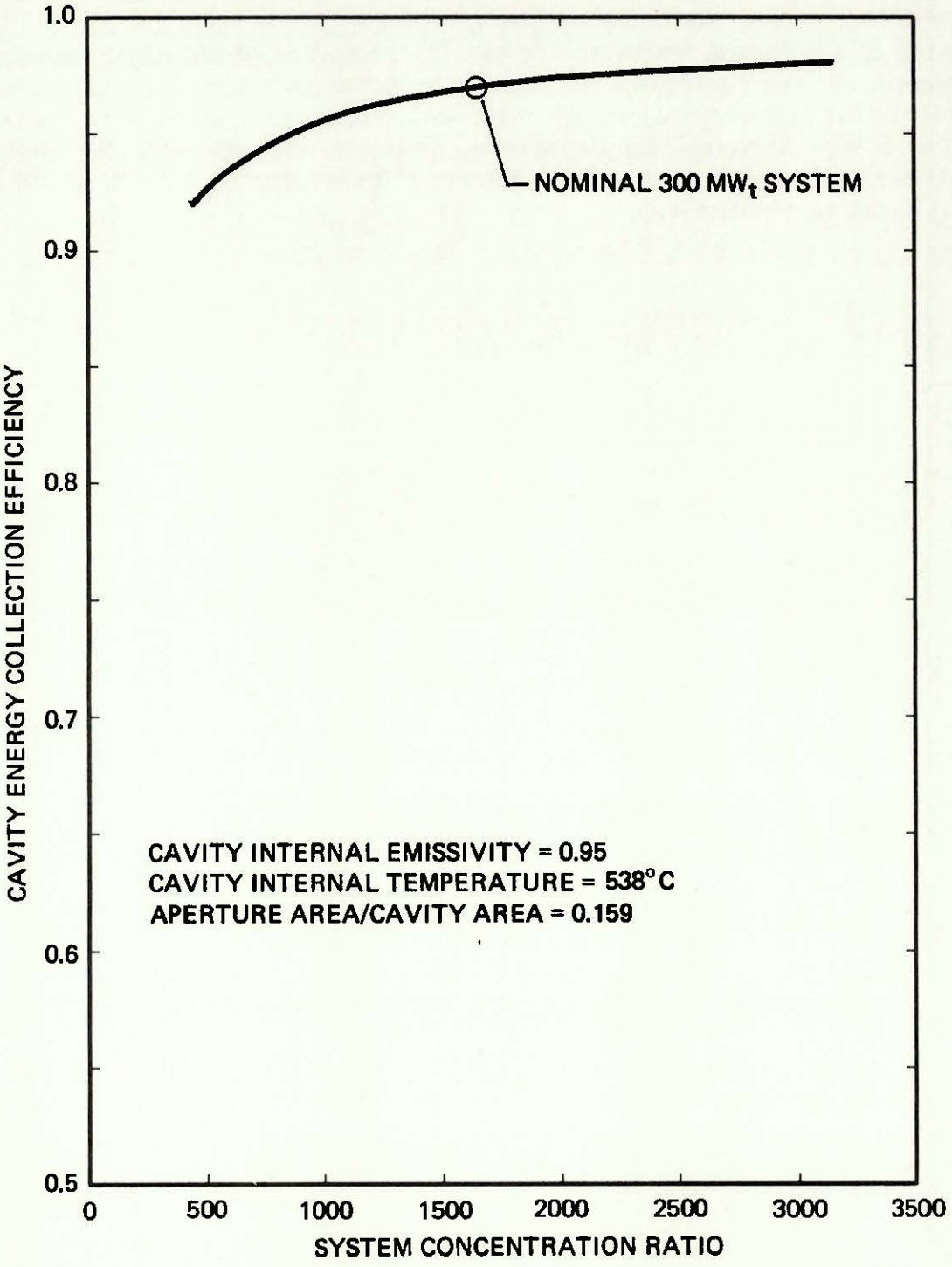

Figure 3-10. Cavity Energy Collection Efficiency Versus System Concentration Ratio

the concentration ratio. Figure 3-11 shows the effect of adding a terminal concentrator at various collection temperatures. The only change was the addition of a terminal concentrator and the reduction of the cavity aperture diameter. At the conditions for the nominal 300 MWt system, the addition of a terminal concentrator improves cavity energy collection efficiency from 0.97 to 0.99. At higher temperatures, or lower emissivities, the improvement would be more pronounced. Terminal concentrators are discussed in more detail in Section 4.0.

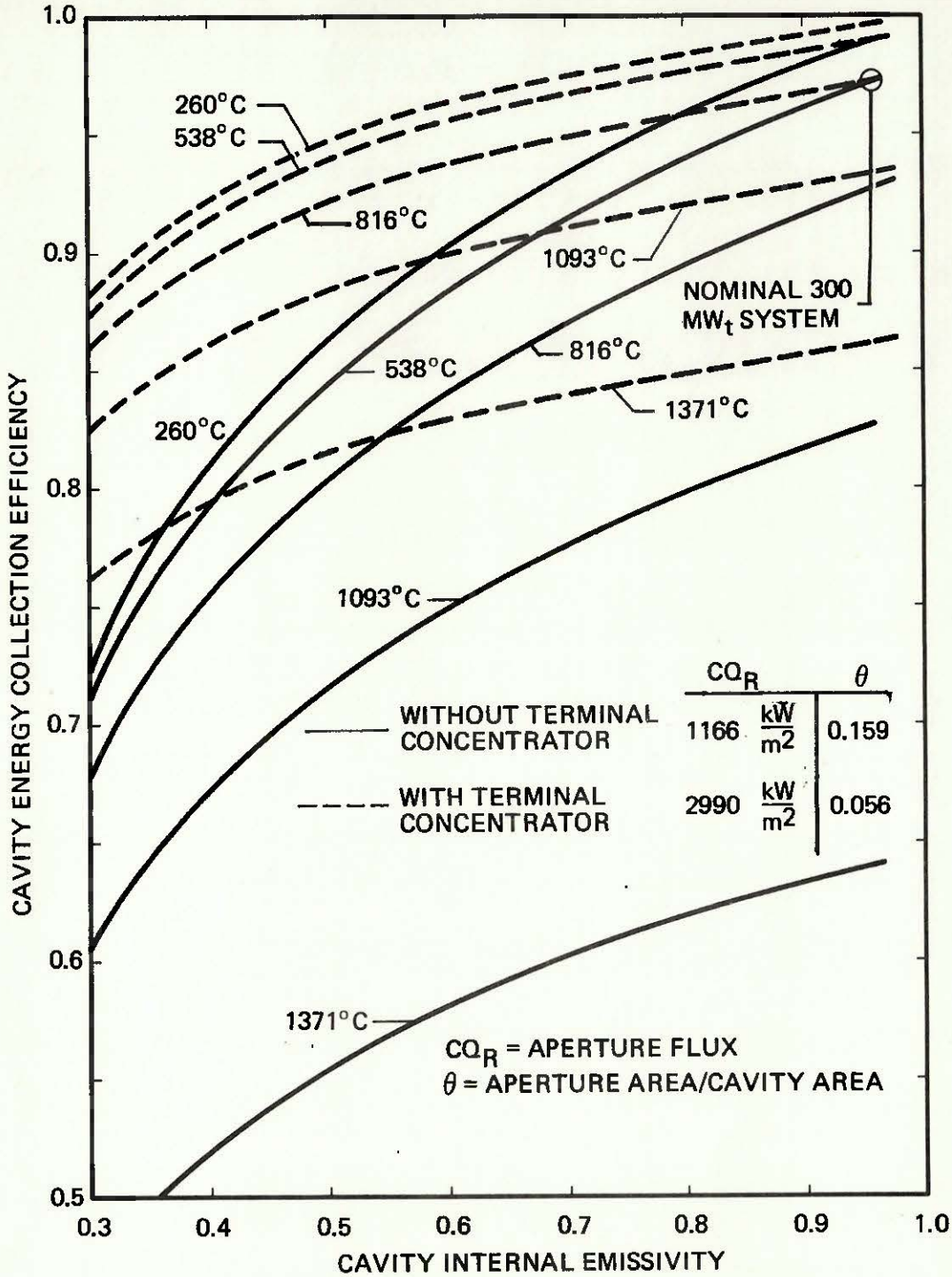

Figure 3-11. The Effects of Varying Cavity Emissivity and Temperature for Nominal 300 MW_e Systems With and Without Terminal Concentrator

4.0 Central Absorbers and Heat Transport Systems

4.1 Design of Central Absorbers and Heat Transport Systems

The central absorber and heat transport system have a major impact on the economics of the entire system. A number of candidate systems were calculated against the following design criteria:

A. Engineering Feasibility

In order to develop the system in a short time period, those systems were emphasized that require no major breakthrough in the thermodynamic state-of-the-art or development of materials.

B. Efficiency of Energy Absorption and Retention

This efficiency directly impacts the cost of the power. The effect is essentially a one-percent decrease in power cost for every one-percent gain in absorption and retention efficiency.

C. Energy Transport

The use of mechanical energy to move thermal energy was minimized.

D. Maintenance

Emphasis was given to systems that would require simple equipment, particularly at the top of the tower. Routine replacement and cleaning of equipment at that location could have a major effect on the feasibility of the concept. Simplicity, ease of replacement, and elimination of any pumps and valves at tower top were the goals.

E. Capital Cost

Capital cost of the cavity-heat transport system has a small impact on the cost of power produced, but was kept as low as possible within the other system constraints.

F. Safety

Where possible, the use of explosive, flammable, and very high-pressure fluids was avoided. High-temperature, high-pressure fluids which were necessary were located away from the tower and close to the prime mover. This emphasis is not only for personnel safety but also to preclude the possibility of a catastrophic failure (boiler explosion or fire) in the absorber tower system. The system should be as fail-safe as possible.

The following general conclusions have been reached:

1. A steam power cycle should be selected for the prime mover. The regenerative reheat cycles used in commercial power plants are providing reasonably high efficiency.

2. A steam boiler should not be located at the top of the tower if other systems with equal or better efficiency can be developed that operate with more safety and less maintenance.

3. The heat transport fluid should probably be a molten salt although further evaluation should be done before a final selection is made.

4. An internal absorbing surface (a cavity) is preferable because it has a higher efficiency than an external absorbing surface. In addition, a terminal concentrator has the potential of further increasing efficiency.

Boiler Considerations

The avoidance of a steam boiler at the top of the tower may seem inconsistent with criteria A above. However, a steam boiler for the tower would require a considerable development because of several differences between standard boiler practice and the requirements for a boiler for a solar application. The major differences are:

1. In a boiler, the operator has direct control of the energy input and can respond to changes in demand. In a solar system, the amount and distribution of the energy is more difficult to control and reaction to changing conditions is more of a problem.

2. Maintenance of a boiler is high with scale and residue removal a constant problem.

3. If a high-pressure system is used for high efficiency, the high-pressure system would extend from the ground to the tower or the pump would have to be at the top of the tower.

4. Regenerative cycles are possible only if the high-pressure pump is at ground level and very hot high-pressure water is pumped up the tower.

5. Thermal stresses and thermal cycling would be a continual problem and with high pressures involved the probability of failure would be high. Thermal stresses would be affected by changing input conditions, temperature, and direction of the wind and by nighttime shutdown.

6. Resuperheating the steam would not be practical since large volumes of low-pressure steam would have to be pumped to the top of the tower and returned to the ground.

Heat Transport Fluid

Figure 4-1 summarizes the attributes of candidate heat transfer fluids. Note that Hitec, a salt manufactured by Dupont, appears to have the least amount of developmental problems along with one of the highest efficiency capabilities. In addition, it is a safe, low-pressure, commercially available fluid and is easily adaptable to storage of energy. Based upon these characteristics, Hitec was selected for the baseline design. Hitec has the following characteristics:

Eutectic mixture of:	Potassium Nitrate	- 53%	KNO_3	(Saltpeter)
	Sodium Nitrite	- 40%	$NaNO_2$	
	Sodium Nitrate	- 7%	$NaNO_3$	(Soda Niter)
Freezing temperature:	142°C (288°F)			
Thermal capacity:	0.373 cal/gm°C or Btu/lb °F			
Viscosity:	1 centipoise, 540°C (1000°F) 7 centipoise, 204°C (400°F)			
Density:	1.69 grams/cc, 540°C (1000°F) = 105 lb/ft^3 1.93 grams/cc, 204°C (400°F) = 121 lb/ft^3			
Thermal Conductivity:	2.0 watts/(m^2 °C) (0.35 Btu/hr ft^2 °F)			
Heat Transfer Film Coefficient (turbulent flow in 2 in. Sch. 40 pipe):	540°C, 3 m/sec = 8.5 kW/(m^2 °C) 204°C, 3 m/sec = 4.4 kW/(m^2 °C)			
Approximate cost:	33¢/kg (15¢/lb)			

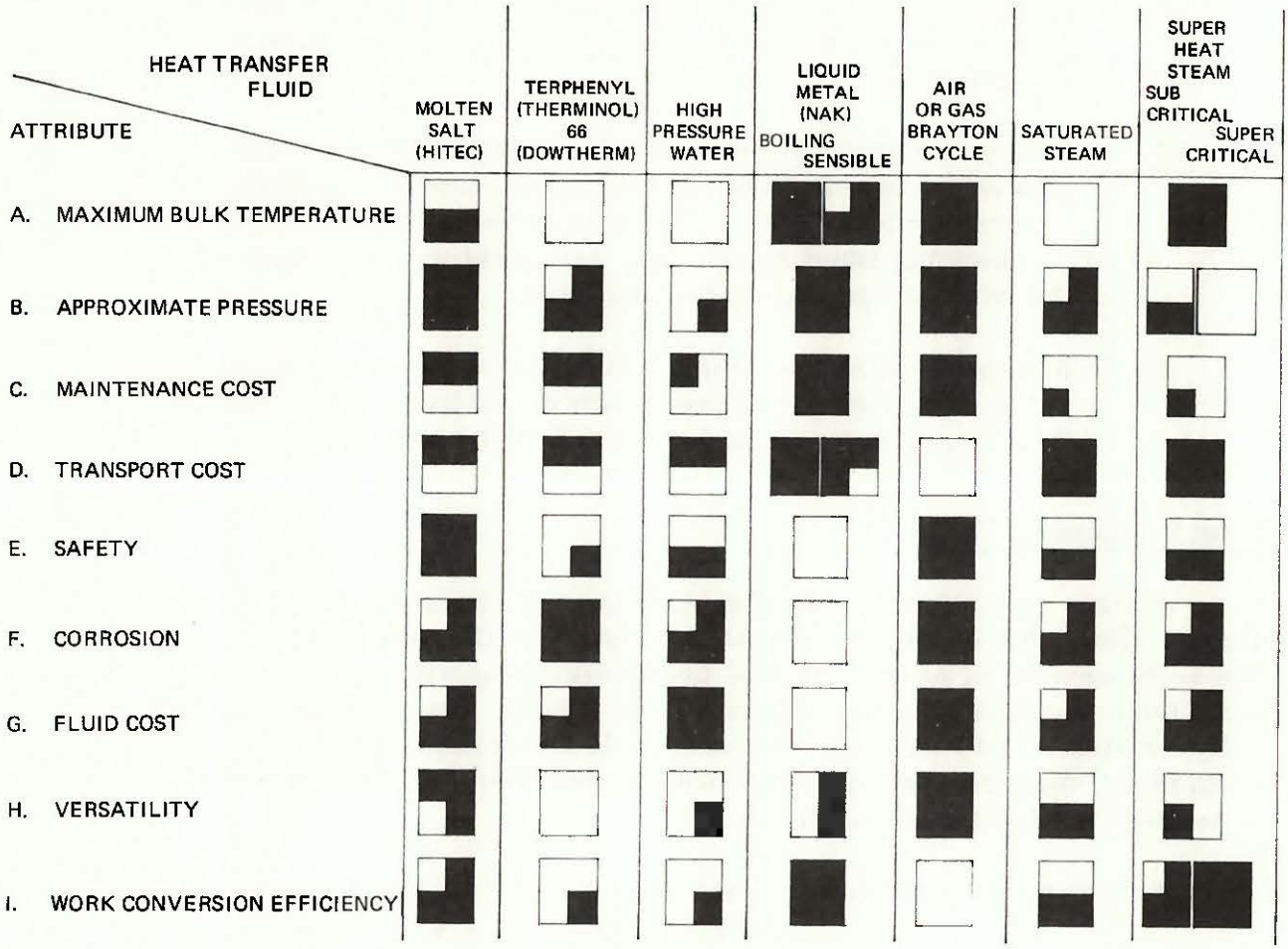

Figure 4-1. Comparison of Heat Transfer Fluids

1	2
3	4

Dark square indicates that the fluid is favorable with respect to the attribute.

A. Maximum Bulk Temperature
1. T > 815°C (1500°F)
2. T > 537°C (1000°F)
3. T > 482°C (900°F)
4. T > 371°C (700°F)
Blank is limited to less than 371°C

B. Approximate Pressure in Absorber
1. P < 50 atmospheres
2. P < 100 atmospheres
3. P < 150 atmospheres
4. P < 200 atmospheres

C. Maintenance Cost
1. No scale problems
2. Low pressure
3. Low temperature pump
4. Very low cost

D. Transport Cost
1. Pump large amount gas
2. Pump small amount gas
3. Pump large amound fluid
4. Pump small amount fluid
Blank is very large cost

E. Safety
1. Very safe
2. Hazardous to personnel
3. Risk of fire
4. Very hazardous
Blank is possibility of catastrophic failure

F. Corrosion
1. No problems
2. Stainless steel good
3. Some corrosion
4. Medium amount corrosion
Blank is very serious corrosion problems

G. Fluid Cost
1. Free
2. Low cost - very little replacement
3. Low cost - some replacement
4. Medium cost
Blank is very high cost

H. Versatility
1. Open or closed fluid
2. Adaptable to storage
3. Direct use in turbine
4. Simple controls

I. Work Conversion Efficiency
1. ≈40%
2. ≈35%
3. ≈30%
4. >20%
Blank is very low efficiency

Key for Figure 4-1

It appears that minimal corrosion occurs with Hitec in common carbon steel piping at temperatures below 727 K (850°F), but stainless steel should be used at the higher temperatures (up to 811 K, 1000°F). Above about 727 K (850°F), two reactions proceed slowly, the rate increasing with increasing temperature.

1. $2NaNO_2 + O_2 \text{ (air)} \rightarrow 2NaNO_3$

2. $5NaNO_2 \rightarrow 3NaNO_3 + Na_2O + N_2$

The first reaction can be suppressed by blanketing with nitrogen. If necessary, most of the air can be excluded by maintaining a slight overpressure of nitrogen in the cavity. Findings of various investigators indicate that the second reaction probably does not proceed at an excessive rate at temperatures up to about 811 K (1000°F). The effect is a gradual raising of the melting point. Further investigation of these and other possible reactions, along with evaluation of absorption and heat transfer characteristics under anticipated use conditions, is planned as part of the development program.

Central Absorber Configuration

The absorber can have either an internal surface (a cavity), an external surface, or a combination of the two. This study indicated that the efficiency of an external absorber would be much lower and would present many design problems. Figure 4-2 is a plot of theoretical absorber efficiency vs. flux density for external and internal absorbers neglecting convection losses. An absorptivity of 0.95 (metal at high temperature or lampblack) and a temperature of 540°C (1000°F) were assumed. Also plotted is an absorptivity of 0.90. Two different cavity designs are shown. One is with a terminal concentrator (explained later) and one is without the concentrator. This plot shows that in order to get high efficiency with an external absorber, the incident flux density must be very high, on the order of 945 kW/m^2 (300,000 Btu/hr ft^2) and even then the efficiency is 92.5% compared with the efficiency of a cavity at 94.0% with no concentrator. Notice, however, the main advantage of the cavity is that as flux density is decreased for more reliable engineering, the efficiency of a cavity increases. If the absorber surface is designed for 315 kW/m^2 (100,000 Btu/ft^2 x hr), an efficiency of up to 96.5% can be achieved with a cavity.

In these comparisons, cavity convection losses are neglected since the outer surface can be well insulated and because the vertical orientation inhibits natural convection through the aperture. An external absorber, however, has significant convection losses over the absorbing area; these losses have been estimated at 5 kW/m^2 (1600 Btu/hr ft^2) for natural convection and an additional loss of about 3.15 kW/m^2 (1000 Btu/hr ft^2) for a wind of 18 m/s (40 mph).

If a flux density of 945 kW/m^2 (300,000 Btu/hr ft^2) is assumed, the efficiency of an external absorber would be about 92.0% at full power ignoring forced convection. A cavity designed for 315 kW/m^2 (100,000 Btu/hr ft^2) would have an efficiency of 96%. These efficiencies appear to be quite high and approximately equal. However, an absorber usually does not operate at full power and except for reflection, losses remain essentially constant regardless of input power. For the same designs at 20% of full power, the efficiencies are about 80% for an external absorber and 88% for a cavity. Figure 4-3 is a plot of efficiency at partial power. The winter peak flux is about 78% of summer peak so the maximum winter efficiency of a cavity would be about 96% and an external absorber would be 91%.

In addition to the efficiency considerations, a cavity would have other advantages. It may be possible to keep the cavity warm overnight thus reducing the thermal stresses from a cold start and maintaining readiness to accept solar energy. An external absorber will have thermal stresses affected by wind direction, temperature, and velocity, and by rainfall.

A number of design studies were performed for cavity configurations in which a heat transfer fluid was circulated through pipes heated by the solar flux. In addition, a less conventional, alternative method was devised in which the solar energy is absorbed directly within a liquid film flowing down the cavity walls. This has the following advantages:

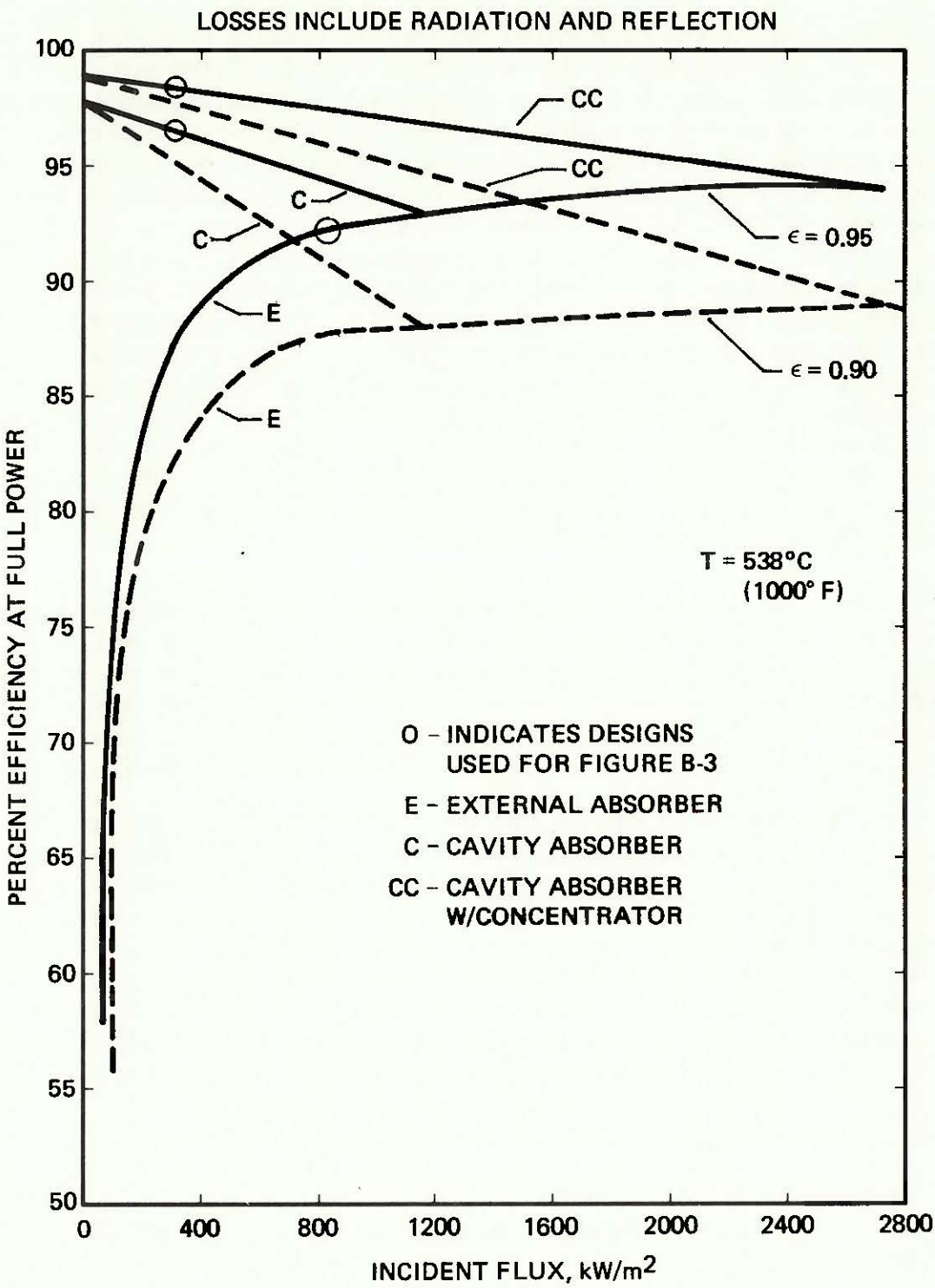

Figure 4-2. Absorber Efficiency Versus Incident Flux

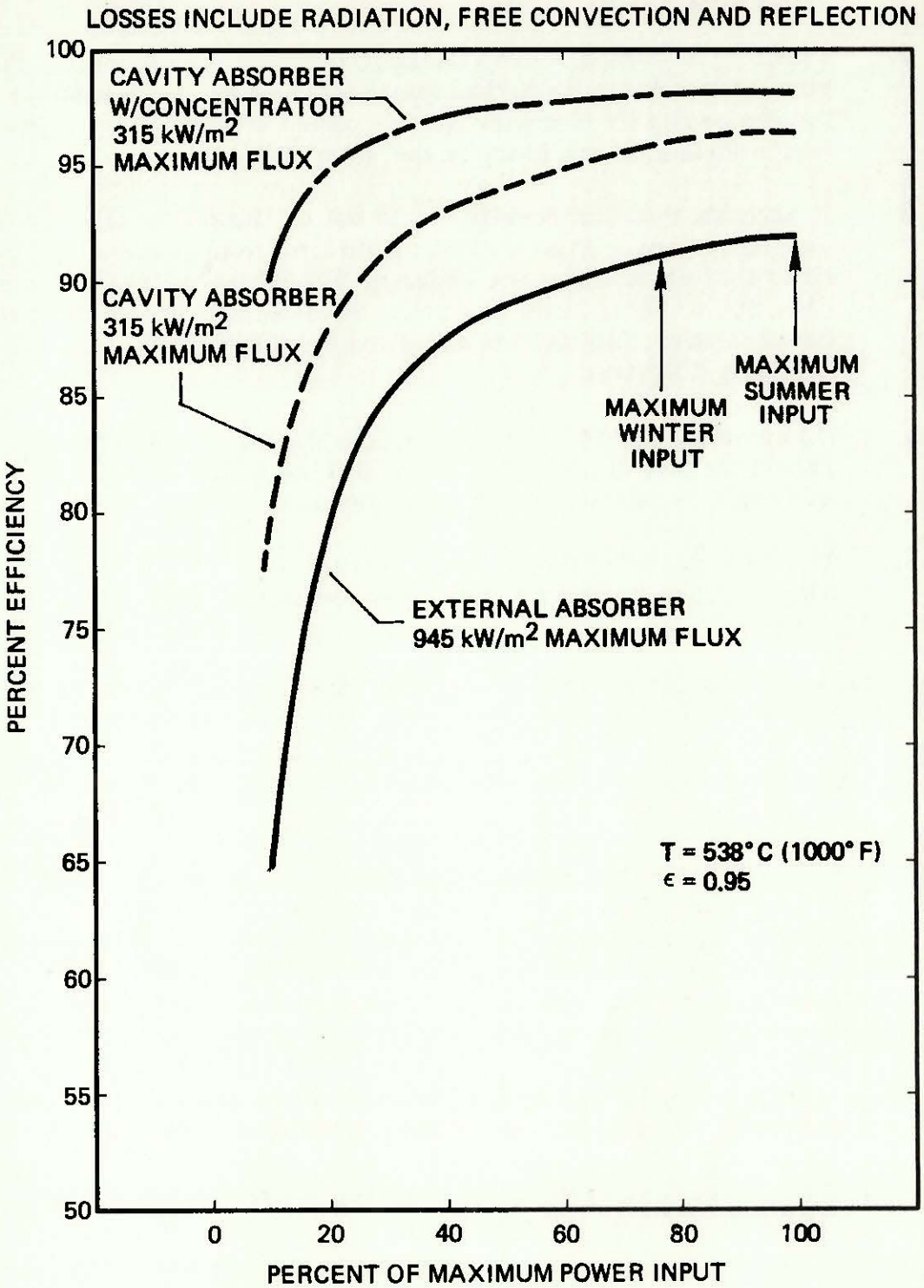

Figure 4-3. Absorber Efficiency as a Function of Input Power

1. The cavity weight is less.

2. There is no temperature differential across a pipe wall. This results in a lower radiation temperature (higher efficiency) for the cavity or in higher quality output energy giving higher thermodynamic efficiency in the steam turbine.

3. It appears that flux density would not be limited by materials considerations. Pipe wall and fluid film temperatures normally limit flux densities to the order of 315 kW/m^2 to 945 kW/m^2 (100,000 to 300,000 Btu/hr ft^2). With no pipe and no fluid film heat transfer, higher flux densities can probably be accommodated if desired.

4. If refractory walls were used behind the fluid, unexpected excessive flux or pump failure would not cause a cavity failure such as tube burnout which could occur in a steam boiler system.

5. The inlet to outlet temperature increase can be relatively large. This reduces mass flow rate, pipe diameter, and fluid inventory.

Several problem areas would have to be investigated and resolved:

1. The fluid must operate at atmospheric pressure in the cavity. This eliminates steam, the terphenyls, and most of the liquid metals because of high vapor pressures at high temperature.

2. The fluid must not be degraded rapidly by the surrounding gas at high temperatures. A blanket gas can be used in the cavity to displace most of the air, if air is a problem. This consideration, however, eliminates rapidly oxidizing or flammable materials such as sodium, potassium, and the terphenyls.

3. The fluid must have the correct optical density to absorb the energy in depth. If Hitec were used, for instance, a doping material would have to be added to increase its opacity.

4. More investigation would be required for nozzle design and downward-flowing fluid films.

Terminal Concentrator

In a cavity, it appears that the flux density at the aperture would be about 1.1 MW/m^2 (365,000 Btu/hr ft^2). This is determined by mirror density, rim angle, aiming errors, mirror abberations, and finite sun size. Analyses indicate that by adding a terminal concentrator the aperture size

can be decreased thereby increasing the efficiency. The following analysis shows how a terminal concentrator can be used to reduce aperture size.

For an array of mirrors reflecting solar energy directly into the aperture of a cavity absorber, the concentration ratio C is given by:

$$C = \frac{A_m}{A_i} = \psi\left(\frac{\sin 2\,\phi_m}{\beta}\right)^2 = \psi\left(\frac{R_m}{R_i}\right)^2$$

where

A_m = area of mirrors

A_i = area of aperture

ψ = mirror area to ground area ratio

ϕ_m = rim angle

β = total angle of divergence of rays reflected from a point on the surface of the most distant mirror

C is therefore, maximum when the rim angle ϕ_m equals 45 degrees. Because the collected energy is proportional to R_m^2, however, it is advantageous to increase ϕ_m if the decrease in C can be tolerated.

A terminal concentration scheme has been devised which not only increases the concentration ratio for all values of ϕ_m, but also causes the maximum to occur at a significantly larger value of ϕ_m. A conical reflector is placed at the aperture as shown in Figure 4-4.

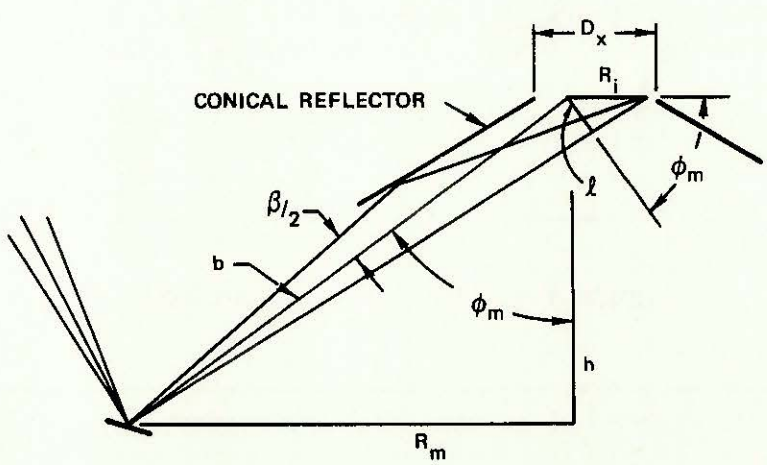

Figure 4-4. Terminal Concentrator

The included angle of the conical reflector is slightly greater than $2\phi_m$. The beam from each of the distant mirrors is aimed so that the far edge of the beam just enters the aperture. The near edge of the beam grazes the conical reflector and is reflected through the aperture. The beam is essentially "folded" in half such that it will pass through a smaller aperture (see Figure 4-5).

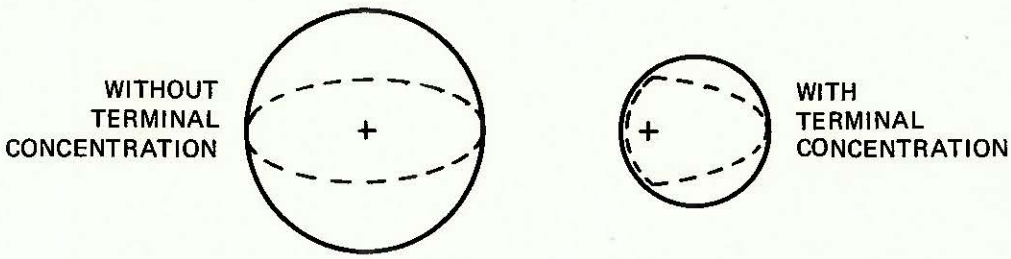

Figure 4-5. Cross-Section of Beam at Aperture

Losses at the terminal concentrator are minimal since (1) only a portion of the beam is reflected, (2) the grazing angle is very small, and (3) beams from interior mirrors require little or no terminal concentration.

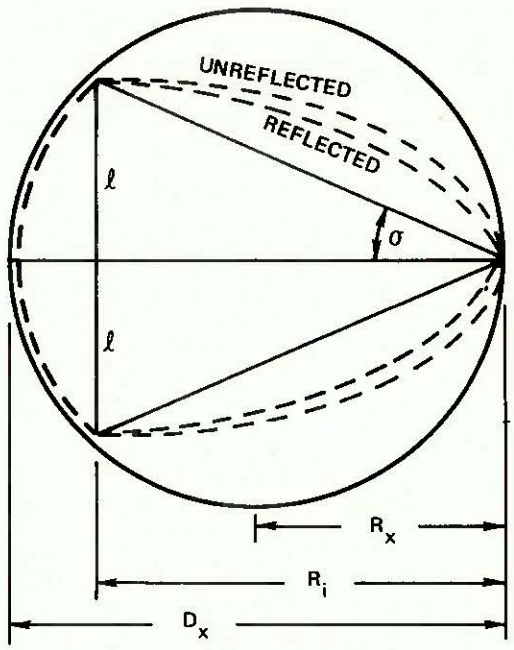

Figure 4-6. Beam/Aperture Geometry

From Figure 4-4: $\cos \phi_m = \ell / R_i$

From Figure 4-6: $\tan \sigma = \ell / R_i$

$$\tan \sigma = \cos \phi_m$$

$$\sigma = \tan^{-1} \cos \phi_m$$

From trigonometric relationship in Figure 4-6, the aperture diameter D_x is

$$D_x = \frac{2\ell}{\sin 2\sigma}$$

$$R_x = \frac{\ell}{\sin 2\sigma}$$

The radius of the beam from the most distant mirror ℓ is

$$\ell = b \tan \beta / 2$$

$$\beta = \alpha + 2\beta_0 + 2\beta_e$$

where b is the distance from the most distant mirror to the aperture, and β is the total angular allowance for the subtended sun angle (α = 0.0093 rad), mirror alignment error β_0, and mirror aberration error β_e.

$$b = \frac{R_m}{\sin \phi_m}$$

by substitution

$$R_x = \frac{R_m \tan \beta / 2}{\sin \phi_m \sin 2\sigma}$$

Substituting for σ, and for $\beta/2$ small:

$$\frac{R_m}{R_x} = \frac{\sin \phi_m \sin 2 \tan^{-1} \cos \phi_m}{\beta / 2}$$

The concentration ratio C_T (with terminal concentration) is therefore:

$$C_T = \frac{A_m}{A_x} = \psi\left(\frac{2 \sin \phi_m \sin 2 \tan^{-1} \cos \phi_m}{\beta}\right)^2$$

The concentration ratio is shown in Figure 4-7 as a function of ϕ_m, with and without terminal concentration, for representative values of β and γ. Note that the maximum value of C_T is twice that of $C_{(max)}$, and that $C_{T(max)}$ occurs at about 55 degrees. At 55 degrees C_T is about 2-1/4 times greater than C, about 2-1/2 times greater at 60 degrees and almost 3 times greater at 65 degrees. Design relationships for the conical reflector are shown in Figure 4-8.

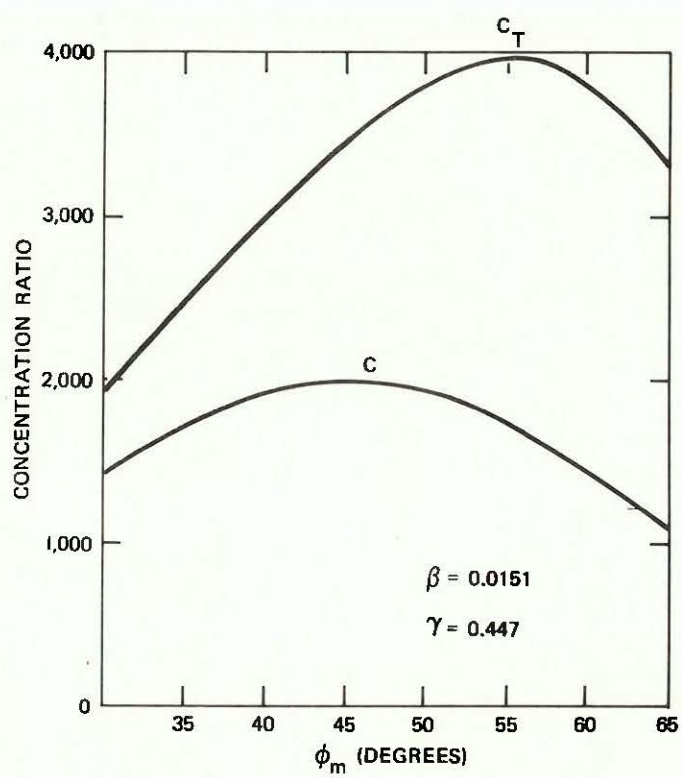

Figure 4-7. Concentration Ratio vs Mirror Field Rim Angle

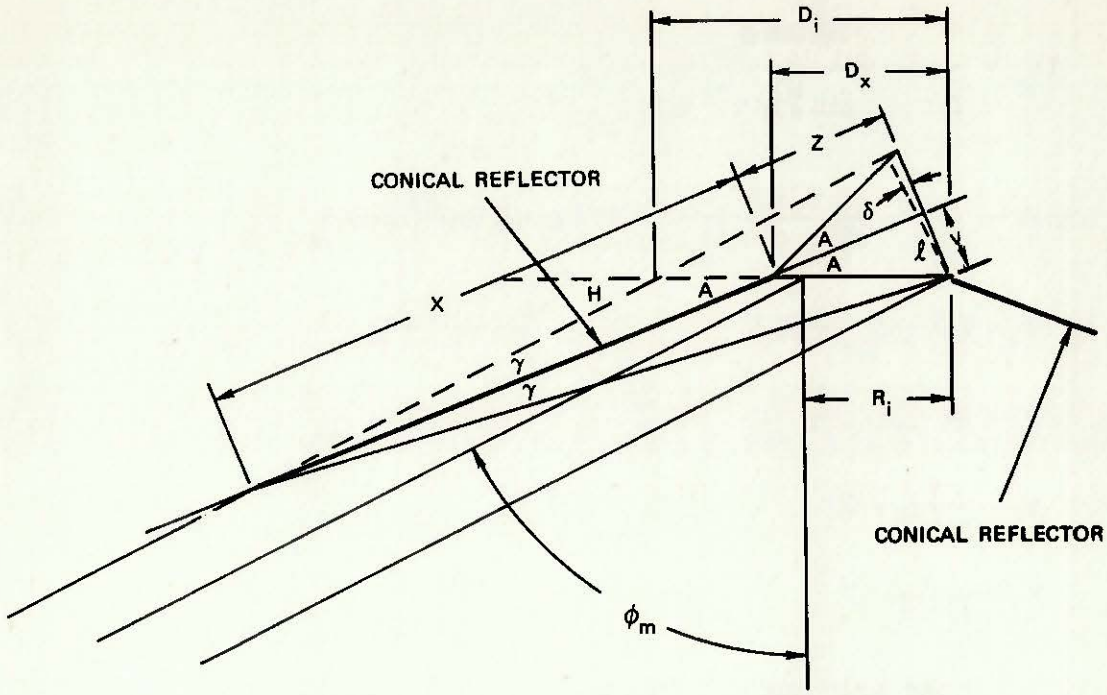

Figure 4-8. Design Relationships for the Conical Reflector

From Figure 4-8:

$$v = \frac{\ell}{\cos\delta} \approx \ell \qquad \left(\text{error less than } \begin{matrix} 1.5\% \text{ for } \delta < 10° \\ 0.4\% \text{ for } \delta < 5° \end{matrix}\right)^*$$

δ = angle between v and ℓ = $90 - \phi_m - A = \gamma - \beta/2$

$$\ell = b \tan\beta/2 \approx \frac{b\beta}{2} \text{ (for } \beta/2 \text{ small)}$$

$$b = \frac{h}{\cos\phi_m}$$

$$v = \frac{h\beta}{2\cos\phi_m}$$

*The error resulting from this approximation increases as the rim angle ϕ_m is decreased; however, in the range of primary interest (55 to 65°) the approximation is sufficiently accurate.

$$D_x = \frac{h\beta \tan \phi_m}{\sin \phi_m \sin 2 \tan^{-1} \cos \phi_m}$$

$$\sin A = \frac{v}{D_x} = \frac{h\beta}{2 D_x \cos \phi_m} = 1/2 \sin 2 \tan^{-1} \cos \phi_m$$

$$H = 90 - \phi_m + \beta/2$$

$$\gamma = H - A$$

$$x = \frac{v}{\tan \gamma} - Z$$

$$Z = \frac{v}{\tan A}$$

J = cone half-angle = 90-A

R_c = base radius of cone = $x \sin J + R_x$

A_c = area projected by cone = πR_c^2

A_g = ground area of mirror field = $\pi (h \tan \phi_m)^2$

Design parameters are given in Table 4-1 over a range of values of rim angle ϕ_m.

TABLE 4-1. DESIGN PARAMETERS TERMINAL CONCENTRATOR

ϕ_m (deg)	D_x (m)	C_T	A (deg)	γ (deg)	v (m)	X (m)	J (deg)	A_c (m^2)	A_g (m^2)	$\frac{A_c}{A_g}$
40	2.042	3020	28.87	21.56	0.986	0.71	61.13	8.4	2.2×10^4	0.0004
45	2.265	3485	28.13	17.30	1.068	1.41	61.87	17.7	3.14×10^4	0.00056
50	2.582	3808	27.06	13.37	1.175	2.64	62.94	42	4.45×10^4	0.00094
55	3.050	3920	25.57	9.86	1.316	4.82	64.43	108	6.0×10^4	0.0018
60	3.775	3764	23.58	6.85	1.510	9.11	66.42	329	9.4×10^4	0.0035
63	4.418	3528	22.11	5.32	1.663	13.76	67.89	702	12.1×10^4	0.0058
65	4.982	3312	21.01	4.42	1.786	18.45	68.99	1220	14.4×10^4	0.0085

β = 0.0151 rad

ψ = 0.447

h = 100 m

One of the problems with the terminal concentrator is weight. A cavity without a concentrator is estimated to be about 180 kg/kW_t (396 lb/kW_t) and the concentrator adds about 500 kg/kW_t (1100 lb/kW_t). For a collection temperature of 540°C, it is not yet clear whether the weight penalty is justified economically. Therefore, we have elected not to use it on the baseline system. Systems analysis and more technical development will ultimately determine the practicality of the concentrator concept.

Baseline Cavity Design

The following presentation is the baseline system describing a practical concept for the point focus system.

Solar power input at cavity aperture:	335 MW_t peak summer 280 MW_t peak winter
Integrated energy output to steam generator:	Summer, 3182 MW_th per day Winter, 1780 MW_th per day
Tower height:	300 meters (984 ft)
Cavity dimensions:	
Inside diameter	18.7 meters (61.4 ft)
Aperture diameter	18.1 meters (59.4 ft)
Cavity wall height	21.5 meters (70.5 ft)
Droop angle of ceiling	0.62 rad (35.5°)
Ceiling height at center	14.8 meters (48.6 ft)
Cavity weight	60,000 kg (66 tons)
Cavity performance:	
Heat transfer fluid	DuPont HITEC
Inlet temperature	204°C (400°F)
Outlet temperature	510°C (950°F)

Wall cooling - film flowing down walls

Ceiling cooling - refractory ceiling with radiation cooling

Collection efficiency* - 91% at full power
78% at 10% of full power

* Output thermal power divided by solar power redirected by mirror field. Includes 4% allowance for shadowing by cavity supports.

	Peak Input	10% of Peak
Input flux, MW_t	330	38.6
Output thermal power, MW_t	300	30
Nominal film thickness, mm (in)	2.54 (0.1)	0.71 (0.028)
Mass flow rate, kg/s (lb/s)	637 (1385)	63.7 (138.5)
Volume flow rate, m^3/s (gpm)		
Input	0.325 (5164)	0.032 (516)
Output	0.367 (5830)	0.0367 (583)
Cavity fluid transit time, s	9	26
Inlet pipe		
Inside diameter, mm (in)	287 (11.3)	287 (11.3)
Weight with fluid, kg (tons)	60,781 (67)	60,781 (67)
Fluid velocity, m/s (fps)	4.57 (15)	0.457 (1.5)
Friction loss, kPa (psi)	206.8 (30)	7 (1)
Outlet pipe		
Size, mm (in)	287 (11.3)	287 (11.3)
Weight with fluid, kg (tons)	54,430 (60)	54,430 (60)
Fluid velocity, m/s (fps)	5.11 (16.76)	0.511 (1.7)
Friction loss, kPa (psi)	365 (53)	7 (1)
Pumping horsepower, hp	1000	50
Electrical power required, kW	746	37
Percent of input power required for pumping	1.0%	0.5%

A schematic of the cavity, heat transpoort loop, and associated equipment is shown in Figure 4-9. This design has been built around the following criteria:

1. Atmospheric pressure at the cavity to allow for open fluid flow.

2. Low pressure Hitec in the storage loop.

3. Separation of the two Hitec loops so that if any degradation of Hitec occurs in the cavity it will not deteriorate the Hitec in the storage loops. Also reduces amount of fluid that requires doping.

4. The Hitec piping to the tower will be kept warm (204°C) throughout the night to simplify morning startup.

5. Storage tanks are not at high pressure and high temperature.

6. All pumps are at low temperature (204°C)

7. Full fossile backup to allow for lack of solar input.

8. Thermal storage capability to allow flexibility in operations.

9. Minimum use of fossile fuel.

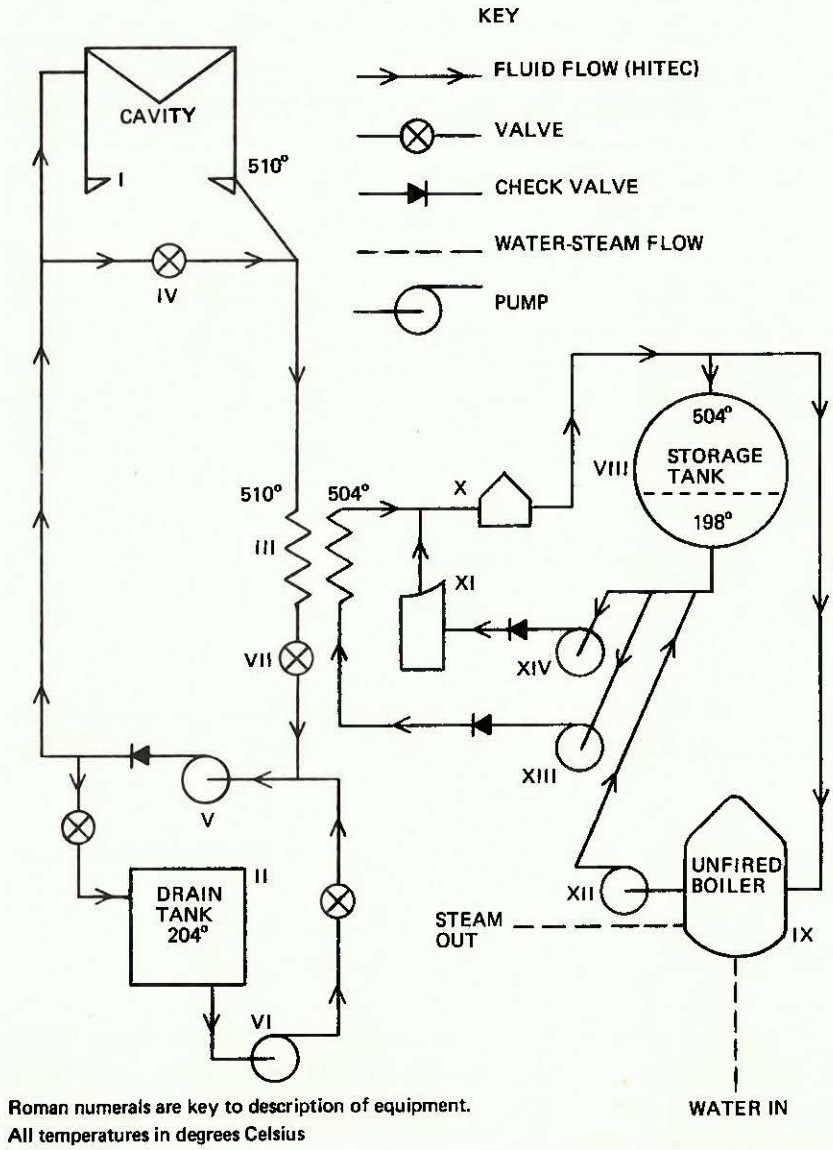

Figure 4-9. Major Equipment Schematic

I.	Hitec Buffer Sump Sump Width - 0.5 (1.64 ft) Sump Depth - 0.34 (1.17 ft) Volume - 10m^3 (353 ft^3)	Stores excess Hitec to allow for expansion and contraction and flow rate variations.
II.	Hitec Drain Tank Pressure - 120 kPa (17 psi) Temperature - 204°C (400°F) Volume - 55m^3 (1943 ft^3)	Stores Hitec from entire cavity loop for maintenance shutdown.
III.	Heat Exchanger Pressure Cavity Side - 7000 kPa (1015 psi) Storage Side - 700 kPa (100 psi)	Allows storage to be at lower pressure and keeps doped Hitec only in cavity loop.
IV.	Shunt Line and Valve Pressure - 700 kPa (100 psi) Temperature - 204°C (400°F)	Allows shunting Hitec when no solar input to keep lines heated.
V.	Cavity Circulation Pump Static Heat - 7000 kPa (1015 psi) Dynamic Head - 1200 kPa (175 psi) Max. Flow Rate - 0.325 m^3/s (5164 gpm) Max. Power - 746 kW (1000 HP)	Supplies pumping power to send Hitec through cavity loop. Controls cavity output temperature by flow rate variation.
VI.	Charging Pump Static Head - 7000 kPa (1015 psi) Dynamic Head - 7000 kPa (1015 psi)	Charges cavity loop from drain tank.
VII.	Return Line Control Valve	Controls level of Hitec in return line.
VIII.	Storage Tank Pressure - 290 kPa (42 psi) Capacity - 117 MW_th (4E8 Btu) Hitec Weight - 912,577 kg (1000 tons) Cost of Hitec - $320,000 Volume of Tank - 536m^3 (18,290 ft^3)	Provides storage for 27 minutes of full power operation at 110 MW_e.
IX.	Unfired Boiler Hitec Pressure - 700 kPa (100 psi) Water Pressure - 4481 kPa (650 psi)	Produces steam for turbine.
X.	Temperature Regulator Pressure - 700 kPa (100 psi) Temperature - 504°C (940°F)	Guarantees 504 C Hitec into storage. Electrically heated.
XI.	Hitec Heater Pressure - 700 kPa (100 psi) Thermal Capacity - 200 MW_t	Can replace solar input to increase inventory of hot Hitec. Fossil fuel fired.
XII.	Boiler Circulation Pump Capacity - 0.22m^3/s (3442 gpm)	Circulates Hitec from storage to the boiler.
XIII.	Hitec Solar Heat Loop Pump Capacity - 0.325m^3/s (5164 gpm)	Circulates Hitec from storage to heat exchanger and back to storage.
XIV.	Hitec Fossil Heat Loop Pump Capacity - 0.11m^3/s (1721 gpm)	Circulates Hitec from storage to Hitec fossil heater and back to storage.

Key for Figure 4-9

4.2 The Temperature of Cavity-Type Solar Absorbers With a Circulating Fluid

This section provides a simple analytical expression for the effective temperature of a cavity-type absorber of radiative energy when a heat transfer fluid is circulated through the cavity. The effective temperature is that temperature which characterizes the radiative emission loss from the cavity aperture and which drives the absorbed energy into the heat transfer fluid. The analysis is intended for use in estimating the effective cavity temperature (and thereby rank-ordering various cavity design options) and is not intended to supplant any detailed numerical calculations for the temperature distribution.

The model of the cavity under consideration is shown in Figure 4-10. Fluid flowing at the rate $\dot{m}$ passes between the walls of the cavity and a perfectly insulated casing, and, by convective heat exchange, experiences the temperature rise $(T_{f,o} - T_{f,i})$. Diffuse radiative flux, assumed to be uniformly distributed over the aperture area, enters the cavity where it is partially absorbed, and this absorbed energy is conducted through the cavity wall into the heat transfer fluid.

In two previous analyses of cavity-type absorbers [1, 2], performance was assessed for an assumed temperature distribution over the interior surface area of the cavity. Actually, however, in many applications, the cavity temperature can be strongly influenced by the presence of the heat transfer fluid, and hence, any a priori specification of this temperature can be very uncertain. In general, a numerical solution for the cavity temperature distribution, such as that reported in [3], is required.

The principal assumptions made are as follows. All physical properties are independent of temperature and are constants; reflectivity and emissivity are independent of wavelength; the interior surface of the cavity emits and reflects energy in a diffuse manner; and the temperature distribution over this surface is uniform and corresponds to the effective cavity temperature. While a uniform cavity temperature is approached only under certain limiting situations,* this assumption is made because it leads to an extremely simple analytical result which accounts for all of the pertinent energy transfer processes: emission and reflection of energy from the cavity, conduction of energy through the cavity walls, and convection of energy by the heat transfer fluid. No restriction is placed upon the shape of the cavity, however, since the effects of cavity shape are incorporated into the apparent emissivity

---

*A uniform cavity temperature is approached as the effective conductance of the cavity wall decreases, fluid flow rate decreases, and radiative input to the cavity increases.

for that shape. (Literature sources for the apparent emissivities of various cavity shapes are cited later.) If the apparent emissivity is unknown for the particular cavity being considered, it can be estimated as described herein.

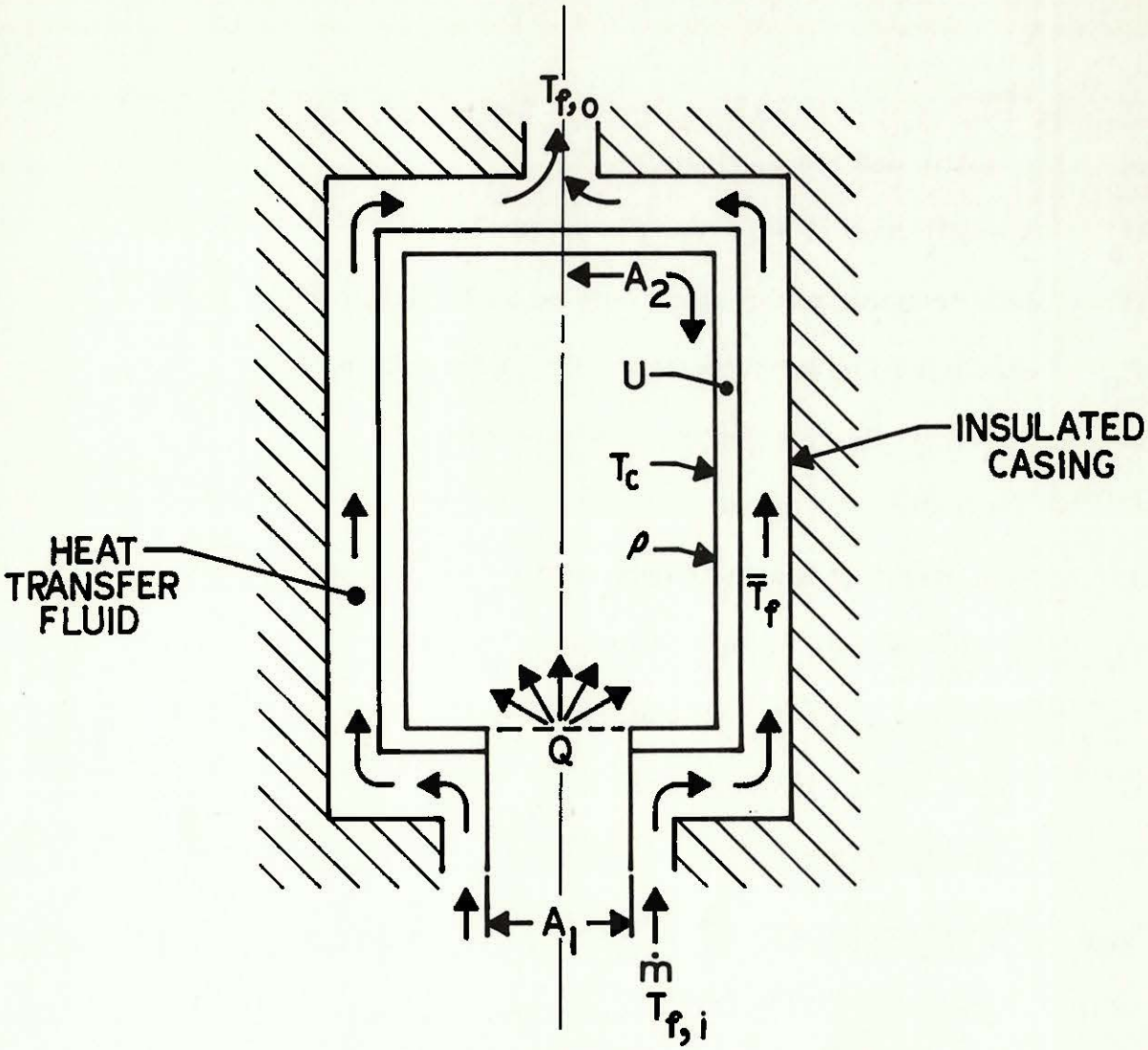

Figure 4-10. Radiation-Conduction-Convection Heat Transfer Model of Solar Radiation Cavity

Nomenclature

A	area
B	quantity defined by Equation (9)
C_p	specific heat of heat transfer fluid
D	heat transfer parameter, defined by Equation (8)
F_{ij}	configuration factor between the surfaces i and j
G	radiative flux incident upon cavity wall
H	parameter, $UA_2/(\dot{m}C_p)$
J	radiative flux leaving cavity wall
$\dot{m}$	mass flow rate of heat transfer fluid
Q	radiative flux entering aperture
R	radiative flux leaving aperture
T	absolute temperature
T_{ref}	reference temperature defined by Equation (6)
t	dimensionless temperature, T/T_{ref}
U	overall heat transfer coefficient
u	dimensionless overall heat transfer coefficient, $U/(\sigma T_{ref}^3)$
Y	parameter defined by Equation (10)
ϵ	emissivity
ρ	reflectivity
σ	Stephan-Boltzmann constant

Subscripts

a	apparent
c	cavity
f	fluid
i	inlet
o	outlet
1	refers to aperture area
2	refers to area of interior surface of cavity

Superscript

-	refers to average of a quantity

Theory

An energy balance at the plane of the aperture requires that the difference between the incoming and outgoing radiative energies equals the energy conducted through the cavity wall, i.e.,

$$(Q - R)A_1 = UA_2(T_c - \overline{T}_f) \tag{1}$$

where U is the effective conductance of the wall plus wall-fluid boundary. The radiative flux leaving the cavity R is simply the sum of the reflected and emitted fluxes and is expressed as

$$R = (1 - \epsilon_a)Q + \epsilon_a \sigma T_c^4 \tag{2}$$

The apparent emissivity ϵ_a is a function of the actual emissivity of the cavity interior (ϵ), and the cavity geometry. Sparrow and Cess [4] give graphs of ϵ_a for cylindrical, conical, and spherical cavities. (Results for the cylindrical and conical cavities are based upon numerical solutions of integral equations, while the results for the spherical cavity are based upon the analytical solution of Reference 5.) When dealing with cavity shapes for which there are no data for ϵ_a, it is possible to estimate ϵ_a by assuming that the cavity behaves as a two-zone enclosure (the zones being A_2, the cavity interior surface area, and the fictitious surface formed by A_1, the area of the aperture; see Figure 4-10). Under this assumption* it can be shown that

$$\epsilon_a = 1/[1 + (A_1/A_2)(\rho/\epsilon)] \tag{3}$$

Eliminating R between Equations (1) and (2) yields the result

$$\sigma T_c^4 + U(T_c - \overline{T}_f)(A_2/A_1)/\epsilon_a - Q = 0 \tag{4}$$

---

*The zonal approach implies that the effective radiative flux leaving each zone is the area-averaged flux leaving that zone. Similarly, the effective irradiation of each zone is assumed to be the area averaged irradiation over that zone.

The temperature difference appearing in Equation (4) is the so-called log-mean temperature difference (LMTD) which arises in heat exchanger theory. Omitting the details for brevity, it can be shown by an energy balance of the heat transfer fluid [6, p. 301] that,

$$(T_c - \overline{T}_f) = (\dot{m}C_p/UA_2)(T_c - T_{f,i})[1 - \exp(-UA_2/\dot{m}C_p)] \tag{5}$$

Substituting Equation (5) into (4), and then normalizing the temperature by T_{ref} where

$$T_{ref} = (Q/\sigma)^{1/4} \tag{6}$$

results in

$$t_c^4 + (t_c - t_{f,i})\, u\,(A_2/A_1)(1/\epsilon_a)\,[1 - \exp(-H)]/H - 1 = 0 \tag{7}$$

Physically, T_{ref} is the temperature which would be attained by the cavity in the absence of heat transfer to the fluid.

Equation (7) is a quartic equation which, as indicated below, has an exact solution. First, the role of the various terms in this equation is briefly commented upon. The first term represents energy loss from the cavity by emission; the second term is a measure of energy transfer to the fluid and cavity reflection losses; and the constant term (-1) is the dimensionless radiative flux input to the cavity. When the coefficients of $(t_c - t_{f,i})$ are small (compared to unity), heat transfer from the cavity by mechanisms other than emission is small, and the cavity temperature approaches its theoretical maximum value, e.g., $t_c = 1$. On the other hand, when these coefficients become large, the limit $t_c = t_{f,i}$ is approached.

The solution of Equation (7) is obtained following the method outlined in [7]. With the quantities D, B, and Y respectively defined as

$$D = u(A_2/A_1)(1/\epsilon_a)[1 - \exp(-H)]/H \tag{8}$$

[the coefficient of $(t_c - t_{f,i})$ in Equation (7)]

$$B = \left\{1 + [(Dt_{f,i} + 1)/3]^3 (4/D)^4\right\}^{1/2} \tag{9}$$

and

$$Y = (D^2/2)^{1/3}[(B + 1)^{1/3} - (B - 1)^{1/3}] \tag{10}$$

the solution is found to be

$$t_c = (1/2)[(2D/Y^{1/2} - Y)^{1/2} - Y^{1/2}] \tag{11}$$

Results

The solution of Equation (7) is plotted in Figure 4-11 as a function of the heat transfer parameter D for several values of the dimensionless fluid inlet temperature $t_{f,i}$. This graph may be employed to obtain the temperature of any cavity shape for which the apparent emissivity is known. If the apparent emissivity for the cavity shape of interest is unknown, it may be estimated from Equation (3). Once t_c has been determined, the dimensionless temperature rise experienced by the heat transfer fluid may be computed from

$$t_{f,o} - t_{f,i} = (t_c - t_{f,i})[1 - \exp(-H)]$$

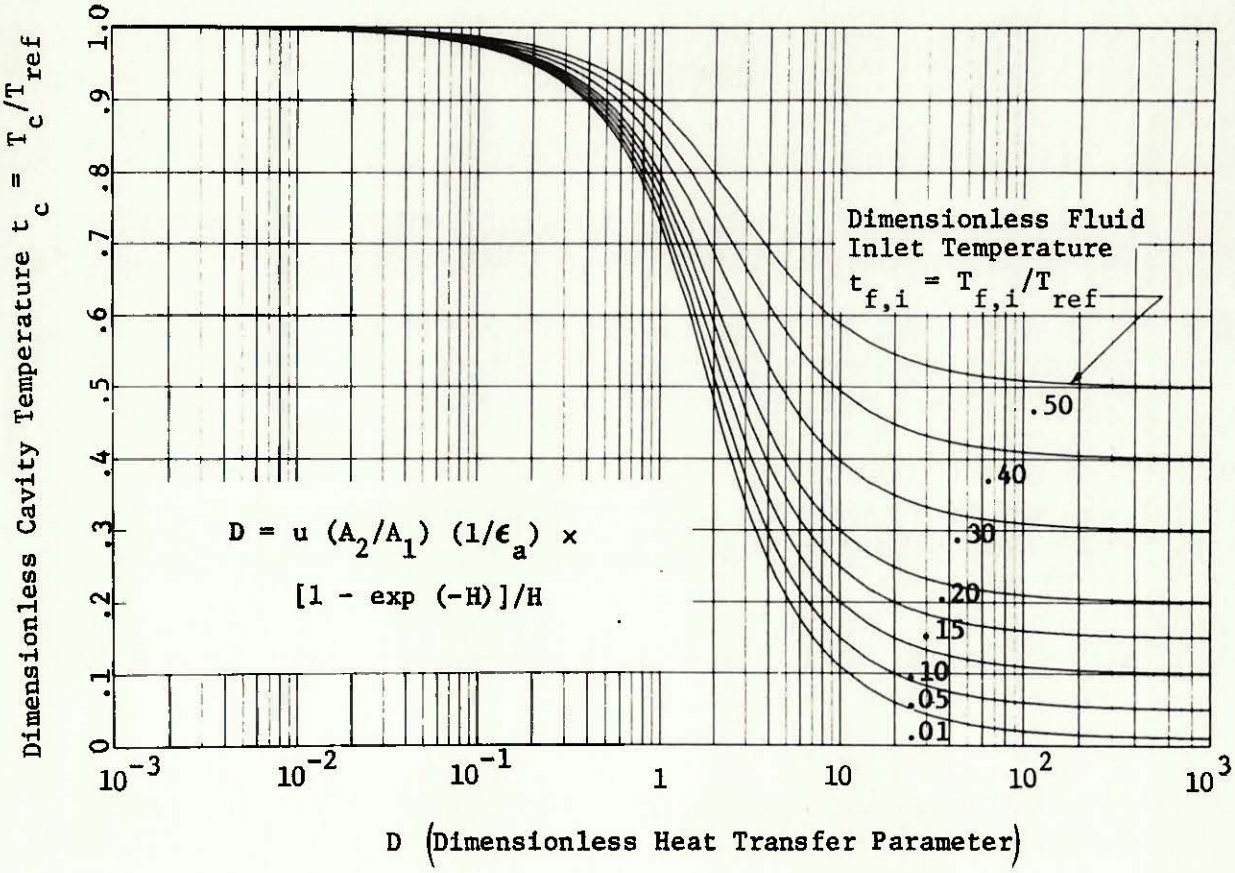

Figure 4-11. Dimensionless Cavity Temperature as a Function of the Heat Transfer Parameter D

REFERENCES

1. C. W. Stephans, A. M. Haire, "Internal Design Consideration for Cavity-Type Solar Absorbers," ARS Journal, pp. 896-901, July 1961.

2. V. A. Grilikhes, F. V. Obtemperanskii, "Analysis of Radiative Heat Exchange Processes in Cylindrical Cavity-Type Collectors of Solar Power Plants," Appl. Solar Energy, 5, No. 1-2, pp. 59-65 (1969).

3. F. V. Obtemperanskii, V. A. Grilikhes, "Approximate Thermal Calculations for Cylindrical Cavity-Type Collectors with Liquid-Metal Heat-Transport Medium," Appl. Solar Energy, 5, No. 3-4, pp. 61-65 (1969).

4. E. M. Sparrow, R. D. Cess, Radiation Heat Transfer, pp. 163-170, Brooks/Cole Publishing Co., Belmont, CA (1967).

5. E. M. Sparrow, V. K. Jonsson, "Absorption and Emission Characteristics of Diffuse Spherical Enclosures," Trans. ASME, J. Heat Transfer, C 84, pp. 188-189 (1962).

6. J. P. Holman, Heat Transfer, Second Edition, McGraw-Hill, New York (1968).

7. S. M. Selby, Editor, Standard Mathematical Tables, Nineteenth Edition, p. 106, The Chemical Rubber Co., Cleveland (1971).

4.3 Design of a Cavity Experiment to Confirm Analytical Predictions

For any of the proposed concepts of cavity design, it is ultimately necessary to predict the temperature and heat flux distribution over the interior surface of the cavity. Unfortunately, to make such predictions requires consideration of phenomena not normally dealt with in heat exchanger design. For instance, one must take into account the asymmetric irradiation of the cavity interior by the incident sunlight; the reflection and emission of radiant energy by surfaces which have wave-length dependent properties; the free convection of air within the cavity volume; and the forced convection of energy to the heat transfer fluid. In fact, there is no known published analysis which has considered these phenomena acting simultaneously. It is, therefore, essential that any new theoretical analysis developed to predict the behavior of a full-sized cavity be verified experimentally. Construction of bench-top models of the solar cavities (corresponding to the various cavity design concepts) is consequently recommended.

The best approach to establishing a reliable theoretical model of a full-sized cavity is to start with a very simple laboratory model (and accompanying analysis) and progress toward a more realistic laboratory cavity and its analytical description.

A very simple bench-top model of a solar cavity, currently under construction at Sandia Laboratories, is described in this section. Temperatures and heat fluxes measured in the laboratory model will be compared to the predictions of potential theoretical models as a means of verifying the latter.

Description of Apparatus--The apparatus being assembled at Sandia Laboratories consists of a radiation-absorbing cavity and a xenon arc lamp energy source (Figures 4-12 and 4-13). The cavity is cylindrical with an aperture at one end and a set of moveable shields at the other end. A heat transfer fluid (helium) flows upward in the annular space between the cavity and a concentric cylindrical outer casing, and becomes heated by the absorbed radiant energy which is conducted across the cavity wall. After exiting the cavity, the hot helium is cooled by a heat exchanger and recirculated through the cavity.

Most of the energy radiated from the arc lamp is focused on the cavity aperture by an ellipsoidal mirror. A small fraction of the radiated energy, however, passes directly out of the mirror enclosure without being focused. This unfocused energy is absorbed on a water-cooled shield located between the mirror and cavity.

The mirror-lamp system is designed to focus up to 12,000 watts of radiant energy into a 2-1/2 inch diameter cavity aperture. At this power level, fluid temperature rises of the order of 540°C can be obtained. Power input to the cavity will be measured at the start of each test by a calorimeter placed across the aperture. Temperatures at selected locations on the cavity wall will be measured by thermocouples; local irradiation of the cavity wall will be measured by foil-type heat flow sensors. Input power level, cavity length, and mass flow rate will be treated as parameters.

The experiments will be conducted inside an environmental chamber where the ambient pressure can be controlled. Initially, experiments will be conducted under vacuum to preclude natural convection within the cavity volume.

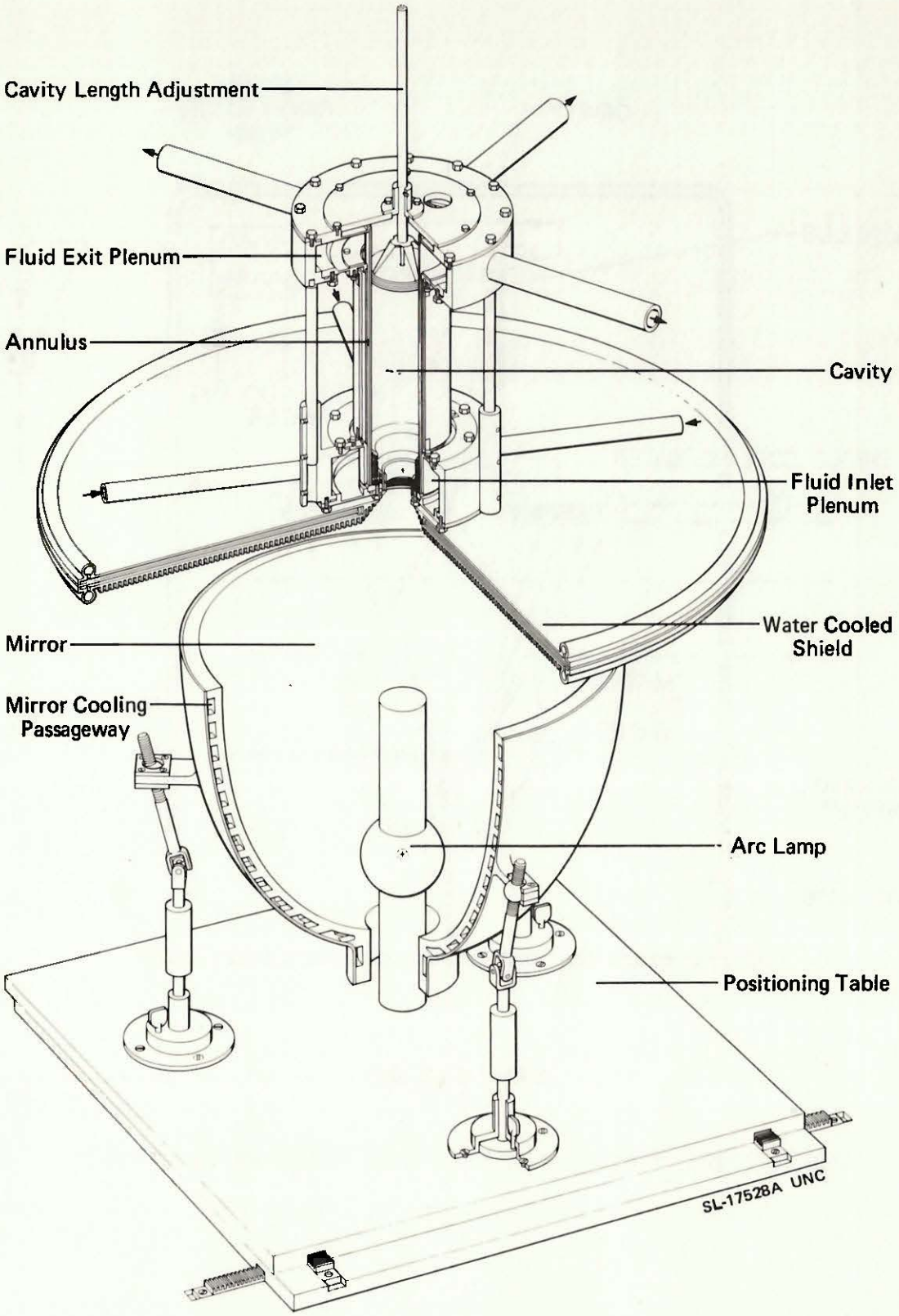

Figure 4-12. Bench-Top Model of Solar Cavity

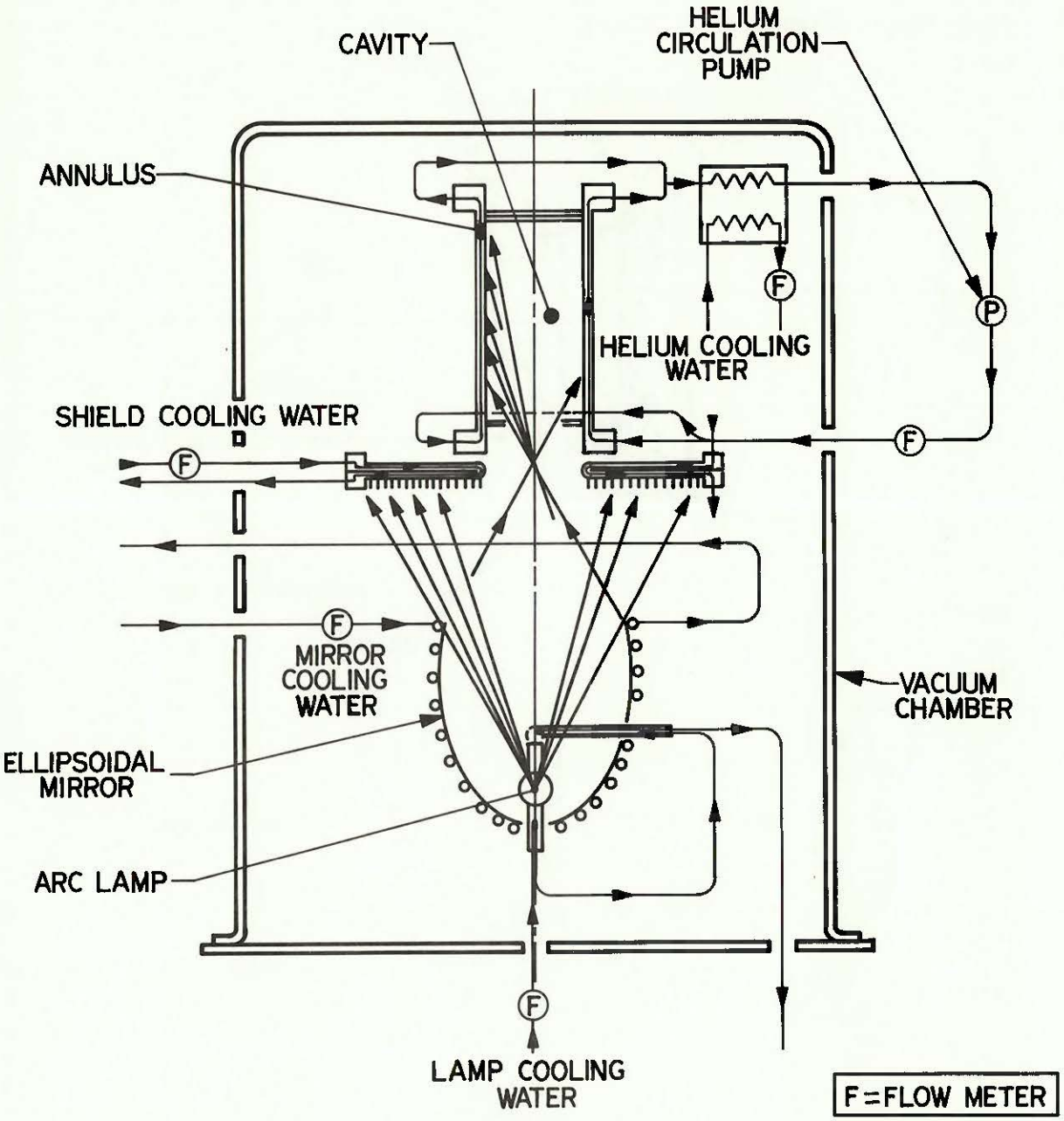

Figure 4-13. Schematic of Bench-Top Model of Solar Cavity

4.4 Direct Absorption of Solar Energy in a Circulating Fluid

One version of the proposed point focus collector system involves absorption of the concentrated solar energy directly in an optically dense heat transfer fluid. This approach avoids difficulties associated with heat rate limitations on conduction through an absorbing wall into a fluid and the corresponding drops in temperature which affect system efficiency.

A possible heat transfer fluid for this application is a mixture of KNO_3, $NaNO_3$, and $NaNO_2$ marketed by DuPont under the name Hitec. This material melts (when anhydrous) at about 70°C and is stable in air up to about 425°C. The liquid itself is very pale yellow in color and is a poor absorber of visible light. Two possible approaches to make this liquid highly absorbing are: (1) dope the mixture with a colored solute, the result of which is an absorbing homogeneous solution; or (2) suspend a colored, insoluble substance in the Hitec liquid, in which case the absorbent properties of the medium would depend primarily on the particle size of the solid material and the degree to which it is dispersed throughout the liquid.

Experimental Results

Since it is desirable to operate the absorbing cavity without a window and in the presence of the atmosphere, if possible, the experimental apparatus took the simple form of a coiled resistance heater surrounding an open quartz tube of 2.0 cm O.D. The bottom of the tube was visible so that the optical behavior of the material could be observed. Approximately 12 g of Hitec containing 1 wt.% of dopant material was placed in the tube and the temperature was rapidly raised to 350°C. The following dopant materials were tried: $CrCl_3$, $MnCl \cdot 6H_2O$, $Co(NO_3)_2 \cdot 6H_2O$, $CoCl_2$, $CoSO_4$, $NiCl_2$, $NiSO_4$, and $CuCl_2$. In all cases the dopant material decomposed rapidly upon heating due to oxidation by atmospheric O_2. In the case of $CoCl_2$, a sample of the black precipitate was taken for X-ray analysis. It was observed that the Cr and Ni oxides settled to the bottom of the solution almost immediately, the Cu oxide remained in suspension for several minutes, and the Co oxide stayed suspended for over an hour.

Discussion

From the above results it is clear that the use of transition metal salts as dopants in fused salts will not be possible unless the process is done under a vacuum or in an atmosphere of inert gas (i.e., nitrogen). Studies by several workers [1, 2, 3] have shown the stability of such dopants in fused alkali nitrates up to temperatures of several hundred degrees C.

In the event that such a procedure is considered for development, the sensitivity of these solutions to residual amounts of O_2 (and other oxidizing agents) in the system will have to be assessed. Also the question of long-term photochemical stability of these materials must be addressed; because radiant flux density will be very high in some regions of the cavity, otherwise imperceptible photo decomposition reactions could become important.

If homogeneous solutions prove to be unsuitable absorbers, then the use of dispersed solids in the Hitec liquid can be considered. From these preliminary results it appears that decomposition of a metal chloride might be an excellent procedure for the introduction of a finely divided metal oxide throughout the liquid phase. In the case of CuO and Co_2O_3, the oxides are black and finely dispersed, thus yielding a highly absorbing medium.

Possible difficulties in using a dispersed solid are: (1) particle nucleation, (2) precipitation on the system walls, and (3) actual particle size growth through continuous recrystallization in the hot medium. Constant agitation in a dynamic system may be sufficient to solve the first two problems. Prevention of crystal growth may be attacked in two ways:

1. A suitably refractory oxide may be chosen such that the growth rate is insignificant. CuO seems a good candidate for this approach as its decomposition temperature of 1026°C is considerably higher than either that of Co_2O_3 (895°C) or the maximum anticipated Hitec temperature of 540°C.

2. An oxide may be chosen which undergoes a reversible reaction to a lower oxidation state within the temperature regime of the system. Continuous formation and decomposition of the two oxides could result in a very fine suspension of the solid material which would be regenerated daily. The following reactions illustrate this approach:

$$2CrO_2 \xrightarrow{300°C} Cr_2O_3 + \frac{1}{2}O_2$$

$$2MnO_2 \xrightarrow{535°C} Mn_2O_3 + \frac{1}{2}O_2$$

$$Ni_2O_3 \xrightarrow{600°C} 2NiO + \frac{1}{2}O_2$$

The reversibility of such reactions and their rates in fused salts at ~400°C must be established in future work.

REFERENCES

1. B. R. Sundheim and J. Greenberg, Rev. Sci. Instru., 27 (9), 703 (1956).

2. B. J. Brough and D. H. Kerridge, J. Chem. and Eng. Data, 11 (2), 260 (1966).

3. S. V. Volkov and N. I. Buryak, Russ. J. Inorg. Chem., 17 (1), 93 (1972).

4.5 Sandia Laboratories Radiant Heat Facility

The Sandia Radiant Heat Facility (Figure 4-14) is expected to be a valuable tool in the development of various types of absorbers for the central receiver system. It is part of a high-temperature testing complex located in the Sandia Laboratories Remote Test Area. The facility was built to provide laboratory simulation of high-temperature environments on large assemblies. A wide range of thermal environments has been simulated: from high-level, short-duration programs simulating the thermal energy from a nuclear burst or launch pad abort fire; to intermediate-level and long-duration programs simulating transportation accident fires; to low-level, intermediate-duration programs simulating aerodynamic heating.

The facility has eight channels of programmable, three-phase power controllers. Long-duration programs can be operated at a sustained level of 5 MW. Peak power level is approximately 20 MW.

Thermal input is produced with either high-power lamps or graphite-resistance heaters. The radiant spectrum produced by these heat sources is shifted towards the infrared as compared to the solar spectrum. This spectral shift should produce no problems unless highly selective surface coatings are used on test hardware.

Test items up to 17-ft high can be accommodated inside the facility; an outdoor test pad is also available. The facility is located in a remote test area with widely separated facilities; thus adequate safety precautions can be made for testing hazardous systems such as high-pressure steam generators.

Test data acquisition and reduction is accomplished on a dedicated, computerized data system located in the test complex.

Additional services which are available in the complex are: (1) a closed-loop cooling water system with a 300,000-gallon storage tank, (2) a 4,200,000 Btu/hr cooling tower, (3) a boiler capable of producing up to 50,000 lb/hr of steam at 175 psig, and (4) high-pressure, large-volume nitrogen, oxygen, and argon gas storage tanks.

Testing programs which could be handled include:

1. Evaluation of sections of full-scale items at rated heat flux levels.

2. Evaluation of scale models.

3. Evaluation of engineering design problems such as flow stability and thermal stress effects.

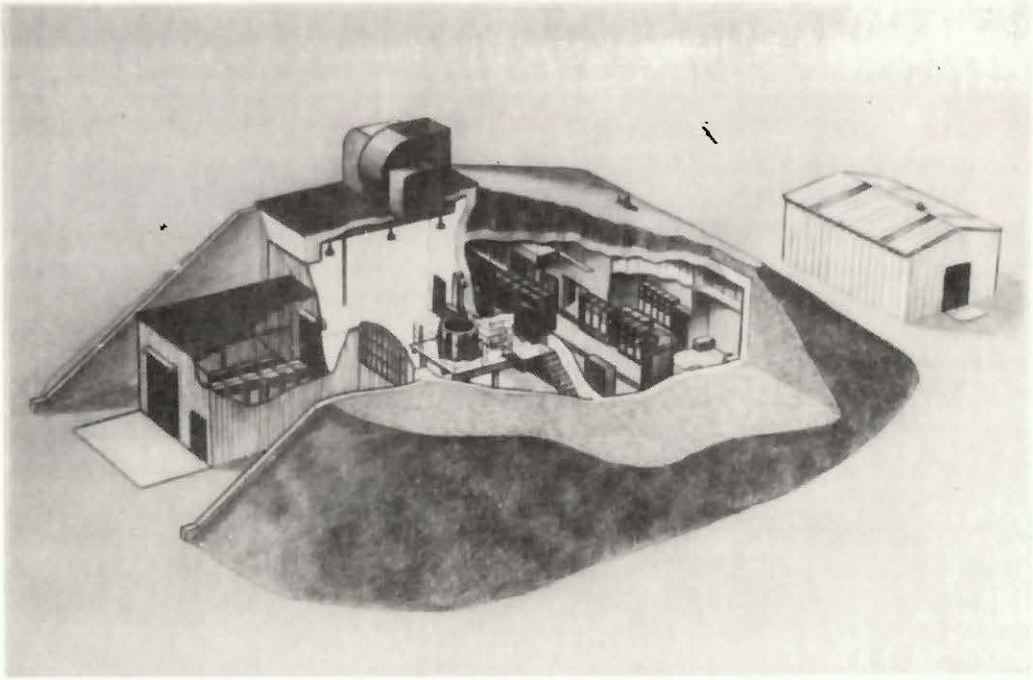

Figure 4-14. Existing Sandia Laboratories Radiant Heat Facility

5.0 Tower Design (Bechtel Corporation Study for Sandia Laboratories, June 1974)

A preliminary structural study was conducted to produce a technically feasible design of the central collector tower in order to make an order-of-magnitude cost estimation.

Tower Design

The tower was tentatively designed in accordance with the following guidelines set by Sandia Laboratories:

- Tower site to be in Albuquerque, New Mexico
- Tower heights to be 200, 300, and 400 meters
- Basic design to be a steel guyed tower
- Maximum allowable sway at the supporting point of the cavity on the top of the tower to be less than 10 percent of the cavity aperture diameter at a wind speed of 25 mph at 30 feet above ground
- Tower design to provide adequate support for the cavity and its associated energy collection and transport equipment

In this preliminary study, standard structural engineering methods were used for the design of the tower. It must be emphasized that the design is primarily for an order-of-magnitude cost estimation only, and structural specifications are to be treated as tentative. The books, articles, and codes listed in References 1 through 6 were used for the study.

The principal loads on the tower are the gravity loads (self weight of the structure and the weight of the cavity with its heat transport facilities), and the wind forces. A square trussed tower was deemed suitable in view of the rigidity required and for the support of a heavy cavity. It was chosen to be the basic design for all three tower heights. This tower is depicted in Figure 5-1; a typical cross section of the tower is shown in Figure 5-2.

The main body is constructed with light structure wide frame steel members with lateral and diagonal bracing of double angles. Again, this design was chosen primarily for cost estimation purposes. Further studies should consider other alternative designs more aerodynamically shaped to minimize wind loading. No effort was made to minimize the self weight of the structure in this study, and therefore the cost of construction estimated for the tower is probably on the conservative side. Although the cavity weight was specified by the Sandia Laboratories, there were reasons to believe that the solar energy conversion efficiency at the cavity would be improved if its weight were allowed to increase to accommodate a more optimum design. In view of this, allowances were made in the structural design of the tower to support a cavity that is up to four times the cavity weight specified.

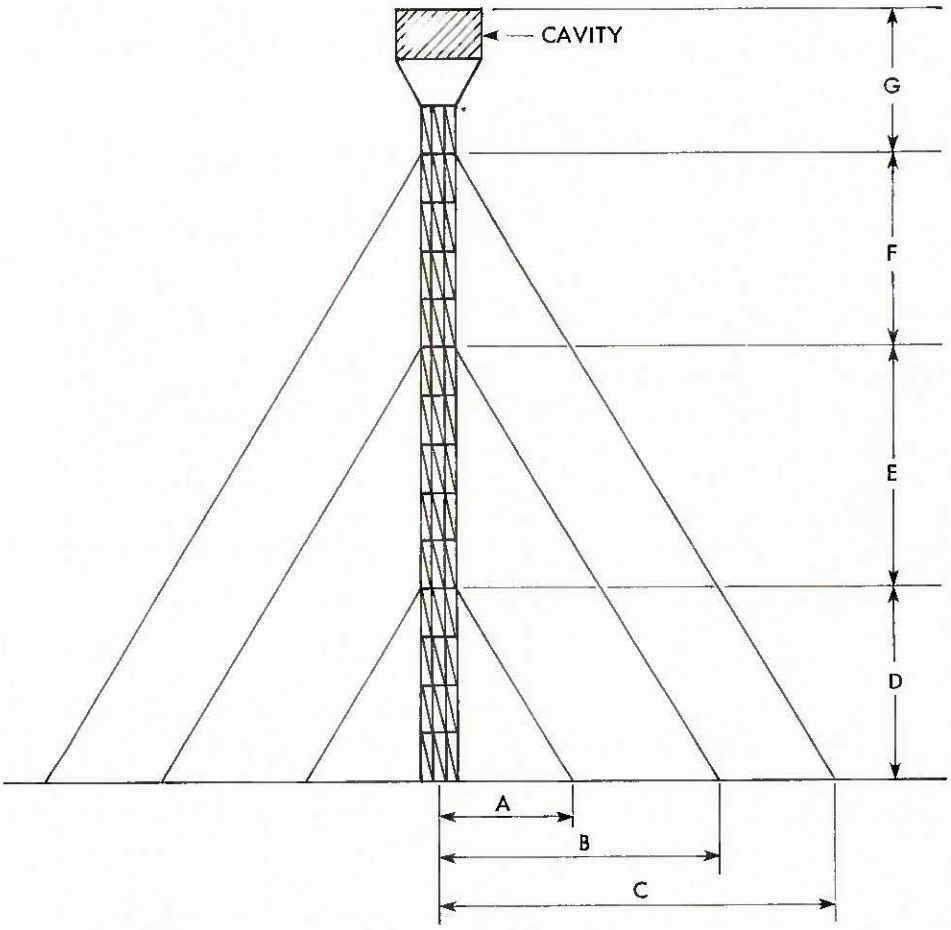

Figure 5-1. Tentative Design of Central Collector Tower

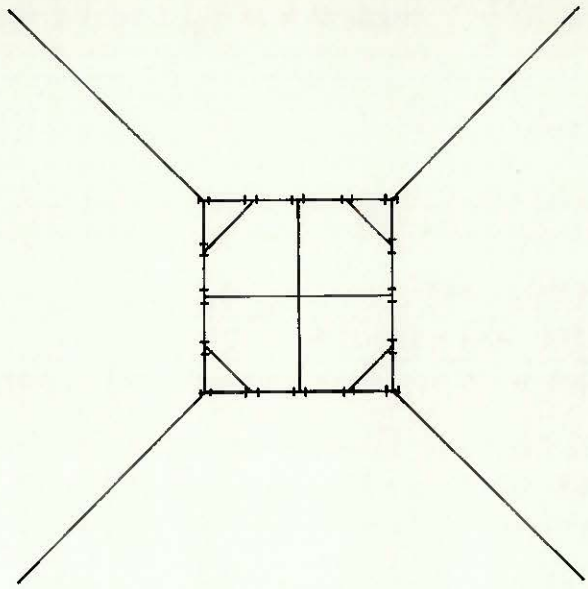

Figure 5-2. Horizontal Cross Section Showing Tower and Guys

The design criterion for the survival of the tower was based on short durations up to two seconds of wind speeds up to 80 mph at 30 feet above ground. Since Albuquerque is in a mild seismic zone, the structural design based on this wind speed criterion is deemed adequate to withstand seismic disturbances.

As a first order of approximation, the wind loading on the structure was assumed to be constant between successive guy levels. The dynamic pressure of a horizontal wind at height z is q_z and is given[2] by the formula

$$q_z = \frac{1}{2} d V_z^2 \tag{1}$$

where d denotes the density of air and V_z is determined by

$$V_z = V_{30}\left(\frac{z}{30}\right)^p \tag{2}$$

where V_{30} = wind speed at 30 ft. above ground level

$p = 0.3$ (assumed)

This dynamic pressure q_z, when multiplied by the drag coefficient C_D, gives the horizontal pressure p_h; and when multiplied by the lift coefficient C_L, gives the vertical pressure p_v on the tower. Since it is the horizontal pressure which causes the sway of the tower, it is appropriate to discuss the determination of the drag coefficient at this point.

Cohen and Perrin[3, 4] suggest that C_D may be approximated by the formula

$$C_D = 4-5f \tag{3}$$

where

$$f = \text{solidity ratio}$$

$$= \frac{\text{solid area normal to wind}}{\text{total solid and open area normal to wind}}$$

Although the tower is an open structure, facilities such as the heat transport pipes inside the tower must be included in the calculation of f, which is a measure of the obstructions in the path of air flow. Within the range of 0.0 to 0.4 of f that is generally applied to structures similar to the one under consideration, the value of 0.3 was arbitrarily chosen for this study.

The tower is of a lattice type, but for a first order of approximation, it was treated as a beam on rigid supports. Figure 5-1 shows the tentative design of the tower with three levels of guys. At each level, there are four guys, each extending at right angles to its adjacent ones from the four corners of the tower to their ground anchors as shown in Figure 5-2. The portion which cantilevers above the top guy support was designed as a free-standing portion. The positioning of the guys for the three towers are shown in Table 5-1 with reference to Figure 5-1. Both the number of guy levels and their positioning are tentative in this design. Further studies should investigate the optimum guy levels, and the possibility of a common point for ground level anchoring for guys from all levels from each side of the tower. This would give continuous ground clearance for the traveling sprinkler used to wash the mirrors.

The sizes and initial tensions of guys were so adjusted that the wind deflection of the tower at each guy level is expected to be proportional to the distance above the ground. The sway of the tower was calculated on this basis. To provide adequate tension in the guys, galvanized steel bridge rope with wire core was assumed for the guys. The preliminary design was found to satisfy the prescribed sway limitation, which is ten percent of the aperture diameter in all directions from the center. Further studies to finalize the design of the tower should employ wind tunnel testings or data derived from this technique to ascertain the sway limit.

The cavity support is shown in Figure 5-3. It is a circular beam on top of a four-legged support. The beam is constructed of steel plates which are welded together to form a square cross section of the beam. The inclined support legs for the circular beam are spaced so as to minimize the blocking of the incoming solar radiation.

The Foundation

The tower is founded on reinforced concrete mats supported by piles. This arrangement simulates the fixed-end design assumption. The guys are anchored to cylindrical concrete caissons on the ground.

TABLE 5-1. TOWER PARAMETERS*

Tower Height		200 m	300 m	400 m
Tower Cross Section		6.1m x 6.1m	9.2m x 9.2m	12.2m x 12.2m
Guy Locations**	A	358m	240m	107m
	B	220m	320m	404m
	C	200m	300m	384m
	D	65m	107m	128m
	E	65m	107m	128m
	F	57.8m	71.4m	128m
Free-Standing Portion	G	9.15m	15.25m	16m
Cavity: Weight		27,000 kg	41,000 kg	86,000 kg
Diameter		16m	19m	30m
Foundation: Size		12.2m x 12.2m	15.2m x 15.2m	18.3m x 18.3m
Thickness		1.07m	1.1m	1.1m
Guy Anchorage Caisson:				
Diameter		2.74m	2.74m	2.74m
Length		4.90m	4.90m	4.90m

*Reference Figure 5-1.

**Note that the guy wires cross in some cases.

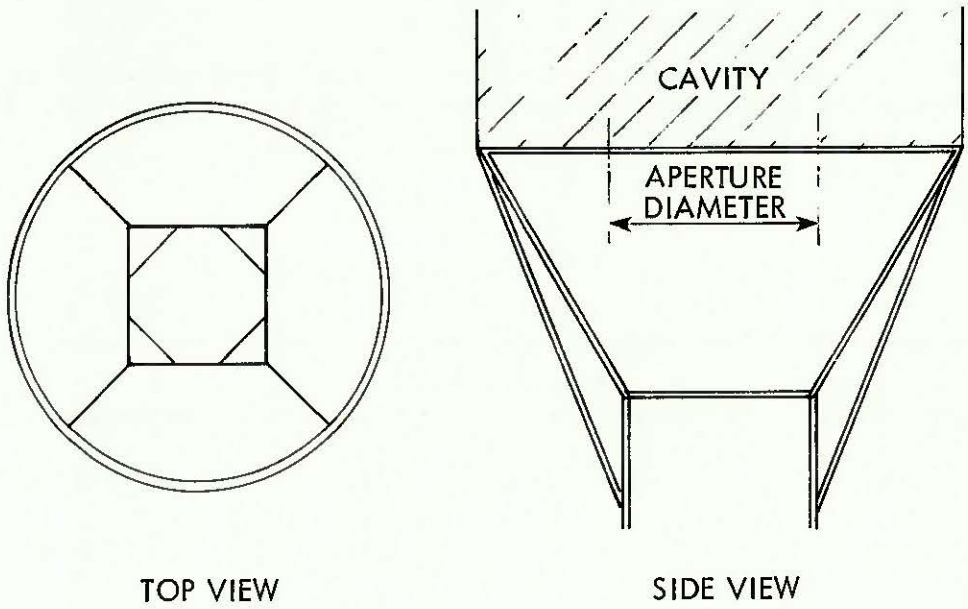

Figure 5-3. Cavity Support

REFERENCES

1. Manual of Steel Construction, AISC, 7th Edition, 1970.

2. Wind Forces on Structures, Final Report, Paper No. 3269, ASCE.

3. Cohen, E. and Perrin, H., Design of Multi-Level Guyed Towers: Wind Loading, Proc. Paper No. 1355, ASCE.

4. Cohen, E. and Perrin, H., Design of Multi-Level Guyed Towers: Structural Analysis, Proc. Paper No. 1356, ASCE

5. Hall, F. H., Stability Analysis of Multi-Level Guyed Towers, J. Struct. Div. Proc., ASCE Paper No. 3091.

6. Sachs, Peter, Wind Forces in Engineering, Pergamon Press, 1972, Chapter 8.

6.0 Mirror Field

6.1 Mirrors, Guidance, and Mounts

The primary requirement constraining mirror design is low cost per square meter of installed mirror. Because proposed mirror fields cover many thousands of square meters, the cost of the mirror field will probably be a significant fraction of the total system cost. The efficiency and accuracy by which solar radiation can be redirected to the point of absorption is also of primary importance as these factors directly influence the overall efficiency of the system.

Additional prerequisites that must be considered in the design of mirror modules include (1) the stability of reflective surfaces due to exposure to the environment; (2) the stability of mirror shape during normal operation; (3) the adequacy of the mount/mirror design to withstand adverse weather conditions; (4) minimal requirements for cleaning and maintenance of mirror surfaces; (5) minimal maintenance for guidance system; (6) minimum energy needed for mount tracking; and (7) adequate lifetime.

The design of a mirror module can be separated into three elements: the mirror, the mount, and the guidance control.

The Mirror

Reflective Surface

Mirrors must possess high reflectivity to solar radiation (wavelengths of 0.2 to 3.0 micrometers). Highly reflective surfaces can be made by using a smooth metallic surface. This process relies on the high extinction coefficient of the base material. Typical values for the total normal reflectance of solar energy at sea level are shown in Table 6-1 for various freshly vapor-deposited metallic coatings.

TABLE 6-1. TOTAL NORMAL SOLAR REFLECTANCE OF MIRROR COATINGS

Material	Reflectivity
Silver	97.9
Aluminum	91.9
Gold	85.3
Copper	86.9
Rhodium	81.9
Platinum	76.7

The reflectance of a surface depends upon the angle of incidence, polarization of the light, and the optical constants of the material; namely, the refractive index and the absorption index or extinction coefficient. The optical properties vary with the frequency of incoming radiation. For most metals with a high electrical conductivity, the extinction coefficient is high (especially in the infrared region) due to the high concentration of conducting electrons. These metals therefore produce the most reflective surfaces. Since the highest possible reflectivities are required, it is evident that only silver or aluminum can be chosen for the reflective surface. Both of these materials are available at reasonable costs and are in adequate supply.

Another important parameter is the quality of the reflective materials' surface finish. High quality surfaces are made basically in two ways: by polishing the metallic surface, or by depositing the reflective material onto a smooth substrate. Many high quality mirrors are fabricated by mechanically polishing a surface. This process may or may not be followed by a chemical treatment (etching or electropolishing). These techniques, while producing high quality surfaces, are not amenable to high production rates. A technique which appears to produce a satisfactory surface and which would be amenable to mass production is the Alcoa Alzak process. In this process, special aluminum alloys are chemically or electrochemically brightened and subsequently anodically treated to provide a protective coating. Material produced by this process would cost approximately $10.00 per square meter and have a reflectivity of about 83 percent.

Most mirrors available today are produced by depositing reflective material onto a smooth substrate. The substrate is usually glass or plastic although any smooth surface can be used. Either first surface or second surface mirrors can be fabricated in this manner. On a first surface mirror,

light is reflected directly off the metallic surface while on a second surface mirror light must travel through a transparent material before it is reflected. First surface mirrors have the disadvantage that the reflective surface is exposed to the environment and therefore if the coating is an active element such as silver, it will tend to tarnish quickly. Thin transparent coatings (such as silicon monoxide) have been used to provide some protection for these surfaces. Second surface mirrors, produced by depositing either silver or aluminum onto the back of a transparent substrate, provide protection for the reflective surface. Glass and transparent plastic sheets or film are used as substrate materials.

Glass, Plastic Films

Glass is an excellent substrate material because its optical properties are relatively stable. It can be made with very smooth surfaces and can readily be cleaned with no damage to the surface. Glass does have its disadvantages, however, as it is not a structural material (unless loaded entirely in compression) and is fragile and difficult to handle in large sizes. Also, if used in any appreciable thickness, absorption in the glass greatly reduces the efficiency of the reflector, especially for reflections at low angles of incidence to the mirror surface. As an example, if a 6.35 mm (0.25 inch) thick sheet of low iron water white glass (extinction coefficient, $K = 0.0042\ mm^{-1}$) is used as a substrate, about five percent of the energy normal to the surface would be absorbed in the glass, while seven percent of energy at a 45° incidence angle would be absorbed. For a more common type of glass ($K = 0.0165\ mm^{-1}$), the absorption in each case would be over three times as great. This problem can be reduced if the reflective surface is laminated near the front surface of the glass in a process similar to the production of automobile windshields.

Although plastics are not as abrasion resistant as glass, they can be produced with the same optical clarity and are not as fragile as glass. Plastics can be obtained in thin films which can reduce costs. The weatherability of plastics is not well established; however, an acrylic sheet was exposed to the Albuquerque, New Mexico, environment for 18 years and showed only a ten-percent loss in transmissivity. After lightly polishing the surfaces, the transmisssivity was down only a few percent from reported original values.

Mirrors of very high reflectivity can be produced on thin plastic films. For example, Sheldahl has reported a silvered teflon surface with a reflectivity of 0.95. Commercially available mirrors of aluminized polyester tested at Sandia Laboratories show a reflectivity of 0.93. Possible candidates for plastic films include Teflon, weatherable Mylar (polyester), Tedlar (pvf), and Korad (acrylic). Screening of these films will include

measurement of their weather resistance, including degradation due to exposure to solar radiation; ability to provide smooth surfaces; and ability to bond to the metallic reflector material.

Environmental exposure tests of candidate reflector materials are underway in Florida, Arizona, and Minnesota under the auspices of the University of Minnesota and Honeywell. Both teflon and acrylic second surface mirrors are among samples being tested. Although the test has been in progress for only slightly more than a year, visual degradation of some samples is apparent. However, in many cases, reflectivities are unaffected and the results thus far are not conclusive.

Mirror Surface Contour

The surface contour of a mirror is an important factor in determining its cost. Flat mirrors can be made relatively inexpensively whereas curved shapes presently are considered to be more costly. To determine the influence of mirror shape on the requirements for mirror pointing accuracy and cavity aperture size, a ray tracing program has been devised. The program determines the position of the sun for any day of the year, latitude, and time of day. It then can determine the reflected image of the outer edge of any mirror in the field on a horizontal aperture at any height. Presently, the program does not include mirror orientation errors, mirror surface errors, the dispersion caused by the finite size of the sun, or the influence of a terminal concentrator about the cavity aperture, although these factors can be added.

Figure 6-1 shows typical output of the ray-tracing program. In this example a flat mirror and a spherical mirror, both 5 meters in diameter are compared. The focal length of the spherical mirror is 424.2 m (sharp focus on aperture). As illustrated, the image from each mirror differs for each position and time of day. The image from the spherical mirror never becomes completely focused since the incoming radiation is never parallel to the mirror normal. This example shows that the curved surface produces a more compact image, which allows smaller cavity apertures or permits greater tracking errors and mirror aberations. The example demonstrates that a slight dishing would be beneficial in spite of the off-axis aberration.

This program also shows that if the curvature in two axes of the mirror (one axis in the plane of the sun, mirror, and cavity) can be independently changed as a function of mirror orientation, the image on the aperture can be maintained in comparatively sharp focus.

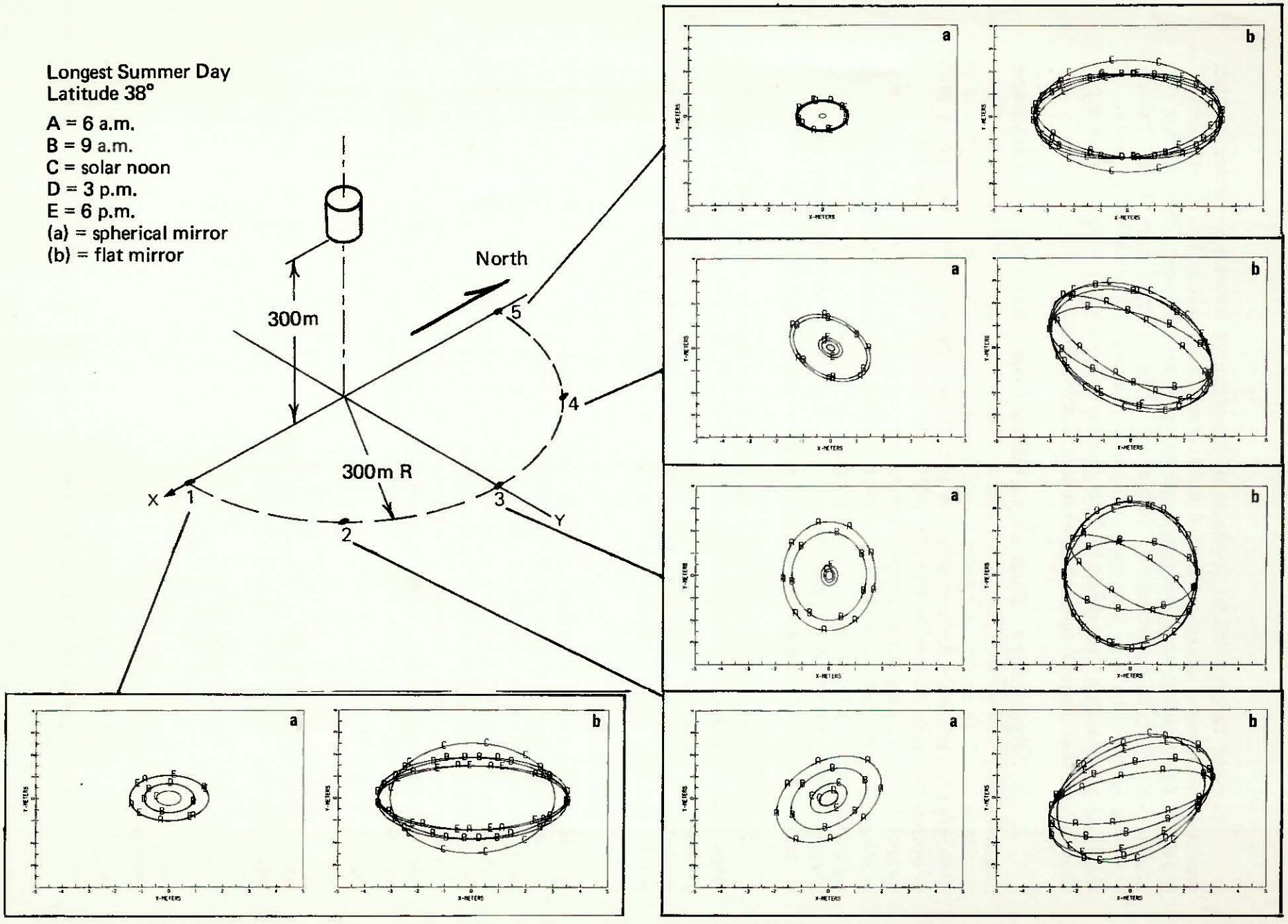

Figure 6-1. Calculated Image of Dished and Flat Mirrors on Cavity Aperture

Various techniques to produce an inexpensive focusing mirror of high quality were investigated. Since the mirrors under study had f-numbers (ratio of focal length to aperture), usually greater than six, the mirror shape can either be parabolic or spherical. These processes were screened for ease of manufacture and amenability to mass production techniques. On this basis, grinding/polishing and electroforming appear to be less desirable. Processes that appear to have merit are listed below.

Cast Polyurethane--Cast polyurethane foam offers several advantages. Lightweight, low-cost structures can be fabricated using mass production techniques. The major expense would be high precision molds which can be amortized over many pieceparts. A prototype mirror fabricated using polyurethane foam is shown in Figure 6-2a. By controlling composition, reaction rates, and zone temperatures during the casting operation, it is believed a part with acceptable surface finish can be made. By casting against a polished surface, a smooth surface was generated on the foam. Further study is needed to determine the adequacy of this surface as a mirror substrate although visually it appears quite good.

Three methods of forming a reflective surface on foam have been tried with some success: (1) vapor depositing directly onto the front surface with a suitable overcoat, (2) bonding (or possibly electrostatically holding) a thin metallized film to a polyurethane surface, and (3) casting foam directly onto a thin metallized film stretched over the mirror face surface within the mold.

With proper surface protection the polyurethane would have sufficient lifetime. The major problem identified at this time is distortion produced by thermal expansion due to nonuniform temperatures within the mirror structure. Distortion of this type is a problem in any mirror construction, but is particularly important with polyurethane because it has a high coefficient of thermal expansion. The magnitude of this problem is presently under investigation. Possible design solutions might include (1) a segmented construction, (2) reinforcement, and (3) tailoring the absorptance of the surfaces of the mirror structure to produce a more uniform temperature distribution.

Centrifugal Casting--By spinning a material about a vertical axis, a paraboloid can be formed. The focal length is related to the speed of rotation:

$$f = 4.9 \frac{g}{\pi^2 n^2}$$

where f is the focal length

g is the gravitational constant

n is the angular velocity in radians per second

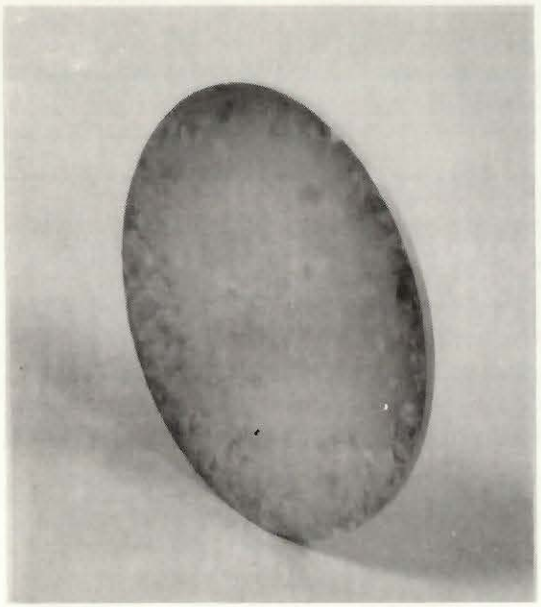

a) Molded Polyurethane (with tarnished unprotected silver deposition)

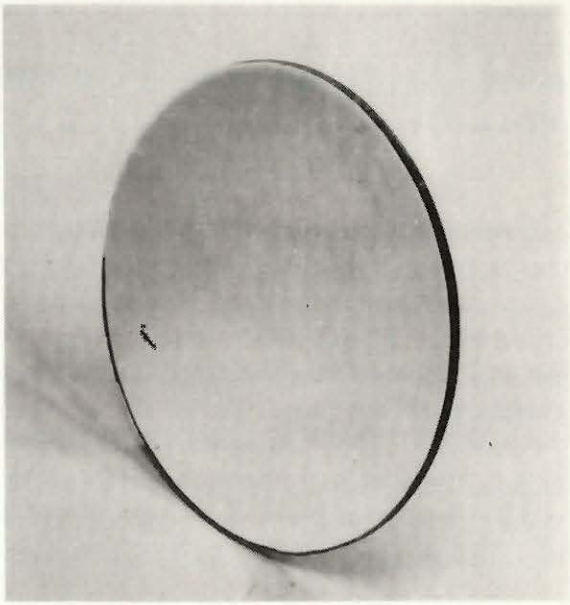

b) Centrifugally Cast Epoxy

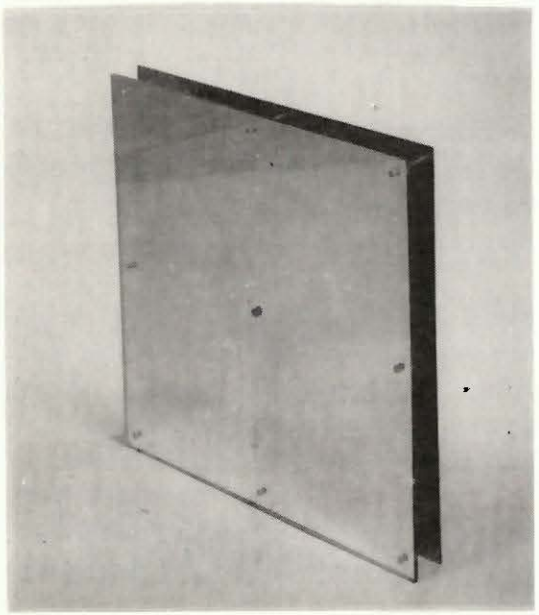

c) Flexure of Flat Plate (point loading)

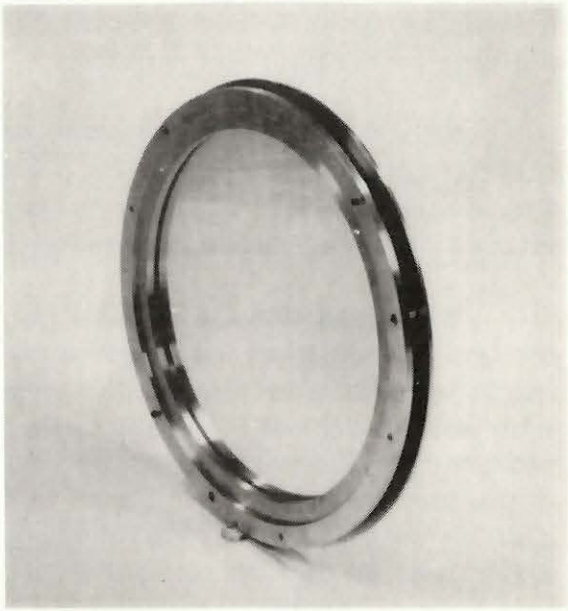

d) Flexure of Flat Plate (uniform edge moment)

Figure 6-2. Prototype Mirrors

Although this phenomenon has been known for many years, it was not successfully exploited to produce mirror surfaces until the use of epoxy became widespread. Epoxy solidifies uniformly and yields a smooth glass-like surface.

Figure 6-2b shows a 30-cm prototype produced at Sandia. It was found that some processing steps require careful control. The epoxy must be outgassed prior to the casting operation, and the rotation must be vibration free and done in a clean atmosphere. The focal length of the surface generated is smaller than predicted by the equation above due to shrinkage of the epoxy; however, this shrinkage is believed to be controllable. The reflective surface can be formed either by vapor deposition as shown on the prototype or by attaching a thin metallized plastic film to the surface. In actual practice, the rough shape of the mirror would be formed by some other process such as casting or stamping and only a thin coating of epoxy would be used to produce the final mirror contour.

Although this process produces excellent quality surfaces on small prototypes, additional work is required to address scale-up problems.

Flexure of Flat Plates--Since high-quality flat mirrors can be produced inexpensively and since mirrors with long focal length require only a small curvature, it appeared worthwhile to attempt to form mirrors to the desired contour by bending flat plates.

Several point loading schemes were tried, including the nine-point method shown in Figure 6-2c. All proved to be difficult to adjust (although this could probably be automated) and produced images of lower quality (see Figure 6-4) than those generated by other techniques.

Theoretically, spherical shaped mirrors can be formed from flat plates by applying uniform edge moments to the edges of the plate (for elastic deformations). This technique has been tried on both square and circular plates with some success. Figure 6-2d shows the circular plate with the edge moment produced by clamping two concentric rings of slightly different diameters on the outer edge of the mirror. The edge moment loading might also be used if slightly different curvatures are required in two orthogonal directions on the mirror surface. If a variable contour mirror is needed, this type of loading could also be used.

Differential Pressure on Thin Films--If a perfectly elastic membrane is stretched over a circular ring and subjected to nonequal pressures on each face, the membrane will form a paraboloid. The focal length would be directly proportional to the tension in the membrane and inversely proportional to the pressure difference.

Although this technique has been used with metallized films to produce solar mirrors, it may not be feasible for the point focus system unless durable films and reliable methods to hold the pressure differential can be developed.

All schemes that rely on loading either glass or plastic to form the desired shape may require periodic adjustment because of the creep characteristics of these materials.

Additional Alternatives--Other possibilities exist if shaped mirrors are required. Mirrors have been built up on polished male forms successfully, beginning with a layer of epoxy to form the mirror substrate and subsequently adding structural materials to give the mirror stiffness. Alternately, one might be able to form glass or plastic sheets to the desired shape by heating them in a mold of the correct shape.

In large solar furnaces, curved shapes are sometimes approximated by many flat sections appropriately oriented. This multifaceted concept would probably be used in any design using glass, including flat mirrors, to simplify handling problems and minimize breakage.

Mirror Surface Evaluation

Some of the prototype mirrors have been contour inspected to determine the adequacy of their shapes. Another technique, although not as quantitative, gives an easier overall evaluation of the surface shape. Figure 6-3 schematically represents the test setup. A laser is used to project a grid pattern on the mirror being tested and the reflected image is photographed. Figures 6-4 and 6-5 show images produced by the point loading technique and the spin casting process.

Mount Design

Design Requirements

The mirror mount must be able to accurately position the mirror surface to redirect the incident insolation to the cavity. It must also survive adverse environments and be designed for minimum cost. The following are important design considerations.

Tracking Accuracy--For the baseline design the cavity aperture is sized to accommodate a total mirror and tracking error of up to ±10 minutes. The guidance system developed can control the mount orientation within ±2 minutes and thus the allowable mirror inaccuracy is ±8 minutes.

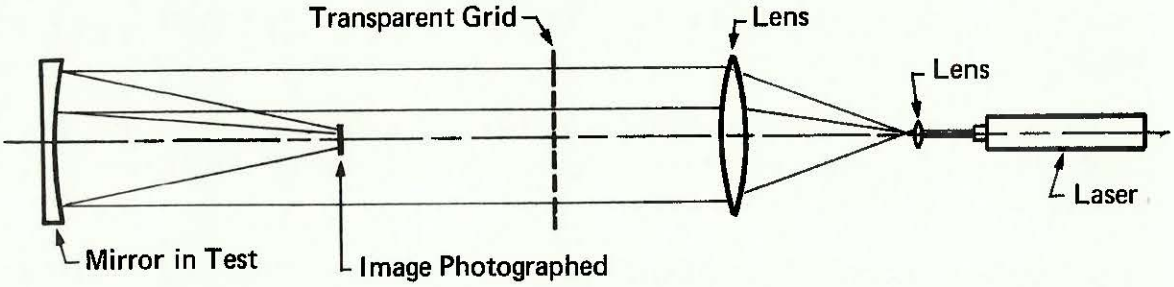

Figure 6-3. Mirror Test Setup

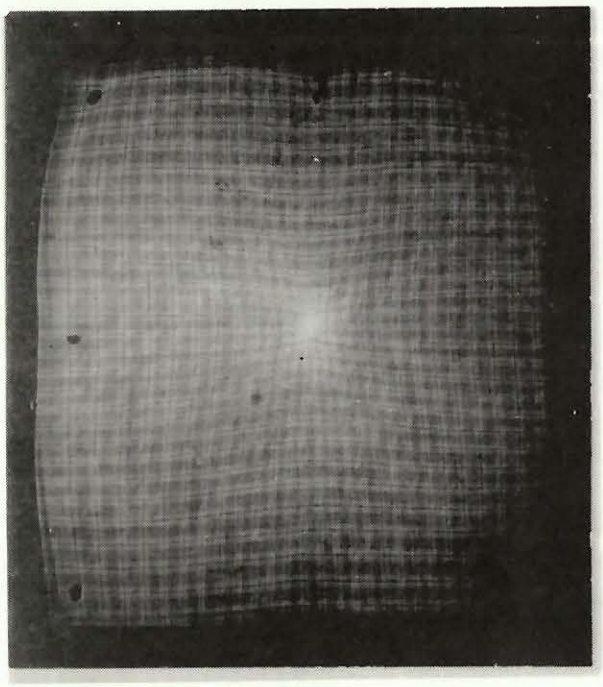

Figure 6-4. Image of Point-Loaded Mirror

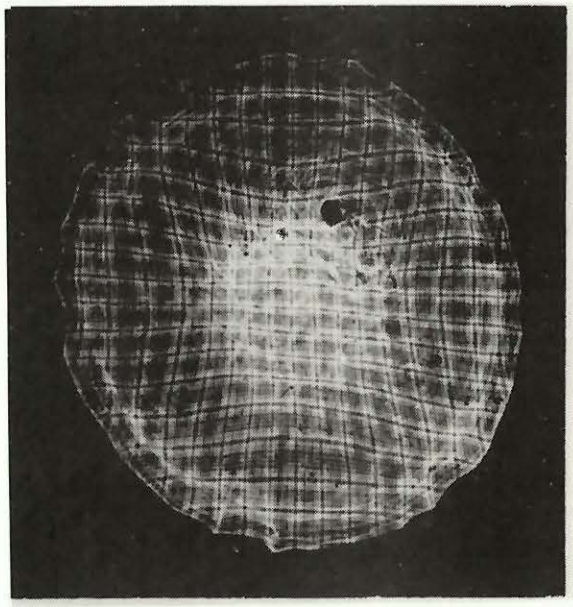

Figure 6-5. Image of Centrifugally Cast Epoxy Mirror

Wind Loading--The mount should maintain tracking accuracy with wind loads up to 35 mph. Minimum damage should be sustained from winds up to 75 mph. The low velocity aerodynamics of large, nonstreamlined mirror structures must be analyzed. The protection of mirrors by adjacent mirrors may prove valuable and possibly mirrors on the outer edges of the field will be designed with more structural rigidity to protect internal mirrors.

Mount Axes of Rotation--There are many possible orientations of mirror axes, and each configuration has a direct influence on the mount design. Since each mirror in the field would have a unique motion, the problem of defining the mirror displacements is more complex than one might suspect. Computations have been made to determine the movement required for five basic configurations. Results of these calculations are shown in Table 6-2. The maximum angular excursions were calculated throughout a year for the most widely ranging mirror in a field with a 63° rim angle, and assuming that the mirror tracks from sunrise to sunset. The actual angular excursions will be less since little energy is collected during early morning and late evening hours. Additionally, it may be desirable to rapidly reorient the mirrors for emergency shutdown, and to orient the mirrors away from adverse weather in a secured position during high winds.

Low Cost--To produce a low-cost design, inexpensive materials must be used and the design must be amenable to mass production. Candidate materials would be concrete (reinforced, prestressed, etc.), steel, and foam materials. The mounts should have at least a 20-year life and require little or no maintenance.

Conceptual Mount Designs--Although little detailed design has been done on specific mount designs to date, concepts are presented to show possible configurations.

Figure 6-6a illustrates a pedestal mount utilizing hydraulic actuators. The pedestal would be a hollow cone of prestressed concrete. A gimbled mount would allow the mirror substructure to pivot in any direction atop the pedestal, but would restrain any tendency of the mirror to twist. Special off-axis universal joints on the upper ends of the hydraulic actuators would allow the mirror to rotate greater than 120° in each axis. The hydraulic actuators support the mirror structure away from the axis of rotation. This allows the mirror to be held more firmly and results in more accurate positioning. A typical hydraulic servo system requires a pump, an accumulator, a servo valve along with the cylinder and actuator. A large number of mirrors could operate from one pump, making the cost of the pump insignificant on a per mirror basis.

Another pedestal mount is shown in Figure 6-6b. The pedestal is constructed as described above, but with this design, one axis of rotation

TABLE 6-2. MIRROR COORDINATE AXES

	MOUNT AXIS		MIRROR AXIS					
	Orientation	Max. Angular Excursion	Orientation	Max. Angular Excursion	Individual Sun Tracker (1)	In-Line Sensor	Other Advantages	Other Disadvantages
I	In line with cavity	236°	Perpendicular to mount axis	73°	Yes	Yes (2)		Each mount aligned differently
II	Vertical	217°	Perpendicular to mount axis	74°	No	Yes		
III	Horizontal, North-South	141°	Perpendicular to mount axis	91°	No	Yes (3)	Mirrors in rows	
IV	Horizontal, perpendicular to radius from tower	107°	Perpendicular to mount axis	110°	No	Yes		
V	Horizontal, East-West	93°	Perpendicular to mount axis	110°	No	Yes (3)	Mirrors in rows	

Notes:
1. Yes considered for sun tracker only when it works with simple gearing.
2. In-line sensor works only if it is mounted such that it rotates with mount axis.
3. Some sensitivity and accuracy may be lost because sensing axis are not orthogonal in most cases.

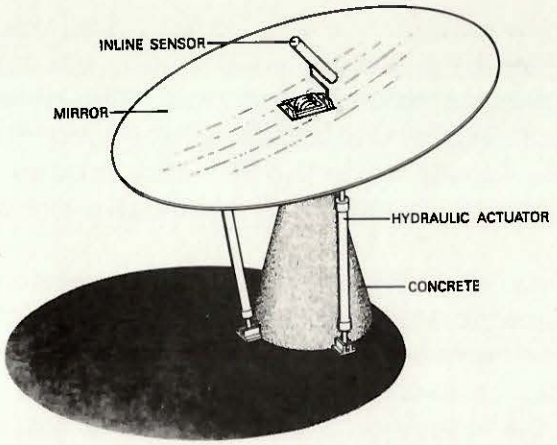

a.

b.

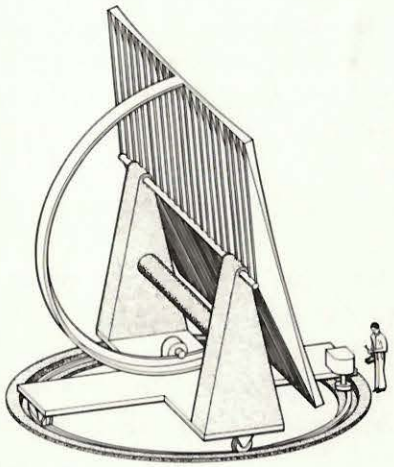

c.

Figure 6-6. Mirror Mount Designs

can be pointed toward the cavity. In this orientation, the two axes of rotation can be controlled by a simple suntracking sensor, although a more precise actuation mechanism will be required. The drive system for this concept would consist of an electric motor with appropriate gearing for the axis pointing toward the cavity while the tilt axis motion could be generated by electrically-driven linear actuators or hydraulic actuators.

A third concept shown in Figure 6-6c has a vertical and a horizontal axis of rotation. The major structures would be made of concrete. The mirror module would be mounted on a circular track on which the entire structure turns. Motion is induced about the horizontal axis by means of a fixed motorized drive that rides on a circular track attached to the back of the mirror surface. On both axes, the point where the driving force is applied is far from the axis of rotation thus providing excellent positional control.

The possibility of floating the entire mirror field on a large concrete slab in a few inches of water has been studied. The floating mirror field would rotate about the central tower, following the position of the sun. The advantage of this concept is that less total mirror motion would be required than shown on Table E-2 and the mount designs can be greatly simplified. Although controlled motion about two axes would still be required for almost all of the mirrors in the field, possibly this motion can be generated by properly designing linkages with a single drive system since the orientation of each mirror is only a function of position of the mirror in the field (which is constant) and the height of the sun above the horizon. Another advantage of this scheme is that shadowing of adjacent mirrors would be less and a greater density of mirrors should be possible. These advantages must be compared to the additional costs and restrictions imposed to judge the merits of this scheme.

In most of the concepts described, electric motors are utilized. Care must be taken to minimize the amount of power used to drive the mirrors. From the standpoint of simplicity, low maintenance, long life, and low cost, a brushless AC motor with a magnetic servo amplifier is ideal. However, peak loads required at start up and emergency defocusing would necessitate very heavy AC service connections. The possibility of a loss of power rendering the entire system unable to respond is also undesirable.

By adding batteries into the system for each of the mirrors and using AC power to trickle-charge the batteries, the size of the AC service can be significantly reduced. Brushless DC motors, either constant speed or stepper types, are available. These motors should have the same reliability and life expectancy as an AC motor and the servo amplifier should only be slightly more complex.

Guidance and Control

Closed-Loop vs. Opened-Loop

For accurate tracking of the mirrors, the advantages and disadvantages of a closed-loop control system using reflected beam in-line sensors was compared with an open-loop computer controlled system. The results of this preliminary study revealed that the open-loop system was not economically competitive with the closed-loop system.

The open-loop system, in which the mirrors' movements are predetermined and scheduled by computer, would require very rigid mounts that would have to be precisely aligned. Changes in the mount caused by thermal expansion or ground settling could not be tolerated. Even if these requirements could be met, a precise feedback system would most likely be required to determine the orientation of the mirrors with respect to the mount. This feedback measurement would require equipment costing more than the closed-loop system considered. The closed-loop guidance with a sensor in the reflected beam is a simple, inexpensive system. Only the sensor must be precisely aligned; not the entire mount.

In conjunction with this accurate closed-loop guidance for individual mirrors, a central control system will be required for gross adjustments of the mirror field for defocusing, reacquisition of the sun, or protection from the elements.

Closed-Loop Sensor

A simple but effective sensor that has been used in the past consists of a tube that sits in the reflected solar radiation and is aligned with the aperture of the cavity. A pin hole or lens at the low end of the tube directs or focuses the reflected image of the sun onto four photocells located at the upper end of the tube. Figure 6-7 shows this quad photocell configuration.

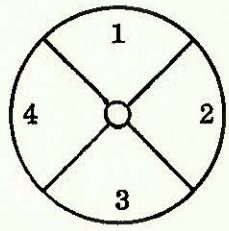

Figure 6-7. Quad Photocell Configuration

Photocells 1 and 3 operate together into a differential operational amplifier to provide a vertical error signal. Photocells 2 and 4 operate similarly to produce a horizontal error signal. The error signals drive the respective axis of the mirror until the reflected image falls onto the center of the quad photocell. As long as the sensor tube is correctly aligned, the reflected radiation will be properly redirected.

Either photovoltaic or photoresistive cells work equally well. Photoresistive cells presently are about five times less expensive, however. When a signal is generated on one of the photovoltaic cells it is amplified and drives the servo mechanism on the appropriate axis. If photoresistive cells are used, the pairs operate as a balanced bridge. As the resistance goes down on the cell with the most light, a signal is sent to change the corresponding mirror axis.

An in-line sensor with both a wide angle acquisition and a precision tracking sensor incorporated into a single tube has been built and tested. A hole is located in the center of the wide angle quad photocell so that as the image of the sun moves in on the wide angle sensor it eventually goes through the hole and falls onto the second quad photocell which allows precise mirror adjustment. The two quad photocells operate electrically in parallel.

Testing

To check different in-line sensor configurations and to determine if the in-line sensor concept is compatible with all mirror/mount axis orientations, an 18-inch square mirror was mounted on a modified telescope stand (Figure 6-8). The mount used two 5W AC motors and a 1:150,000 gear ratio. The in-line sensor appears to work properly with axis orientations II, III, IV, and V defined in Table 6-2.

To further test tracking accuracy, a gimbled mount was built on which a 6-foot diameter mirror can be mounted. The axes of the mount are driven by AC motors running through a 75,000:1 gear ratio. Tracking accuracy was monitored using a target made of 48 adjustable photocells located in a cross pattern as shown in Figure 6-9. Preliminary testing indicates the mount tracks within ±2 minutes.

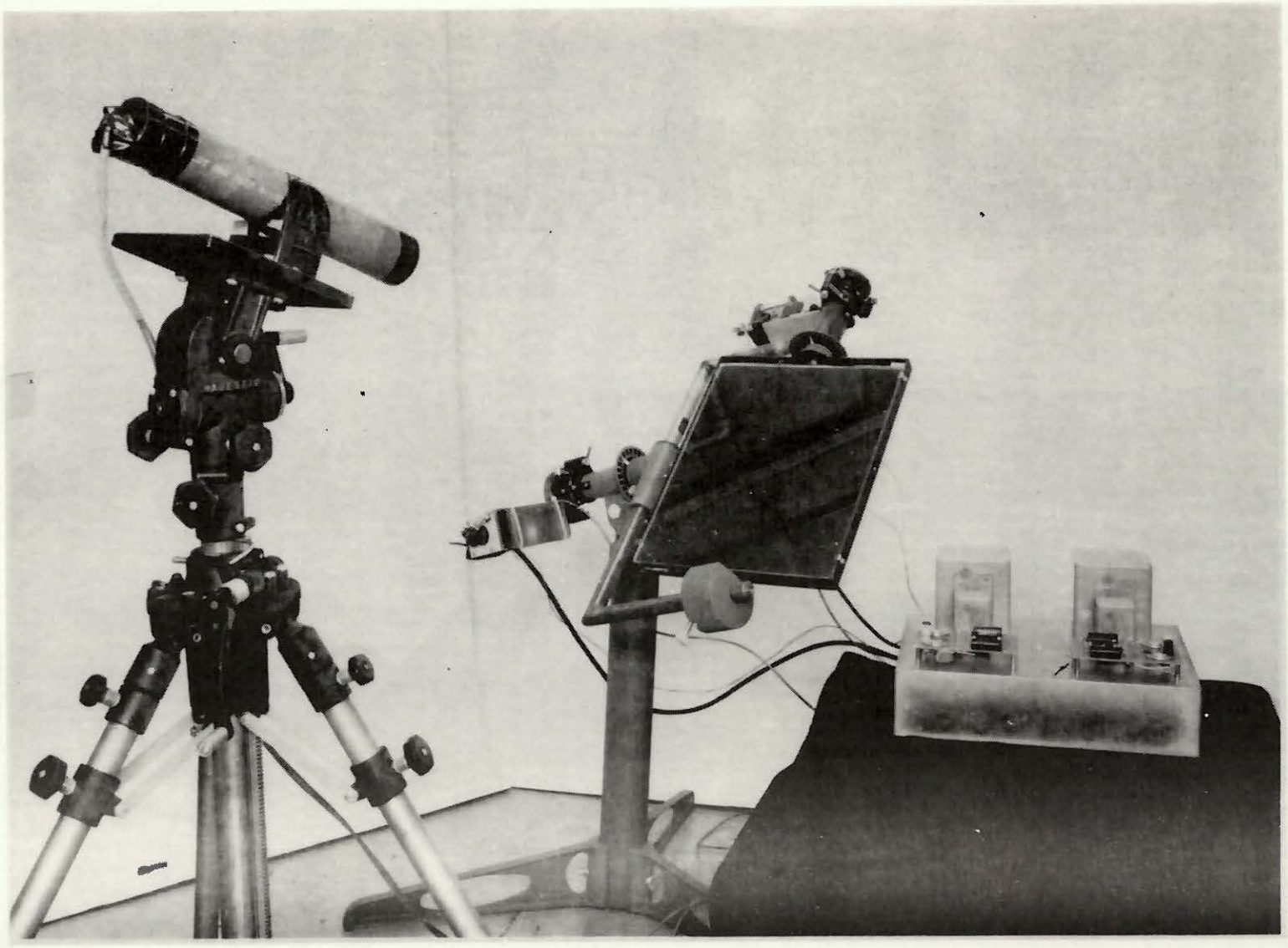

Figure 6-8. Tracking Test Apparatus

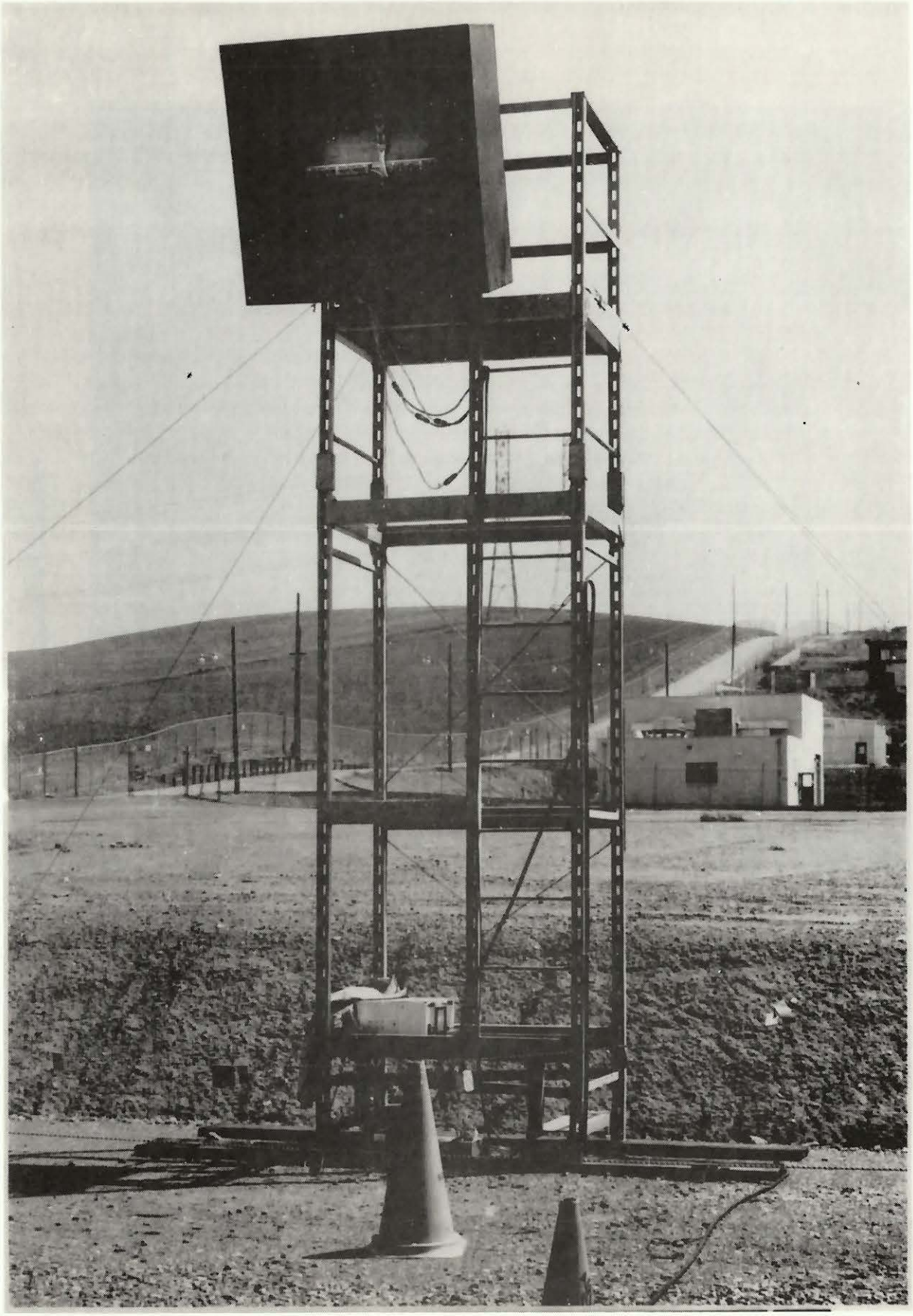

Figure 6-9. Mirror Target

6.2 Cost Optimal Deployment of Mirrors Associated With a High Temperature Solar Energy System

Nomenclature

$\mathcal{G}$	family of locally uniform rectangular arrays
$\mathcal{M}$	family of mirror density functions
$\mathcal{R}$	family of row spacing functions
V	redirected energy from a (not necessarily realizable) array of mirrors
M	mirror density function
R	mirror row spacing function
J	incident energy per unit of unshadowed mirror area
H	fraction of mirror area neither blocked nor shadowed
U	redirected energy per unit of mirror field area
L	Lagrange function
K	cost units per unit of redirected energy
T	mirror field region
C	unit mirror cost
$\underset{\sim}{v}$	position vector of a point in the mirror field relative to the base of the tower
t	time of year
r	value of row spacing
c	value of column spacing
m	value of mirror density
dw	element of mirror field area

Γ area of mirror field (the area of T)

λ Lagrange multiplier

δ mean zenith path atmospheric transmissivity

γ mirror area or mirror area bound

ρ mirror reflectivity

s edge length of square mirror

An absorbing cavity or collector of solar energy is mounted on a tower which is assumed to be erected over horizontal terrain. Located about the base of the tower are many relatively small mirrors of predetermined size. The bases of the mirror mounts are rigidly attached to the ground. During daylight hours, each mirror is continuously positioned so that the specular component of incident sunlight is reflected into an aperture located in the base of the cavity.

In this paper, a sharp upper bound is found on the maximum energy that can be redirected into the aperture by an array of mirrors belonging to a certain family G (the class of locally uniform rectangular arrays) whose total surface area is not more than some preassigned value. The upper bound is obtained by building up an optimal mirror array in local blocks. Although these blocks may not combine to generate a realizable deployment, their properties should be of assistance in finding superior members of G. This method can be applied without modification to much more inclusive classes than G but not without an increase in the use of computer resources. These results are combined with a simple cost model to obtain a lower bound on the minimum cost per unit of redirected energy as a function of the unit mirror cost.

Site latitude, mirror reflectivity, time of year during which collection takes place, atmospheric transmissivity, and mutual shadowing and blocking by neighboring mirrors are taken into account.

Mirror Field Optimization

Consider the relations

$$V(M,R) = \int_T \int_{t_1}^{t_2} J(\underset{\sim}{v},t)\, M(\underset{\sim}{v})\, H(M(\underset{\sim}{v}), R(\underset{\sim}{v}), \underset{\sim}{v}, t)\, dt\, dw \tag{1}$$

$$\int_T M(\underset{\sim}{v})\, dw \leq \gamma \tag{2}$$

In this discussion, J is the number of units of specular solar energy incident on an unshadowed unit of mirror surface per unit of time. The value of J takes into account the tilt of the mirror surface and the absorption of specular solar energy by the atmosphere [2]. The location of the mirror relative to the tower base is given by the vector $\underset{\sim}{v}$ and t represents the time. $M(\underset{\sim}{v})$ is the number of units of mirror area per unit of ground area in the vicinity of $\underset{\sim}{v}$. H is the fraction of the mirror surface at $\underset{\sim}{v}$ and time t which is neither blocked nor shadowed. For the application reported on in the paper, the value of H is obtained at $\underset{\sim}{v}$ by assuming that there is a mirror at $\underset{\sim}{v}$ which is surrounded by a block of 24 neighboring mirrors deployed as in Figure 6-10. The block pattern is uniform and rectangular with row spacing R and density M. T is the region over which the integration is performed and dw is the element of area. Clearly, V(M, R) can be interpreted as an approximation to the total energy redirected into the aperture during the time interval (t_1, t_2) by a uniform rectangular mirror array deployed over T; relation (2) states that the deployed mirror area is less than γ. In fact, for mirror deployments which are very nearly uniform and rectangular in the vicinity of each of their mirrors, V(M, R) represents an excellent approximation for the total redirected energy provided early morning and late afternoon radiation is ignored. The class of mirror deployments which have this local property is denoted by G.

The Mirror Arrays, G

The purpose of this section is to clarify the definition of the class G and to provide a precise definition for the functions in the integrand of Equation (1) for any member of G. A mirror array G belongs to G if and only if for each mirror in G (other than edge mirrors) a block of 25 mirrors of the type shown in Figure 6-10 can be found whose mirror configuration closely approximates the mirror configuration in the vicinity of the given mirror in G. Since the blocks used in the computation of H are restricted to be of the type shown in Figure 6-10, a member of G must have rows and

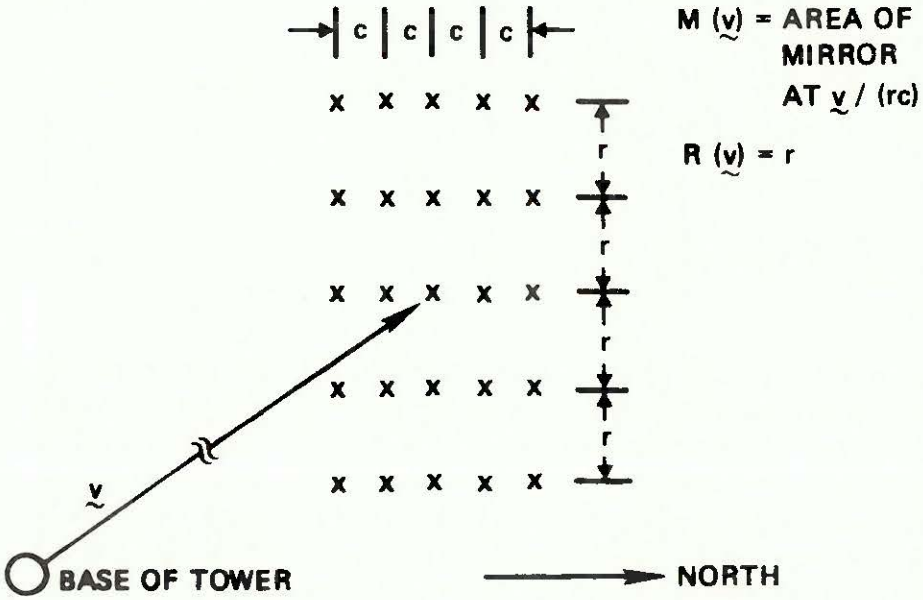

Figure 6-10. Typical Block Pattern

columns which, though possibly curved, do not depart much from a north-south, east-west direction. The row and column spacing can vary across the array but the variation must be gradual.

Figure 6-11 is a map of the west half of a mirror array which belongs to *G* and which happens to have straight rows and columns. Although any 5 x 5 rectangular block of the array can be closely approximated by a block of the type used to compute H, the mirror density varies by about a factor of two across the array.

Suppose that a rule has been agreed upon for associating with each mirror of each array in *G* a best approximating rectangular 5 x 5 block (Figure K-1). This can be done in a variety of reasonable ways, any one of which would be satisfactory for the following. The mirror density M at the center of any mirror is then defined to be the mirror density in the

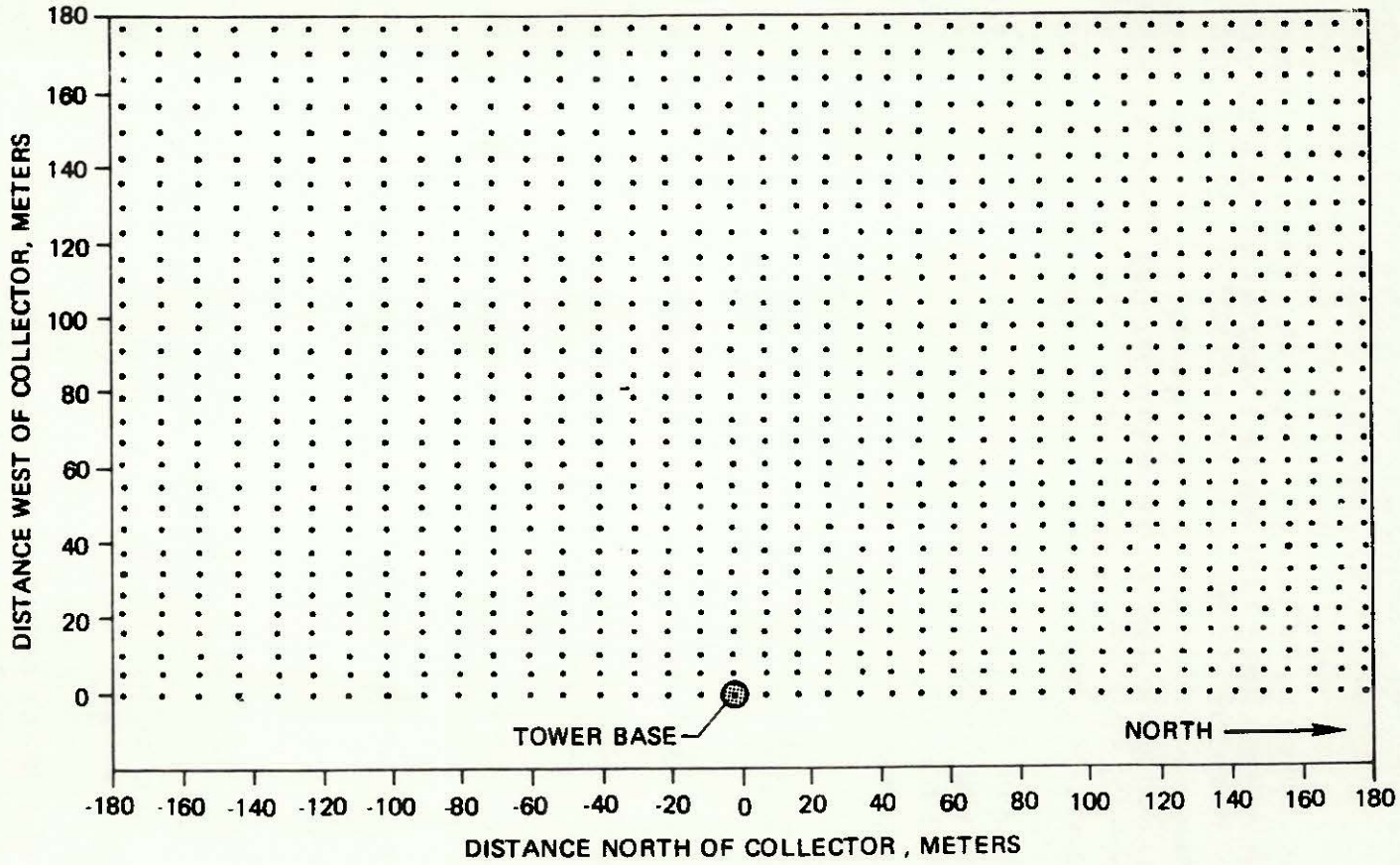

Figure 6-11. Map of Mirror Array

approximating block. The row spacing function R is defined similarly. Finally, one extends the definitions of M and R in any reasonable fashion to all points of the field. Now it can be seen that for any member G of G the right-hand side of Equation (1) is well-defined and its value is an approximation to the redirected energy obtained from G during the time interval (t_1, t_2).

There is one remaining difficulty. For locations near the edge of the mirror field, it is obvious that no satisfactory approximating blocks of the type discussed can be found. In the application to follow, this problem is ignored by imagining the mirror array to be extended beyond T in a regular way and then by selecting the appropriate approximating block to the extended array. In other words, edge effects are ignored. The optimization method can be used, however, in a way that accounts for edge effects (see Extensions).

Every member of G is said to be a locally uniform rectangular array. It would be desirable to find that member of G whose total mirror area does not exceed γ and which maximizes the redirected energy. Since this problem seems to present great difficulties, a closely related but different problem is solved instead.

The Method of Optimization

The problem that is solved is finding functions M and R which maximize V(M, R) as defined in Equation (1) and which satisfy the area constraint of relation (2). The class of admissible density functions M consists of all the real valued functions whose values are between zero and one and which are defined on T. The class of admissible row spacing functions $R(M)$ depends on which density function M is chosen. This dependency arises from the requirement that mirrors shall not overlap when they are oriented so that their surfaces are horizontal.

Thus the new problem is to find functions M and R which maximize V(M, R) as M runs over M and for each such M, R runs over $R(M)$ and M is subject to the constraint

$$\int_T M(v)dw \leq \gamma$$

Since M and $R(M)$, $M \epsilon M$ include all the density and row functions corresponding to the members of G, it follows that if (M*, R*) is a solution, then V(M*, R*) is an upper bound on the maximum redirected energy obtainable from any element of G which satisfies the area constraint. For the application discussed below V(M*, R*) is, in fact, a fairly sharp upper bound. Although (M*, R*) may not correspond to any member of G, it should be useful in searching for superior members of G.

To solve the new problem, one can proceed as follows:

Let λ be a positive real number; let

$$U(M(\underset{\sim}{v}), R(\underset{\sim}{v}), \underset{\sim}{v}) \equiv \int_{t_1}^{t_2} J(\underset{\sim}{v}, t)\, M(\underset{\sim}{v})\, H(M(\underset{\sim}{v}), R(\underset{\sim}{v}), \underset{\sim}{v}, t)dt$$

and

$$L_T(M, R, \lambda) \equiv \int_T U(M(\underset{\sim}{v}), R(\underset{\sim}{v}), \underset{\sim}{v})dw - \lambda \int_T M(\underset{\sim}{v})dw \tag{3}$$

It is well known [1] that if $(M_\lambda{}^*, R_\lambda{}^*)$ maximizes the right-hand side of Equation (3), then $(M_\lambda{}^*, R_\lambda{}^*)$ maximizes $V(M, R)$ where M is subject to the constraint,

$$\int_T M(\underset{\sim}{v})dw \leq \int_T M_\lambda^*(\underset{\sim}{v})dw \tag{4}$$

Thus the constrained problem (with some constraint) is solved if an unconstrained problem is. Actually, no particular value of γ is preferred--in fact, solutions are desired for a range of values of γ. It turns out that by judicious selection of a family of values for λ, the corresponding γ's range over the interval of interest (where, of course, $\gamma = \int_T M_\lambda{}^*(\underset{\sim}{v})dw$).

Now one can write,

$$\begin{aligned} \max_{M \in \mathcal{M},\, R \in \mathcal{R}(M)} L_T(M, R, \lambda) &= \max_{M \in \mathcal{M},\, R \in \mathcal{R}(M)} \int_T (U(M(\underset{\sim}{v}), R(\underset{\sim}{v}), \underset{\sim}{v}) - \lambda M(\underset{\sim}{v}))dw \\ &= \int_T \max_{m \in [0,1],\, r \in [s, s/m]} (U(m, r, \underset{\sim}{v}) - \lambda m)dw \end{aligned} \tag{5}$$

Since r can be bounded independent of m and since $(U - \lambda m)$ is bounded, for each $\underset{\sim}{v}$ there is a pair (m_λ, r_λ) which maximizes the integrand. The desired solution functions $M_\lambda{}^*$ and $R_\lambda{}^*$ are those that have these values at each $\underset{\sim}{v}$ in T. Thus the problem of maximizing a functional (L_T) reduces to maximizing a function of two variables at each point in T. Efficient numerical techniques exist for estimating these maxima.

Effect of Mirror Reflectivity

If each mirror has the same reflectivity ρ, then optimal deployments are independent of the value of ρ. This can be seen as follows. If the mirror reflectivity is ρ and $0 < \rho < 1$, then the right-hand side of Equation (1) should contain ρ as a factor and similarly Equation (3) should be written (in condensed notation) as

$$\int_T (\rho U - \lambda M)dw = \rho \int_T [U - (\lambda/\rho)M]dw$$

Clearly if $(M_\lambda^*, R_\lambda^*)$ maximizes $\int_T (\rho U - \lambda M)dw$, then it maximizes $\int_T (U - (\lambda/\rho)M)dw$ and vice versa. This proves the assertion.

A Simple Cost Model

Suppose that the cost of all the elements of the solar energy collecting array other than the mirrors is independent of the area of mirrors deployed. Then it is convenient to measure all other costs in terms of this cost. This amounts to setting the non-mirror costs equal to unity. With this unit of cost, let C be the cost of Γ units of mirror area where Γ is the area of the region T. Then if γ units of mirror surface are optimally deployed in T, the total cost is

$$1 + C(\gamma/\Gamma)$$

and the cost per unit of redirected energy K is given in

$$K(\gamma) = [1 + C(\gamma/\Gamma)]/V(M_\gamma', R_\gamma')$$

where (M_γ', R_γ') corresponds to the best deployment from G satisfying the area constraint γ. If now M_γ^*, R_γ^* represent the functions which maximize V for the area constraint γ, then

$$K(\gamma) \simeq [1 + C(\gamma/\Gamma)]/V(M_\gamma^*, R_\gamma^*) \tag{6}$$

To the extent that M_γ^*, R_γ^* represents a realizable mirror field, the approximation is good--in any case, the right-hand side of Equation (6) represents a lower bound on $K(\gamma)$.

An Application and Results

Specifications

T is a square region 360 meters on a side; the collector tower is centered in T with its absorbing aperture 100 meters above the mirror field. The mirrors are 5 meter squares aligned so that when a mirror normal is vertical, the mirror edges are aligned east-west and north-south. The time interval t_1, t_2 is selected to correspond to that part of a day during which the elevation angle of the sun is greater than or equal to 10°. The latitude of the site is 37.5°. The model used for atmospheric absorption of specular sunlight is that given in [2]. In that model, the mean zenith path transmissivity δ determines the clarity of the atmosphere. ($\delta = 0.9$ approximates local measurements made on a clear winter day in Livermore, California.) For a non-absorbing atmosphere, $\delta = 1.0$.

Computations are performed for transmissivities of 1.0 and 0.7 for a mid-summer and for a mid-winter day. Simplifications and approximations used are:

- Edge effects are ignored.
- To compute H (see Equation (1)), the neighboring 24 mirrors are assumed to have surfaces parallel to the mirror surface at which H is evaluated.
- The earth revolves about the sun in exactly 365 days in a circular orbit.
- Mirror reflectivity is constant and equal to unity.

Results

Figures 6-12 through 6-16 provide a summary of the data computed for mid-summer and for a zenith transmissivity of 0.7. In these figures, data denoted "variable density" is obtained by using $V(M_\gamma^*, R_\gamma^*)$ for the redirected energy. "Constant density" refers to those arrays with straight rows and columns which are equally spaced, i.e., to globally square arrays.

For a given area constraint γ, let (M_γ^S, R_γ^S) denote the best square array. In Figure 6-12, both $V(M_\gamma^*, R_\gamma^*)$ and $V(M_\gamma^S, R_\gamma^S)$ are plotted as functions of γ.

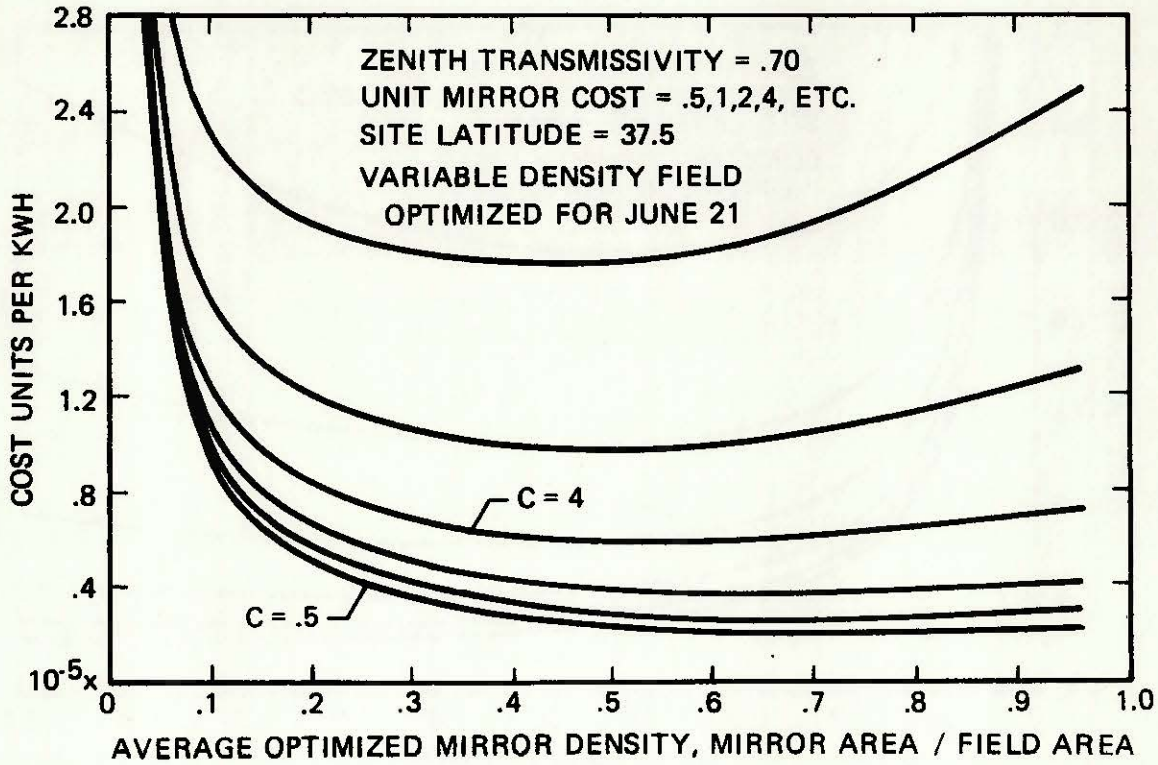

Figure 6-13. Cost Per KWH Versus Mirror Density for Variable Density Fields

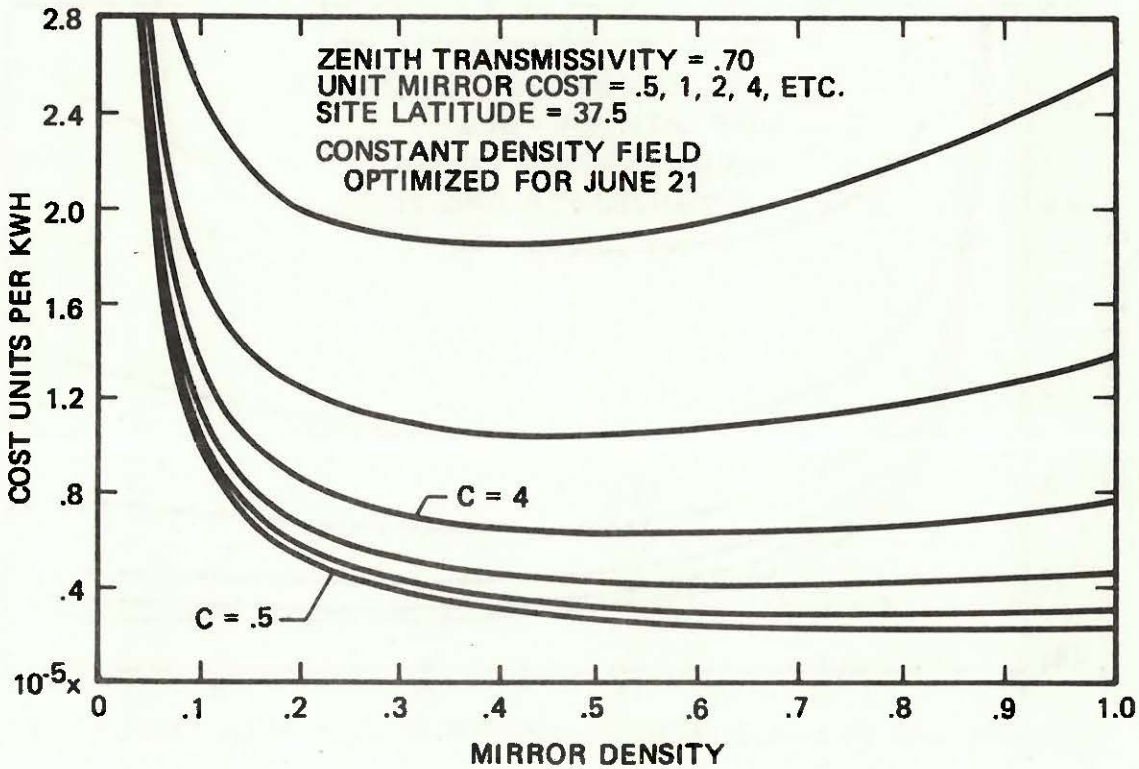

Figure 6-14. Cost Per KWH Versus Mirror Density for Constant Density Fields

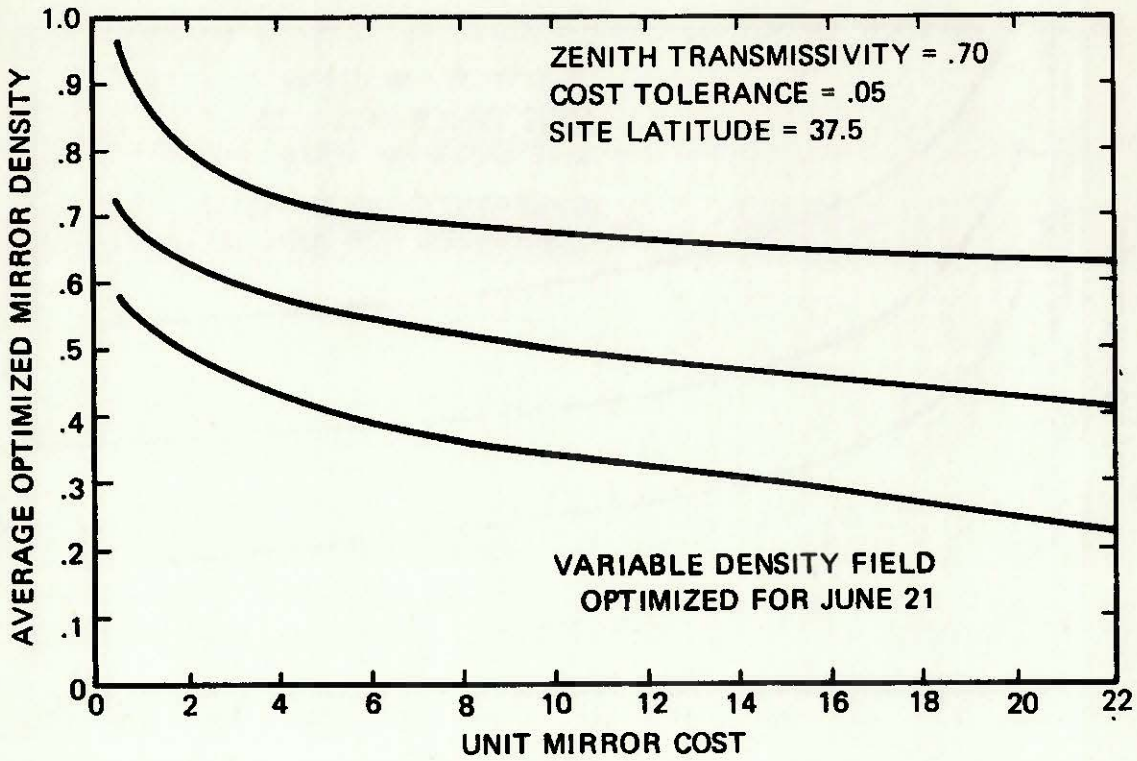

Figure 6-15. Mirror Density Five-Percent Cost Tolerance Band Versus Unit Mirror Cost for Variable Density Fields

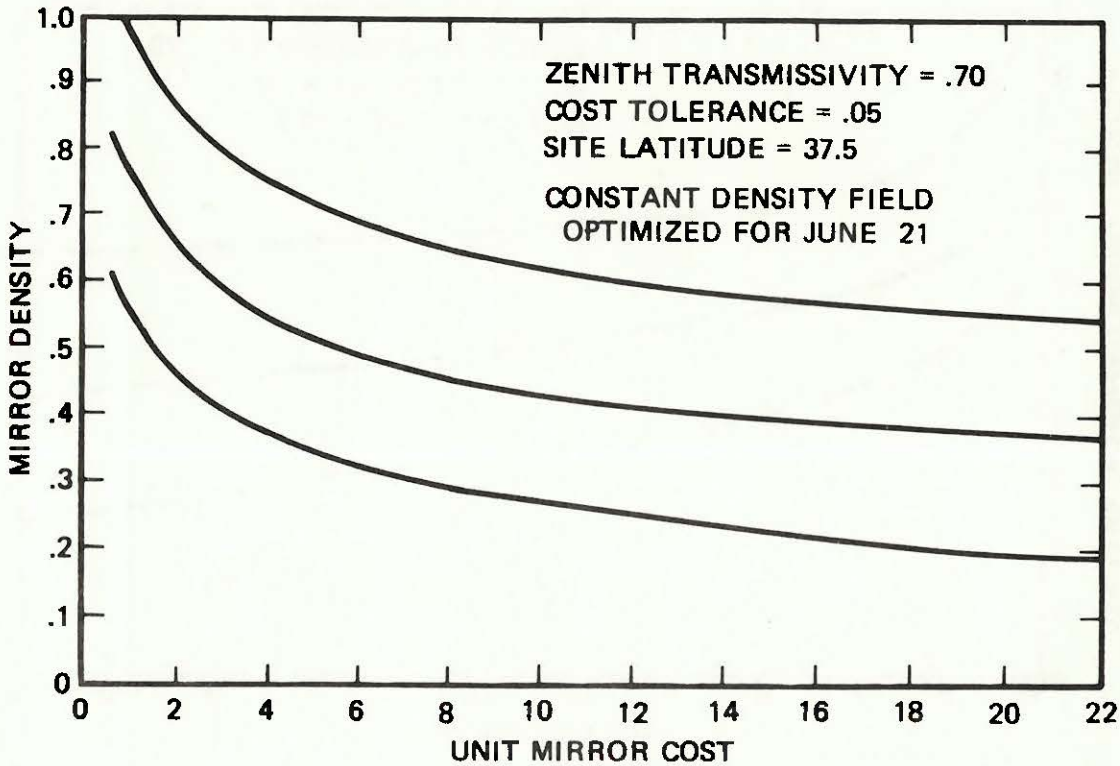

Figure 6-16. Mirror Density Five-Percent Cost Tolerance Band Versus Unit Mirror Cost for Constant Density Fields

Since

$$V(M_\lambda^s, R_\lambda^s) > 0.9\,V(M_\gamma^*, R_\gamma^*)$$

for every value of γ, it seems likely that some member of G comes exceedingly close to achieving the upper bound on the redirected energy. Another significant result is that globally square arrays are almost as effective as members of G. These conclusions hold for mid-winter and for $\delta = 1.0$ as well. Thus the right-hand side of Equation (6) is a good approximation to $K(\gamma)$.

In Figure 6-13, $K(\gamma)$ is plotted versus the average optimized mirror density for variable density fields for several values of the parameter C, the unit mirror cost. As would be expected, the best average density becomes smaller as the unit mirror cost grows larger. The flatness of these curves in the vicinity of their minima is impressive. Figure 6-14 displays the same information for constant density arrays. Again, it is seen that globally square arrays are almost as cost effective as the best member of G.

Figure 6-15 shows three graphs. The middle one is a plot of the best average optimized mirror density for variable density arrays as a function of unit mirror cost. The top and bottom curves show the magnitude of the departure from the best average density that can be made without increasing the cost per unit of redirected power more than five percent. Figure 6-16 presents the same data for constant density arrays.

By reviewing all the data (only one-fourth is shown) obtained for $C = 4$, it appears that a constant density field of density 0.45 is within about 12 percent (in terms of cost per unit of redirected energy) of the best member of G where the member of G is tailored to be optimal for the particular day and atmospheric condition prevailing for a mid-winter or mid-summer day and for $\delta = 1.0$ or 0.7. Similar results hold for other values of C.

Extensions

The results above show that the best locally rectangular array is not very much better than a globally square array (the simplest array of all). In current work, optimization is being performed over a much larger class than G. The enlargement is achieved by permitting rows and columns in the blocks defining H to meet in a common but arbitrary angle and by allowing arbitrary row-column orientation with respect to north. Further enlargement appears to be limited by available computer time.

Other modifications being considered may yield increased mirror effectiveness. For example, the region T need not be square. Its size and shape can be parameters subject to optimization. The tower need not be centered in the mirror array. It is easy to show that if functions M_γ^*, R_γ^* are solutions for the entire plane, then M_γ^*, R_γ^* restricted to any subset of the plane is also a solution provided edge effects are ignored. This suggests that edge effects be considered only for a final trimming of an array obtained by ignoring edge effects.

REFERENCES

1. H. Everett III, Generalized Lagrange Multiplier Method for Solving Problems of Optimum Allocation of Resources, Operations Research, 11, 401, 1963.

2. B. J. Garnier and Atsumu Ohmura, Evaluation of Surface Variations in Solar Radiation Income, Solar Energy, 13, 22, April 1970.

7.0 Power Plant Considerations (Bechtel Corporation Study for Sandia Laboratories, June 1974)

Selection of a suitable power plant was based on several key design criteria supplied by Sandia Laboratories. These are listed below:

- 850°F steam temperature
- Albuquerque, New Mexico, site location
- 200 to 400m tower height range
- auxiliary fossil fuel firing
- no energy storage system
- 10° right circular conical volume under the cavity for power plant location at base of tower

Size Selection

The tower height range of 200m to 400m yields a collected solar power range of 130 to 500 MW_t. Using a rough plant efficiency of 33 percent, this yields a solar power plant output range of 43 to 167 MW_e. Within this range, three power plant outputs were selected for this study: 50, 100, and 150 MW_e.

Cooling Type and Water Requirements

Both dry and wet cooling were investigated for this study. The main advantage of wet cooling is lower capital cost by a factor of up to 10 compared to dry cooling. Mechanical draft wet towers were chosen over natural draft wet towers since experience has shown that the latter are only economic by comparison in areas with high relative humidity and low average wet bulb temperatures. If closed cycle dry cooling became necessary because of water scarcity, a direct condenser cooling system, such as the GEA (Gesellschaft für Luftkondensation) system, would probably be more economical than a dry tower for power plants in the 50 to 150 MW_e range considered in this study. Constraints associated with wet towers include water requirements for evaporation and blowdown and potential mirror field interference problems caused by the cooling tower plume and drift. These constraints were considered.

A preliminary investigation into surface and ground water availability in the Albuquerque area indicates that sufficient water is available at present. However, a more definitive study is necessary to predict the future supply. At any rate, it must be recognized that the sufficient water supply at the hypothetical site of Albuquerque is a fortuitous coincidence and is not typical of other potential solar power plant sites. The choice of a cooling system will have to be considered on a case to case basis. For the purposes of this preliminary study it was assumed that sufficient water is available for wet cooling.

Experience has shown that in dry climates, cooling tower plumes are small. Also, even in average climate areas, mechanical draft tower drift fallout rarely extends beyond 900 feet downwind. Consequently, it was decided that wet mechanical draft towers located 1500 feet downwind from the mirror field outer rim would be acceptable.

Alternate Fuel

Auxiliary fossil fuel firing during extended periods of low insulation and nighttime is included to provide a stable and continuous power supply. Coal is available within a few hundred miles of Albuquerque. In view of predicted future oil and gas shortages, coal was chosen as the logical fuel.

Cycle Selection and Performance

A schematic diagram of the power cycle arrangement is shown in Figure 7-1. Pending further studies in the technical and economic feasibility of integrating the Hitec boiler and the coal fired boilers into a single steam generator, it was decided to have these units separated as shown. For simplicity, one turbine is shown with one extraction for feedwater heating. In fact, for the three plants under consideration there would probably be a high- and low-pressure turbine and from two to five stages of feedwater heating. Turbine manufacturers have indicated that reheat would not be economical for these sizes and conditions.

The throttle pressure of 800 psig was selected from a review of previous power plants and discussions with turbine manufacturers. The 850°F throttle temperature is the basis for this selection. Cycle performance for the three plants together with their respective tower heights and coal consumption rates is summarized in Table 7-1. Overall efficiencies fall in the range of 32.8% to 36.5% for the solar energized cycle and 28.5% to 31.7% for the fossil fired cycle. The efficiency of the solar energized cycle is defined as the net output of the plant per thermal energy input from the steam fed by the Hitec heater. The slightly higher numbers compared with the coal fired cycle efficiencies reflect the exclusion of boiler inefficiencies in the solar energized cycle.

TABLE 7-1. PLANT PERFORMANCE

	Net Output, MW_e		
	50	100	150
Throttle temperature, °F	850	850	850
Throttle pressure, psig	800	800	800
Back pressure, in. Hg	2.5	2.5	2.5
Approx. throttle flow, lbs/hr	500,000	1,000,000	1,500,000
Gross heat rate, Btu/kW_eh	9800	8800	8800
Gross output MW_e	53.2	106.4	159.6
Net output MW_e*	50	100	150
Solar plant efficiency**	32.8	36.5	36.5
Fossil plant efficiency***	28.5	31.7	31.7
Coal comsumption tons/hr			
100% capacity	35.8	64.3	96.6
50% capacity	17.9	32.15	48.3
Collected solar power, MW_t	152	274	410
Tower height, meters	215	290	350
Mirror field dia., meters	2440	3300	3980
10° area dia., meters	250	335	404

*Assumes 4% of gross output for plant auxiliaries and 2% of gross output for Hitec pumping and miscellaneous electrical requirements associated with the solar energy collection system.

**$\text{Efficiency} = \dfrac{\text{Net output}}{\text{Collected solar power}}$

***$\text{Efficiency} = \dfrac{\text{Net output}}{\text{Coal HHV x Coal consumption}}$ (HHV = 8400 Btu/lb)

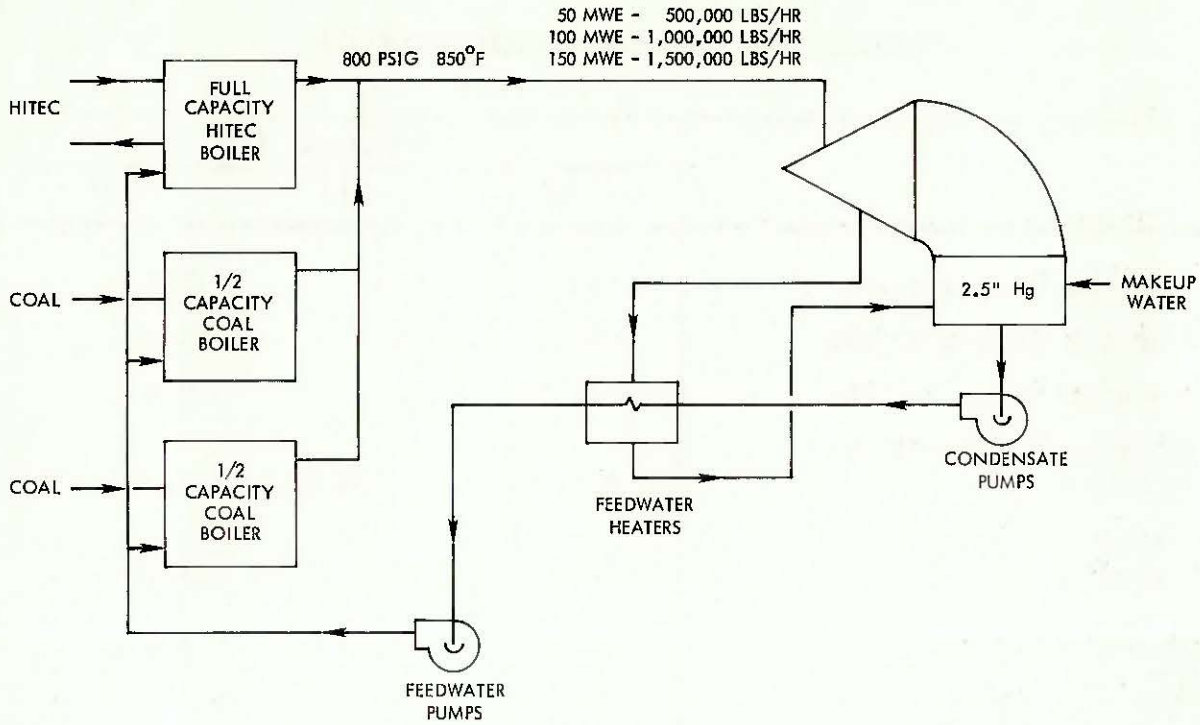

Figure 7-1. Power Cycle Arrangement

Plant Arrangement

A typical plot plan is shown in Figure 7-2 for the 100 MW_e plant. The power plant including switchyard, power building, stack, and office and machine shop area is located in the center of the mirror field. The tower is shown penetrating the power building. Hot Hitec would be piped directly to the Hitec boiler at the base of the tower. An access road is provided around the power plant. The 10° conical volume underneath the tower appears to be marginally sufficient as illustrated in Figures 7-3, 7-4, and 7-5. Plant areas are estimated from completed power plants with comparable outputs. The plant will probably be slightly larger because of Hitec equipment, storage, and pumping. However, much of this equipment could be located at different levels within the base of the tower. As the plant output decreases the plant area per kilowatt increases and 50 MW_e appears to exceed the lower limit for 10° conical volume. Sandia Laboratories have indicated, however, that the available area could be increased somewhat without significant penalty.

Referring to Figure 7-2, water treatment, cooling towers, and coal storage are located outside the mirror field on the west side of the plant. Prevailing winds are from the south in the summer and from the northeast in the winter. The coal pile and the cooling tower are therefore not expected

to cause interference with the mirror field collection efficiency. An access road is provided and a railroad line is included for delivery of coal. Sized coal is transported by enclosed conveyor from ready storage to the power plant along side of or above the access road.

A 138-kV transmission line is shown crossing above the mirror field from the switchyard.

The 50 MW_e and 150 MW_e plants would be similar with all items being scaled accordingly.

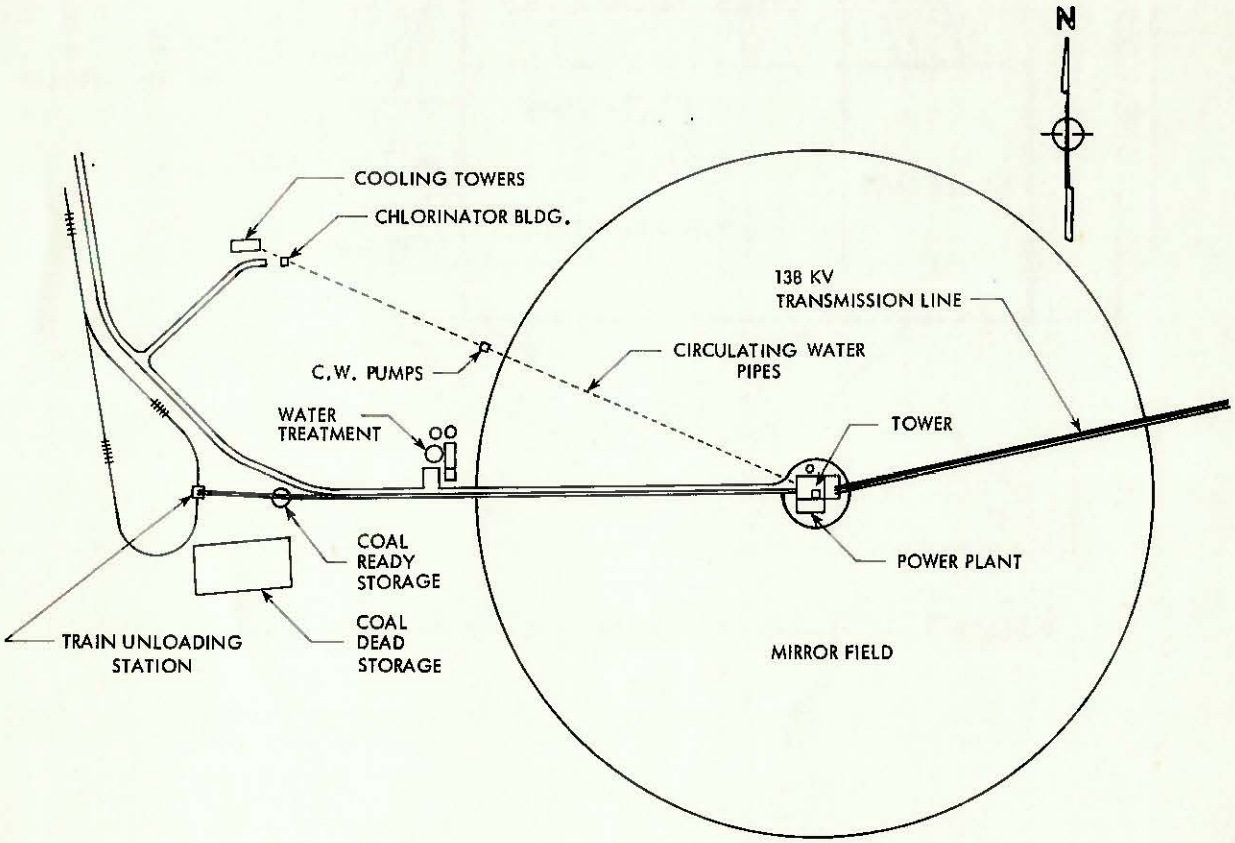

Figure 7-2. Plot Plan for 100 MW_e Plant

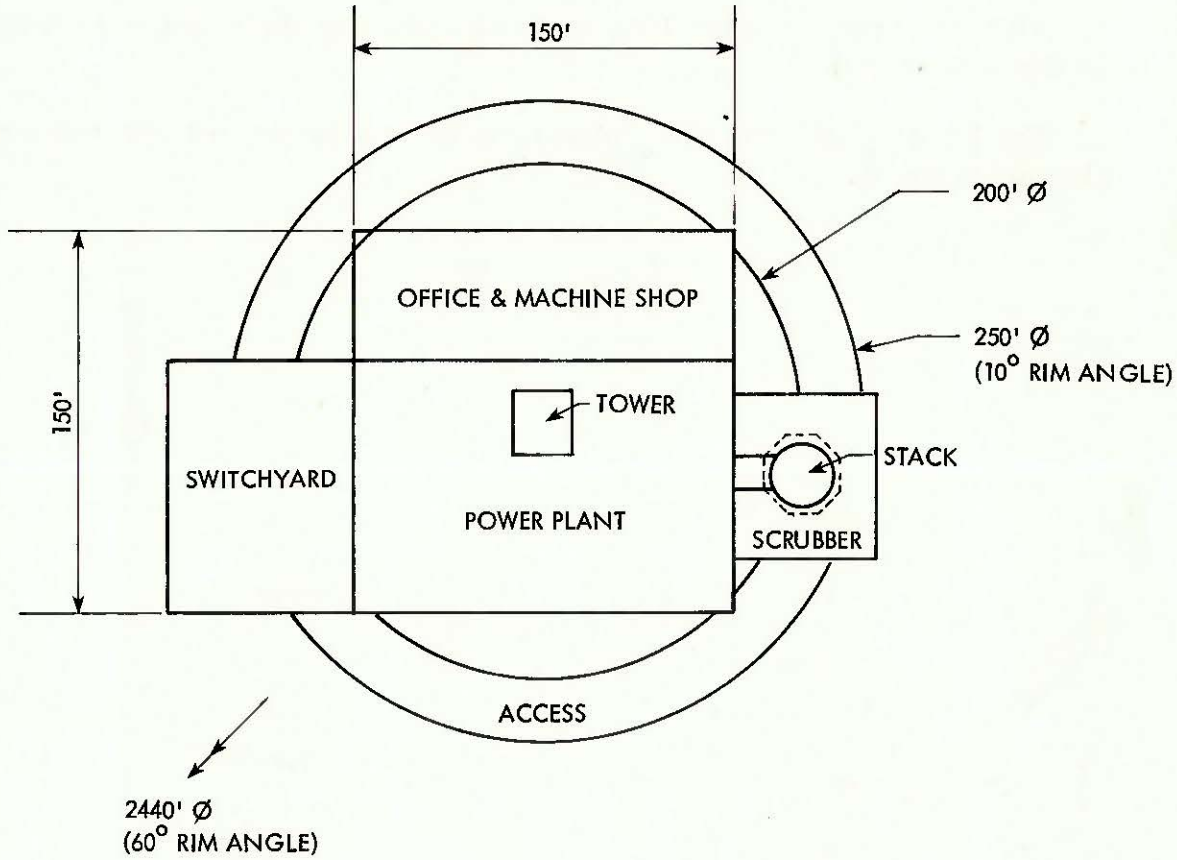

Figure 7-3. Land Area Required for 50 MW_e Plant

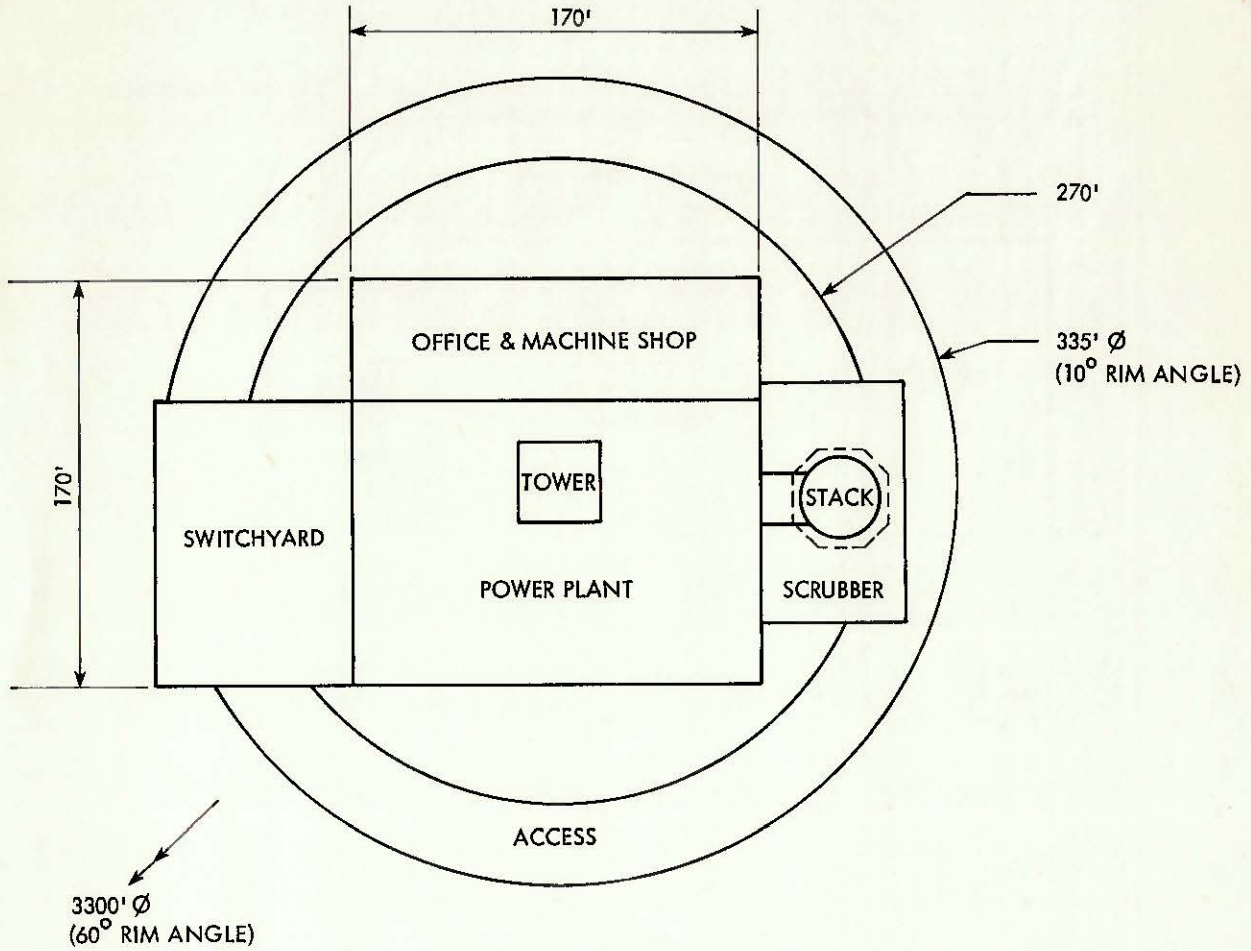

Figure 7-4. Land Area Required for 100 MW_e Plant

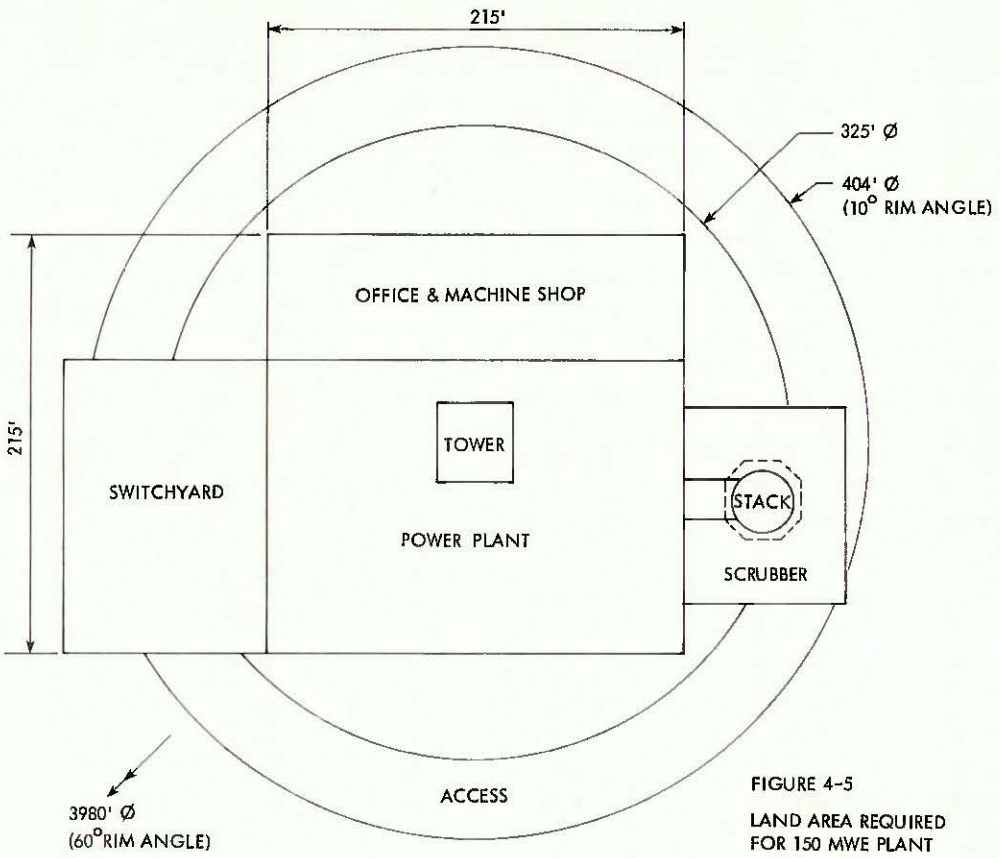

Figure 7-5. Land Area Required for 150 MW_e Plant

8.0 Economic Analysis

System and component cost estimates for solar-generated electrical power have been developed by Sandia Laboratories with inputs from Bechtel Corporation in the areas of the power house, coal-fired boiler, tower, and Hitec piping (under contract to Sandia Laboratories). The resulting capital cost estimates are shown in Table 8-1 and Figures 8-1, 8-2, and 8-3 in terms of 1974 dollars. The estimates were based on the assumption that the solar facility would be located in Albuquerque, New Mexico, together with a full capacity coal fossil plant to operate the turbine-generator when solar energy was not available. The cost bases for each of the system's components are listed below. It should be noted that the final cost estimates include a 15 percent increase to cover costs associated with land, interest during construction, small buildings, roads, and other miscellaneous costs. Costs are estimated for systems corresponding to tower heights between 200 and 400 m.

Cavity

Estimated using the weight of the cavity at 400 pound/MW_t at a cost of $12.50/pound.

Tower

Labor and materials were estimated based on design shown in Section 5.0.

Piping

Estimate was based on a combination of carbon steel and stainless steel piping.

Pumps

Estimate based on information from commercial manufacturers.

TABLE 8-1

COST ESTIMATES*

	Power Output					
	200 m 43 MW_e		300 m 110 MW_e		400 m 193 MW_e	
Description	$\$/10^6$	$\$/kW_e$	$\$/10^6$	$\$/kW_e$	$\$/10^6$	$\$/kW_e$
Cavity	0.67	16	1.5	14	2.67	14
Tower	1.05	24	1.98	18	3.25	17
Piping	1.06	25	1.50	14	3.56	18
Total	2.11	49	3.48	32	6.81	35
Pumps	0.30	7	1.0	9	2.37	12
Heat Exchanger	1.19	28	3.0	27	5.93	31
Steam Generator	0.89	21	2.0	18	3.56	18
Drain Tank	0.03	1	0.10	1	0.24	1
Buffer Tank	0.27	6	0.60	5	1.07	6
Ground Equipment	2.68	62	6.70	61	13.17	68
Mirrors $\$20/m^2$	4.05	94	9.10	83	16.18	84
Power House	10.48	244	24.13	219	34.56	179
Auxiliary Firing	11.00	256	24.00	218	34.50	179
Power Plant**	21.48	500	48.13	438	69.06	358
TOTAL	30.99	721	68.91	626	107.89	559
+15% misc.	35.64	829	79.25	720	124.07	643
TOTAL with $\$40/m^2$ mirrors	40.30	937	89.00	815	142.67	739

* Assumes power plant at base of each tower (no clustering).

** Initial estimates for 454°C steam system.

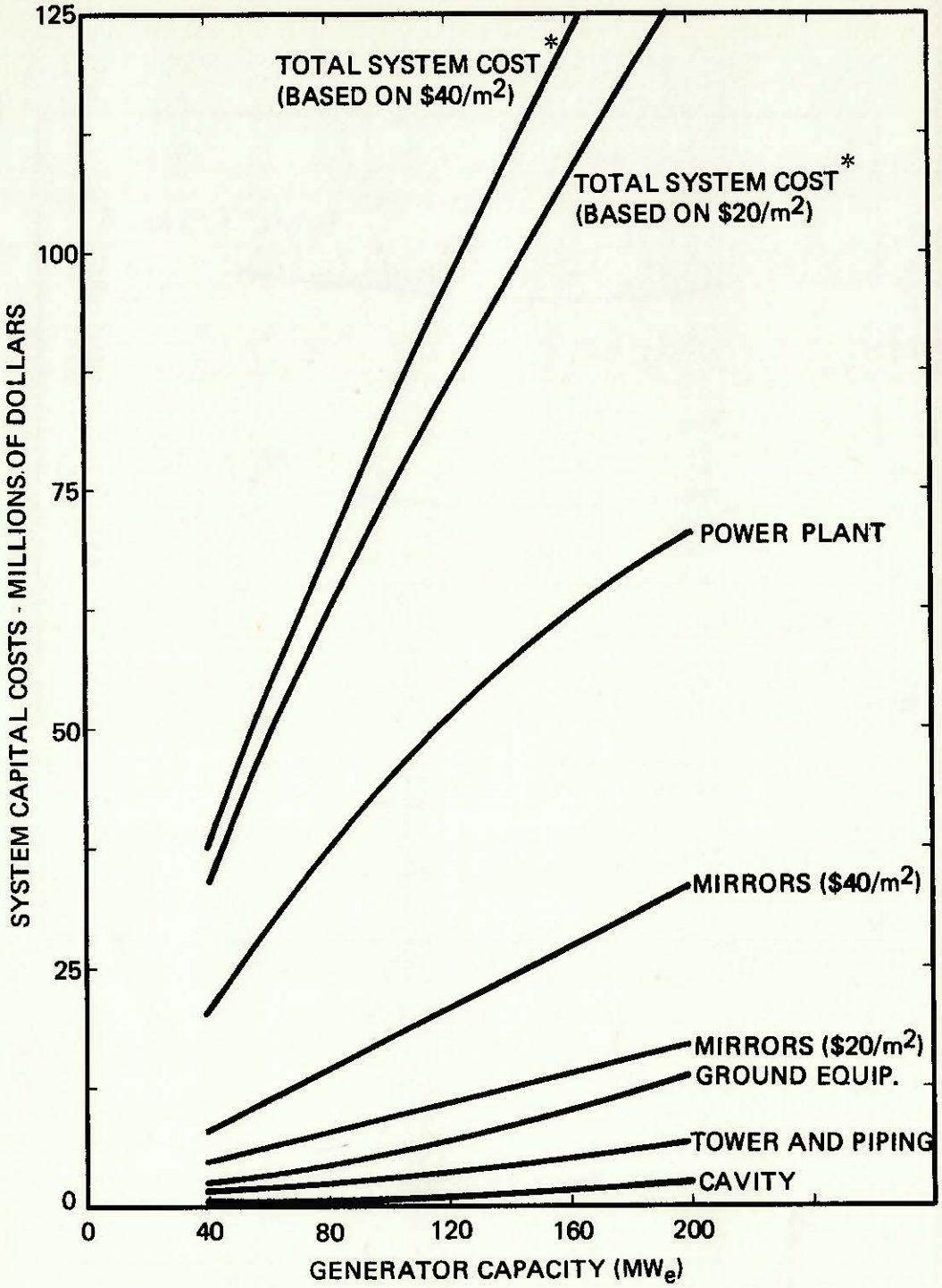

*Includes 15% for interest during construction.

Figure 8-1. System Capital Costs Versus Generator Capacity, 454°C Steam

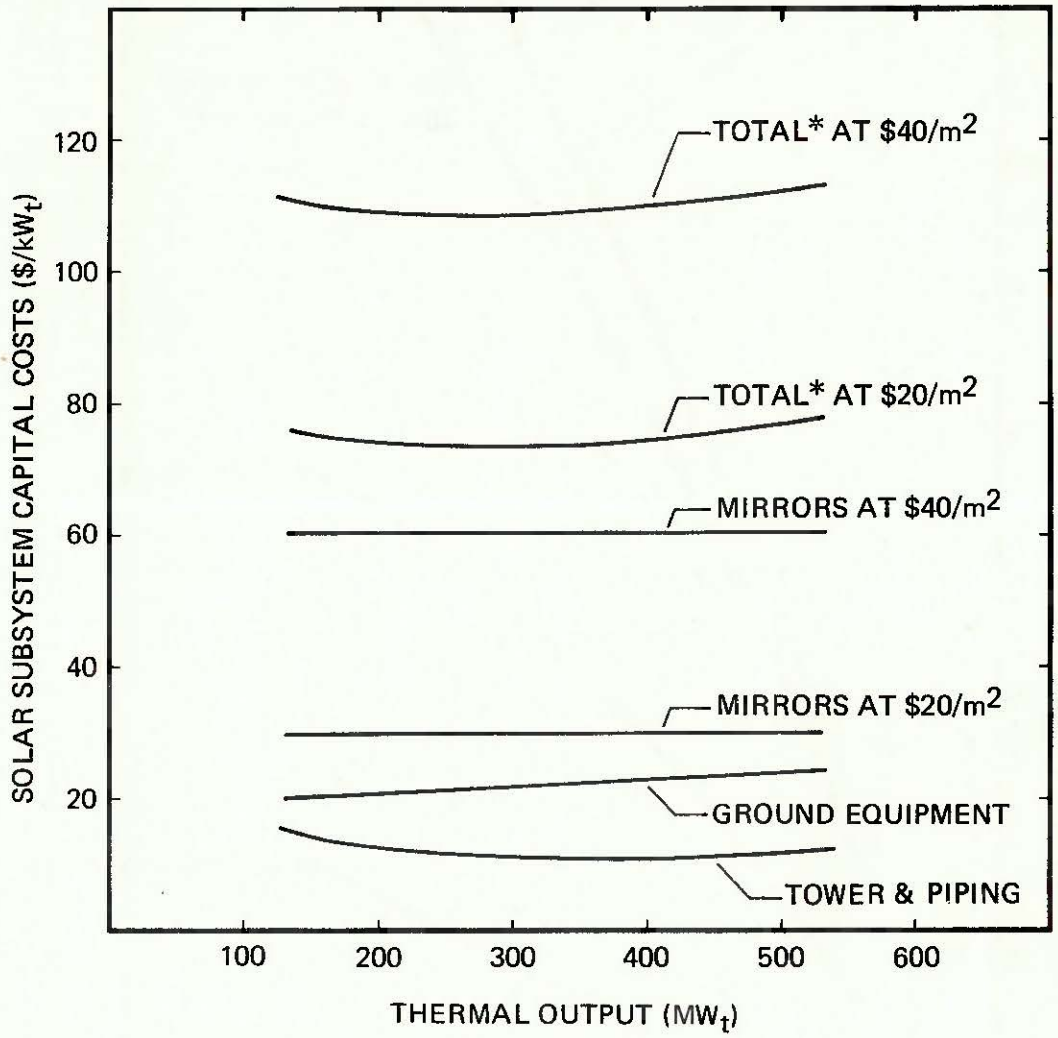

*Includes 15% for interest during construction.

Figure 8-2. Solar Subsystem Capital Costs

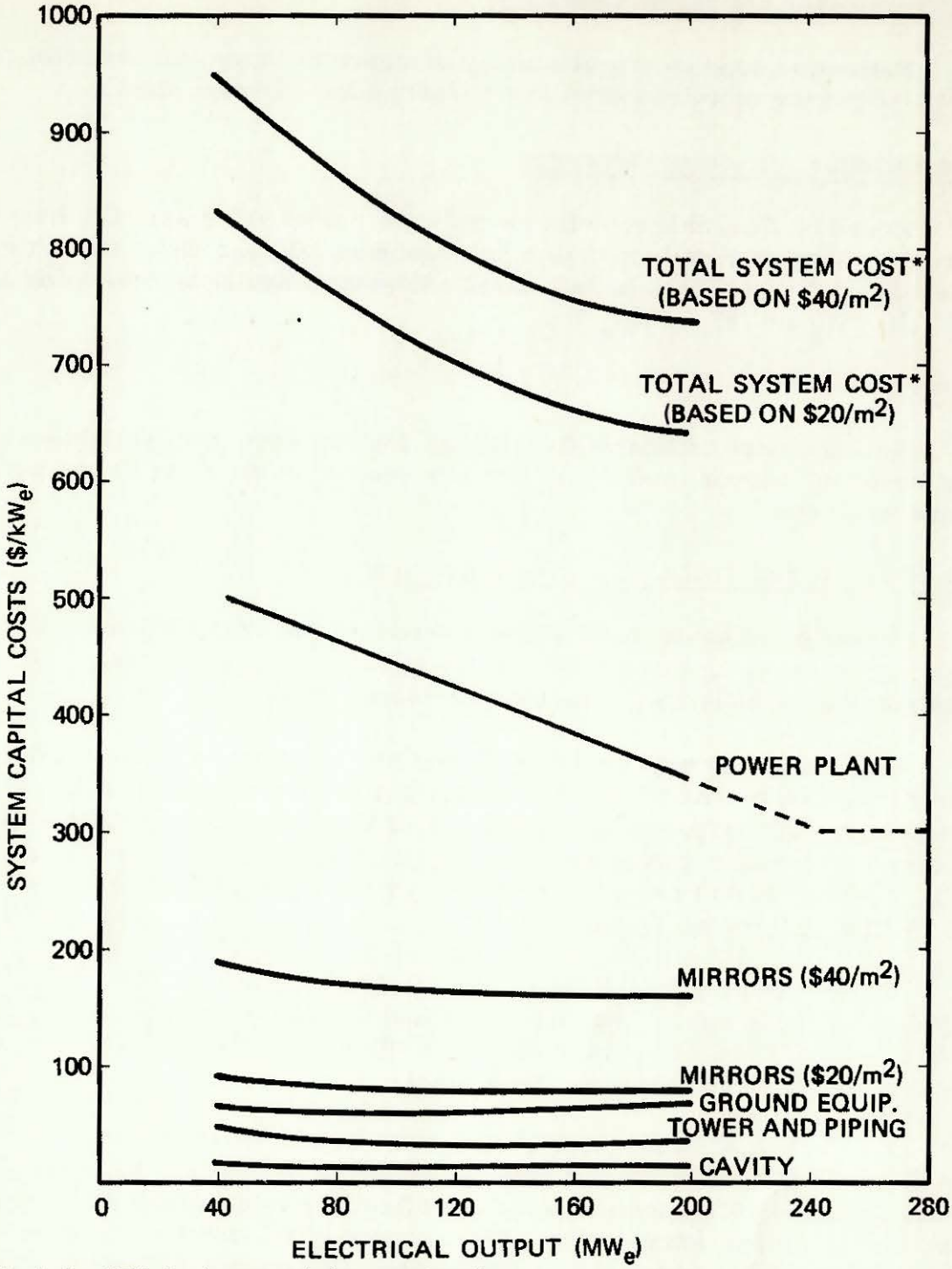

*Includes 15% for interest during construction.

Figure 8-3. Solar Electric Capital Cost Versus Electrical Capacity, 454°C Steam

Heat Exchanger and Steam Generator

Estimate based on a preliminary design with labor and material costs of $10/pound for stainless steel and $5/pound for common steel.

Tanks (Buffer, Drain and Storage)

Based on SLL characteristics and cost model using sensible heat of Hitec operating in a thermocline mode* between 504 and 198 C in insulated, above-ground, non-pressurized, stainless steel tanks at an estimated cost of $9.20/kW$_e$-hr ($3.86/kW$_t$-hr).

Mirrors

Reliable cost estimates for mirror designs were not available so a cost based on mirror modules at $20 per square meter and $40 per square meter was used.

Power House and Auxiliary Firing Equipment

Power plant costs were initially estimated at $500/kW$_e$ for a 43-MW$_e$ capacity, decreasing linearly to a value of $300/kW$_e$ at 250 MW$_e$. A constant cost of $300/kW$_e$ was used for larger sizes.

Because of the high cost of small power plants (see Table 8-1), a power plant fed by one tower is probably not economic unless that tower produces enough output for at least a 250-MW$_e$ plant. It is probably more economic to feed the output from two or more towers into a central generating station. In this case, additional piping and pumps were estimated at 2.5 million dollars per tower.

Hybrid power plant efficiency was initially estimated to be 36 percent in the solar mode and 31 percent in the fossil mode based on steam conditions of 454 C (950°F) and 800 psi for plants of 100 and 150 MW$_e$. The solar mode has the advantage of having no stack losses.

As a result of subsequent design studies, it appeared that steam conditions of 494 C (922°F) and 3500 psi could be achieved, Accordingly, Sandia adjusted efficiencies upward to reflect these higher quality conditions using the same percentage of an ideal Rankine efficiency for a regenerative reheat cycle. This resulted in an estimated efficiency of 42 percent for solar and 36 percent for fossil. The equipment for such a cycle would be more expensive so power plant costs were adjusted upwards by 10 percent to $330/kW$_e$ for capacities of 250 MW$_e$ and above. For comparison purposes the same cycle, steam conditions and power plant cost, with a slightly higher efficiency (37 percent), was used for new fossil plants.

---

*This mode of operation is described in more detail in "Sensible Heat Storage in Liquids," T. D. Brumleve, Sandia Laboratories, SLL-73-0263, July 1974.

Capitalization

Selection of the capitalization rate has a large impact on system economics economics because a solar system is very capital intensive compared to a standard power plant. In this economic analysis, a capitalization rate of 15 percent was selected and applied to both systems. The capitalization rate is assumed to cover the expenses of debt retirement and production expenses except for fuel costs. Maintenance is expected to be slightly higher on a solar power plant.

Parameters used for the remainder of the economic analysis are summarized in Table 8-2.

Plant Utilization

In order to compute the cost of electrical output, Use Factor (also known as plant factor) was used to account for periods when the electrical operating plant is being utilized at less than full rated capacity. Use Factor is the annual net electrical output divided by the possible output at nameplate capacity. It accounts for scheduled and unscheduled downtime and lack of demand. National average Use Factor is approximately 55%. Use Factor has been computed using Mission Factor, Need Factor, Heat Factor, and Electrical Factor.

The assumptions used for the factors are as follows:

Mission Factor--Mission factor accounts for demand which is less than full rated capacity. A base-load plant was assumed to have a average mission factor of 95% of nameplate capacity for 24 hours a day, 365 days a year. For the intermediate load cases, mission factor was assumed to be 67% of nameplate capacity for 24 hours a day, 365 days a year. This load was assumed to correspond to daylight hours to the extent that about six hours of storage would be required to obtain 16 hours of run time at nameplate capacity on a cloudless summer day. Peaking plant calculations were not done because solar electric power plants are capital intensive.

Need Factor--Need Factor is used to take into account the fact that not all of the capacity is required to meet the demand and that solar input will be used in preference to fossil fuel. The plant is assumed to be designed to match the demand such that no solar energy is intentionally discarded. Need Factor for solar is 1.0, with fossil fuel used to make up the difference to meet the demand.

TABLE 8-2

POWER PLANT COST ESTIMATION PARAMETERS

Hybrid Plant	
Power Plant Cost $379/kW (includes 15% interest during construction)	
Thermal Efficiency	36% Fossil Mode 42% Solar Mode
Supercritical Cycle	
Maximum Steam Temperature	494°C (922°F)
Maximum Steam Pressure	24.1 MPa (3500 psi)
One Reheat to 494°C	
Regeneration Cycle Heating Feedwater to 150°C	
Pure Fossil Plant	
Power Plant Cost $379/kW	
Thermal Efficiency	37%
Capitalization 15%/Year	
Solar Input Energy to Steam Boiler per Tower (Baseline System)	6.87×10^8 $kW_t h/Yr$
Solar Peak Power Input to Steam Boiler Per Tower Assumed to be:	300 MW_t
Location of Plant	Albuquerque, N. M.

Note: All Plants Configured for Nominal 1000 MW_e

Heat Factor--Heat Factor takes into account the unavailability of the Hitec heating system when it is needed. It is assumed to be 0.93 for fossil and 0.97 for solar. The solar is assumed to be higher since there are no shutdowns for tube burnout, pollution equipment problems, and other problems associated with burning fuel. In addition, about 16 hours a day are available for maintenance on the solar collection system with no significant loss of energy.

Electrical Factor--The Electrical Factor is used to account for the time that the turbine, generator, condenser system may not be available. It is assumed to be 0.94 for fossil and for solar without thermal storage. A higher factor 0.96 is used for solar with storage to account for the lower probability that solar energy would be wasted with loss of the electrical load.

Operating Modes

Figure 8-4 illustrates the effect of demand patterns and power plant configurations. Table 8-3 lists the formulas and symbols used for the cost estimation and Use Factor calculations. The actual factors used are not based on specific data but an attempt was made to keep the overall values consistent with the Use Factors reported by the Federal Power Commission and other sources.

Cost Comparisons

Tables 8-4 and Figure 8-5 show the cost comparisons for the base-load assumptions. Tables 8-5 and Figure 8-6 are cost comparisons for the Intermediate Load assumptions. In addition, Case IX is shown for comparative purposes. It is a pure solar plant with no storage and essentially would compete with fuel costs only (shown as Case V_F) if zero capacity displacement is assumed.

Note that all of the solar systems cross their fossil counterpart in the range of $1.45 to $2.60/MBtu. Furthermore, because some of the systems diverge slowly on either side of the crossover, bus bar energy costs are not greatly different at fuel costs substantially below the crossover points. For example, note that energy produced by the hybrid systems with no thermal storage (Cases II and VI) is only about 8 to 21 percent higher at a fuel cost of $1.00/MBtu.

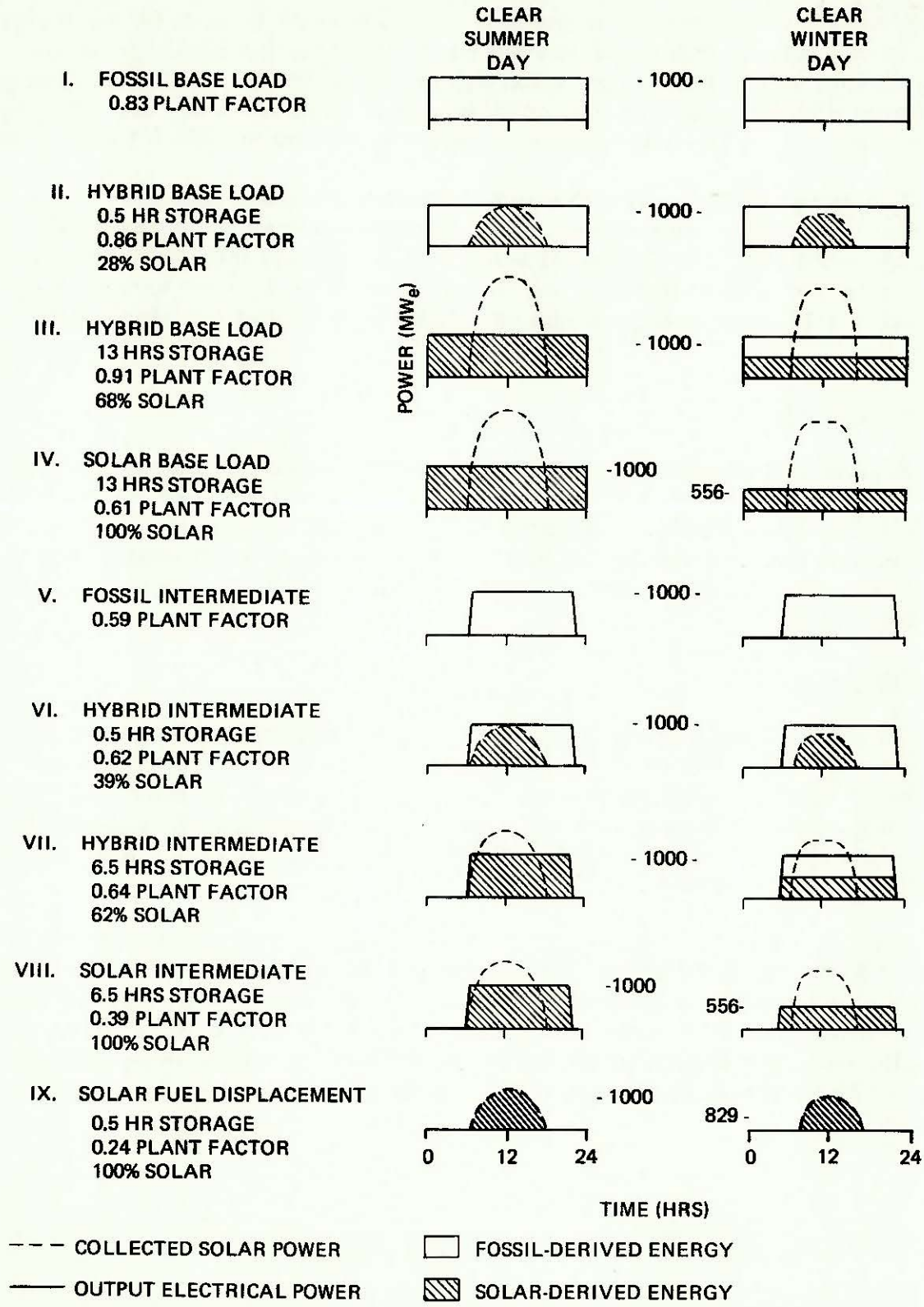

Figure 8-4. Power Plant Operating Modes

TABLE 8-3

COST ESTIMATION FORMULAS AND SYMBOLS

Q = thermal efficiency = 0.37 for fossil plant, 0.36 for hybrid

C = name plate capacity MW_e

P = possible energy, $MW_e h/Yr$

M = mission factor

base load = 0.95

intermediate load = 0.67

fuel displacement = 1.00

D = desired average annual capacity, $MW_e h/Yr$

A = available annual energy, $MW_e h/Yr$

N = need factor

H = heat factor

E = electrical factor

T = total annual energy, $MW_e h/Yr$

B = Btu of fossil fuel energy used annually, Btu/Yr

U = use factor (or plant factor)

I = individual electrical plant size, $MW_e h$

= no. of solar towers

$ = cost in dollars/kilowatt - fossil plant

$20 = cost in dollars/kilowatt - solar plant with $\$20/m^2$ mirrors

$40 = cost in dollars/kilowatt - solar plant with $\$40/m^2$ mirrors

% = percent of total output from solar

Subscripts S for Solar
F for Fossil

$P = C * 24 * 365$

$D = M * P$

$T_S = A_S * N_S * H_S * E_S$

$D_F = D - T_S$

$N_F \quad D_F/P$

$T_F = A_F * N_F * H_F * E_F$

$B = T_F * 3.4\ 13E6/Q$

$U = T/P$

$\% = T_S * 100/T$

TABLE 8-4

BASELOAD PARAMETERS

	Symbol	Case I	Case II	Case III	Case IV
Name Plate Capacity, MW_e	C	1000	1000	1000	1000
Possible Output, $MW_e h$	P	8.76E6	8.76E6	8.76E6	8.76E6
Mission Factor	M	0.95	0.95	0.95	0.95
Desired Output, $MW_e h$	D	8.32E6	8.32E6	8.32E6	8.32E6
Available Solar, $MW_e h$	A_S	--	2.31E6	5.77E6	5.77E6
Need Factor	N_S	--	1.00	1.00	1.00
Heat Factor	H_S	--	0.97	0.97	0.97
Electrical Factor	E_S	--	0.94	0.96	0.96
Total Solar-Derived, $MW_e h$	T_S	--	2.11E6	5.37E6	5.37E6
Desired Fossil, $MW_e h$	D_F	8.32E6	6.21E6	2.95E6	--
Need Factor	N_F	0.95	0.709	0.326	--
Heat Factor	H_F	0.93	0.93	0.93	--
Electrical Factor	E_F	0.94	0.94	0.94	--
Available Fossil, $MW_e h$	A_F	8.76E6	8.76E6	8.76E6	--
Total Fossil-Derived, $MW_e h$	T_F	7.27E6	5.43E6	2.58E6	--
Total Fuel, Btu	B	6.71E13	5.00E13	2.38E13	--
Total Output, $MW_e h$	T	7.27E6	7.54E6	7.95E6	5.37E6
Plant Factor	U	0.830	0.861	0.907	0.613
Individual Plant, MW_e	I	1000	500	250	250
No. Solar Towers	#	0	8	20	20
System Cost, $\$/kW_e$	$	379	--	--	--
	$20	--	593	1081	875
	$40	--	683	1277	1071
Thermal Storage, Hrs	--	0	0	13.44	13.44
Coal Saved, Tons/Yr	--	0	1.08E6	2.75E6	2.75E6
Percent Solar	%	0	28	68	100

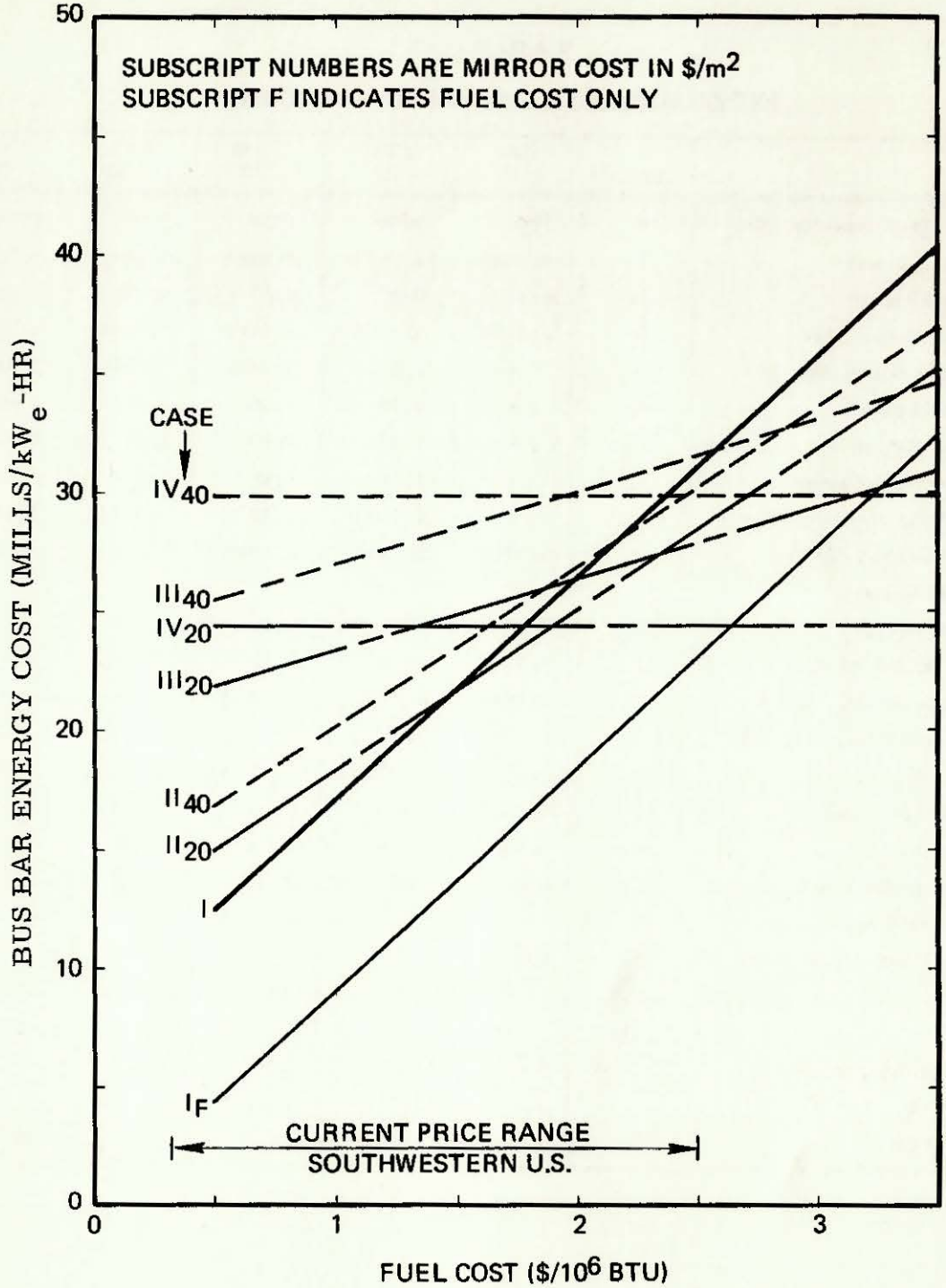

Figure 8-5. Base Load Energy Cost

TABLE 8-5

INTERMEDIATE LOAD PARAMETERS

	Symbol	Case V	Case VI	Case VII	Case VIII	Case IX
Name Plate Capacity, MW_e	C	1000	1000	1014	1014	1000
Possible Output	P	8.76E6	8.76E6	8.88E6	8.88E6	8.76E6
Mission Factor	M	0.67	0.67	0.67	0.67	1.00
Desired Output, MW_eh	D	5.87E6	5.87E6	5.95E6	5.95E6	8.76E6
Available Solar, MW_eh	A_S	--	2.31E6	3.75E6	3.75E6	2.31E6
Need Factor	N_S	--	1.00	1.00	1.00	1.00
Heat Factor	H_S	--	0.97	0.97	0.97	0.97
Electrical Factor	E_S	--	0.94	0.96	0.96	0.94
Total Solar Derived, MW_eh	T_S	--	2.11E6	3.49E6	3.49E6	2.11E6
Desired Fossil, MW_eh	D_F	5.87E6	3.76E6	2.46E6	--	--
Need Factor	N_F	0.67	0.429	0.277	--	--
Heat Factor	H_F	0.93	0.93	0.93	--	--
Electrical Factor	E_F	0.94	0.94	0.94	--	--
Available Fossil, MW_eh	A_F	8.76E6	8.76E6	8.88E6	--	--
Total Fossil Derived, MW_eh	T_F	5.13E6	3.29E6	2.15E6	--	--
Total Fuel, Btu	B	4.73E13	3.03E13	1.98E13	--	--
Total Output, MW_eh	T	5.13E6	5.40E6	5.64E6	3.49E6	2.11E6
Use Factor	U	0.586	0.616	0.635	0.393	0.241
Individual Plant, MW_e	I	1000	500	338	338	500
No. Solar Towers	#	0	8	13	13	8
System Cost, $\$/kW_e$	$	379	--	--	--	-
	$20	--	593	795	605	404
	$40	--	683	922	733	482
Thermal Storage, Hrs	--	0	0	6.5	6.5	0
Coal Saved, Tons/Yr	--	0	1.08E6	1.79E6	1.79E6	1.08E6
Percent Solar	%	0	39	62	100	100

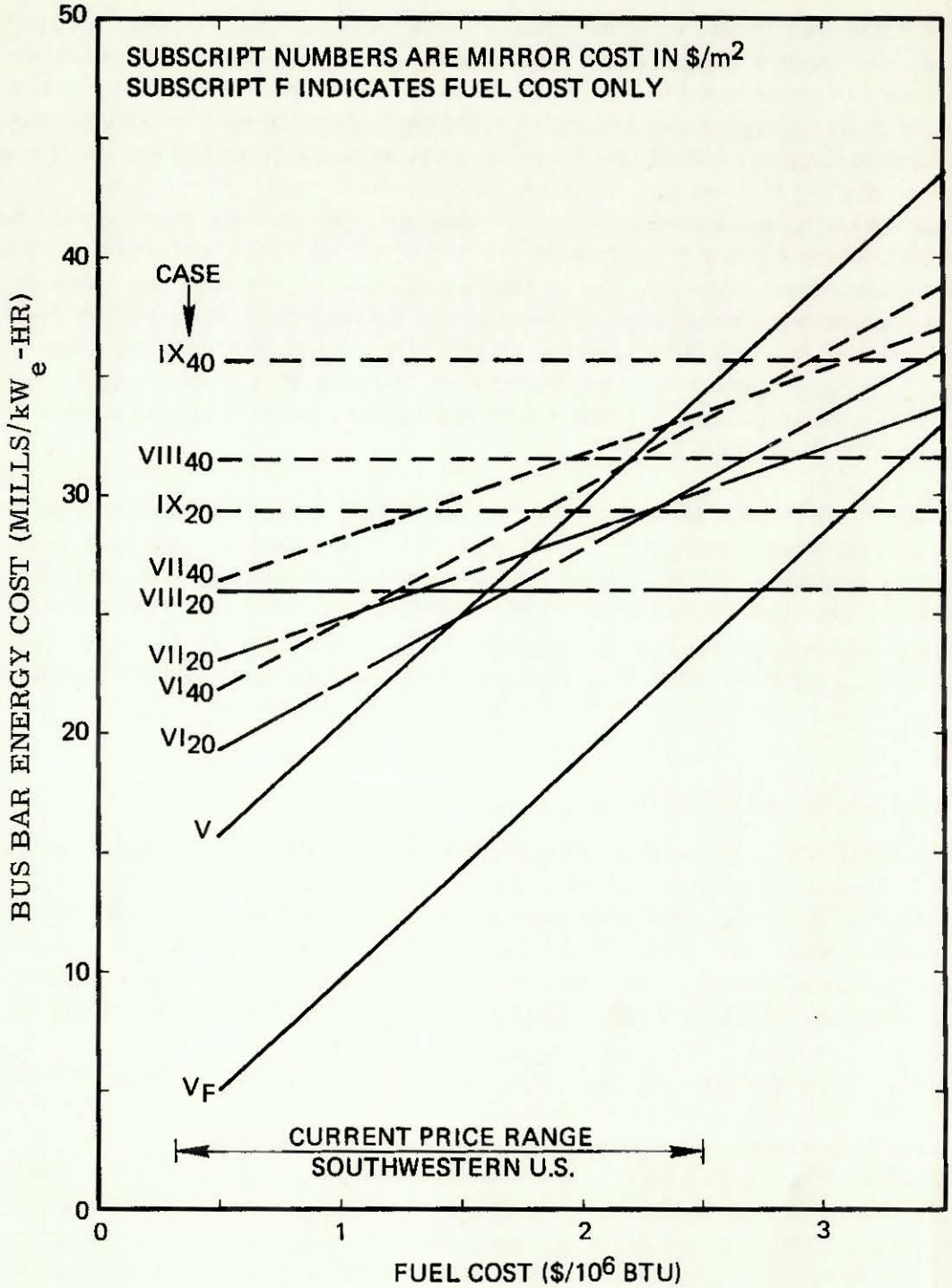

Figure 8-6. Intermediate Load Energy Cost

Sensitivity to Plant Factor

As reflected in the cost analyses, it is expected that Hybrid systems would achieve higher plant factors than their fossil counterparts because (1) incidence of unscheduled interruptions of plant output should be lower because of dual energy supplies, (2) scheduled plant downtime should also be reduced because much of the routine maintenance can be done on the solar subsystem during non-sunshine hours and on the fossil subsystem when the generator is being operated from solar energy, and (3) the plant would be operated whenever possible in the solar mode since marginal cost should be lower than fossil plants in the network. However, to test the sensitivity of this assumption, comparisons were made between the fossil base load plant and two of the hybrid systems (II and III) using equal overall plant factors. The assumption was retained that the hybrid systems would be operated whenever possible from solar energy because of the very low marginal cost in the solar mode.

The cost of bus bar energy increases in all cases as the plant factor is lowered (as shown in Figures 8-7 and 8-8). However, note that the competitive position, as indicated by the crossover fuel costs shown in Figure 8-9, changes very little. This insensitivity is due largely to the fact that, as plant factor is reduced, the fossil fuel used by the hybrid plants decreases at a greater rate than fuel used by the fossil plant; this more than compensates for the higher annual fixed charges of the hybrid plants.

Sensitivity to Cost Estimates

Preliminary sensitivity analyses were also done to explore the effects of different cost estimates for certain elements of the system on bus bar energy costs. An example is shown in Figure 8-10 for variations about nominal values of $\$40/m^2$ mirror cost and \$2/MBtu fuel cost for a hybrid base load plant (Case II). A similar plot for Case I is shown in Figure 8-11 for comparison. Note in Figure 8-10 that the cost of bus bar energy is much more sensitive to the cost of fuel, capitalization rate, and power plant cost than it is to the cost of mirrors. It is very insensitive to tower cost.

The sensitivity of the competitive position of the two plants is illustrated in Figure 8-12 for variations about the same nominal conditions assumed above. The competitive position is strongly sensitive to fuel cost and capitalization rate, moderately sensitive to mirror cost, and very insensitive to tower and power plant costs. At a fuel price of \$2/MBtu and the other nominal conditions assumed in this instance, it is interesting to note that even if mirrors cost as much as $\$80/m^2$, bus bar energy from the hybrid plant would cost only about 17 percent more than that from the fossil plant.

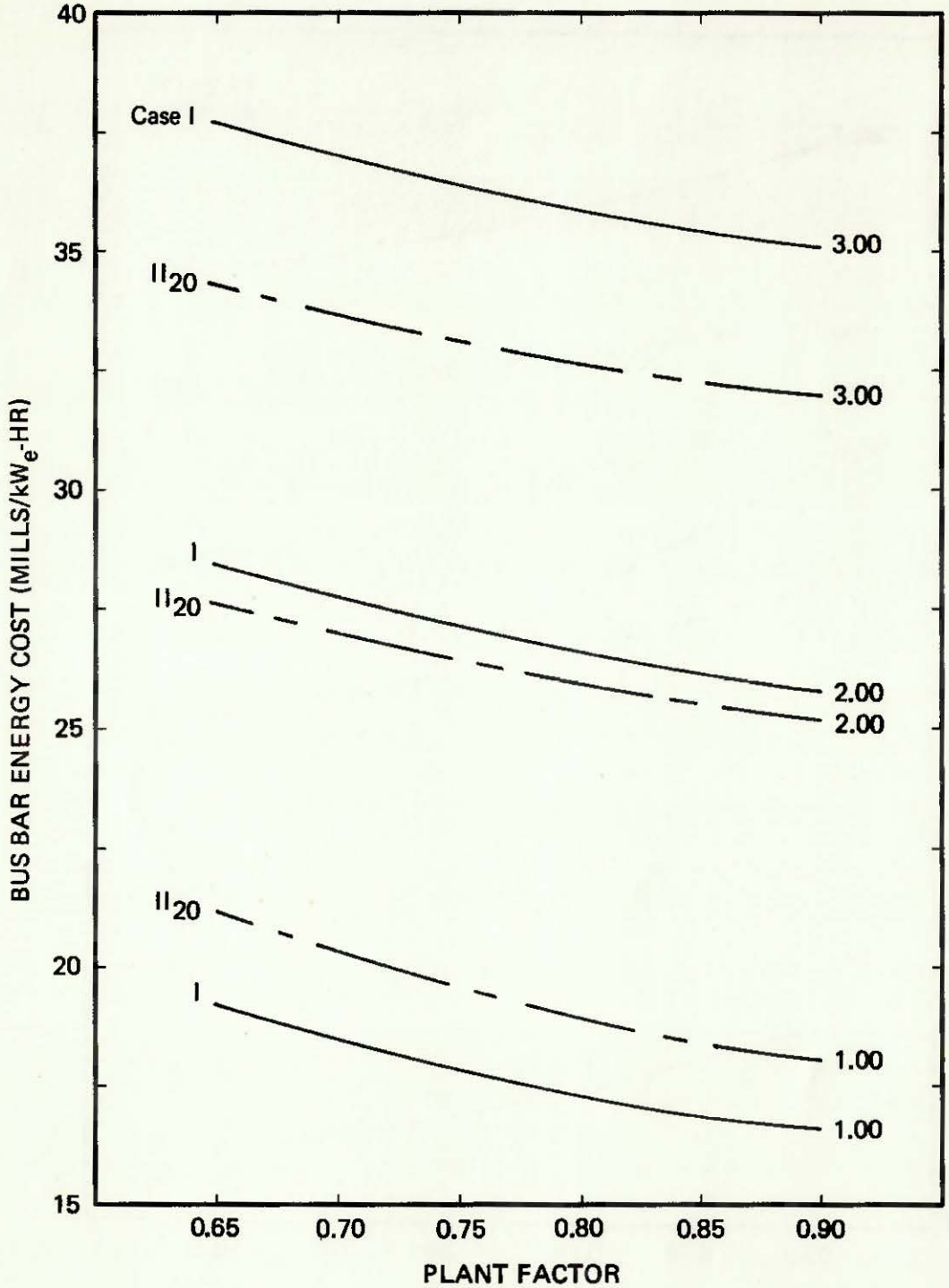

Figure 8-7. Sensitivity of Case II Bus Bar Energy Cost to Plant Factor

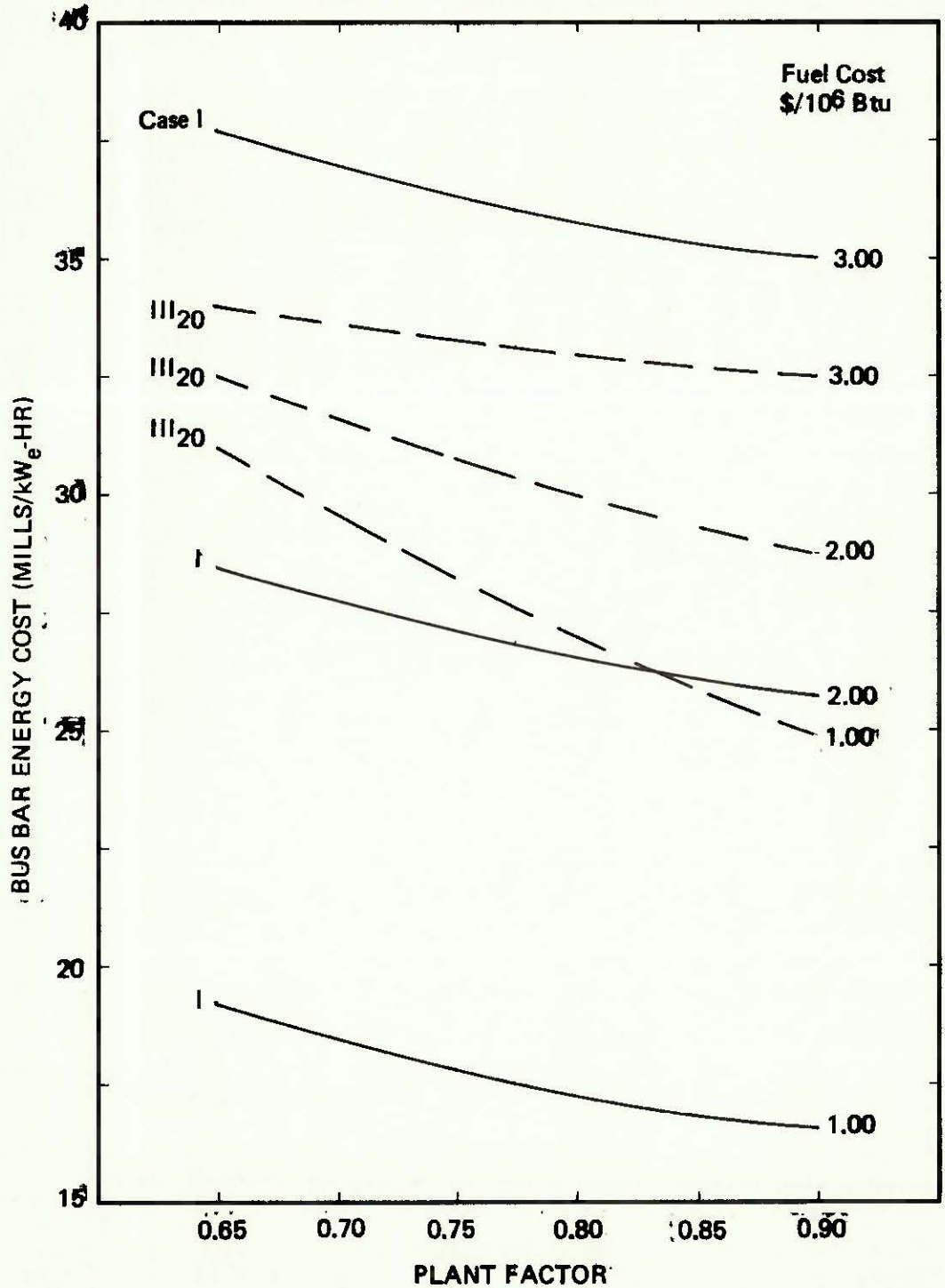

Figure 8-8. **Sensitivity of Case III Bus Bar Energy Cost to Plant Factor**

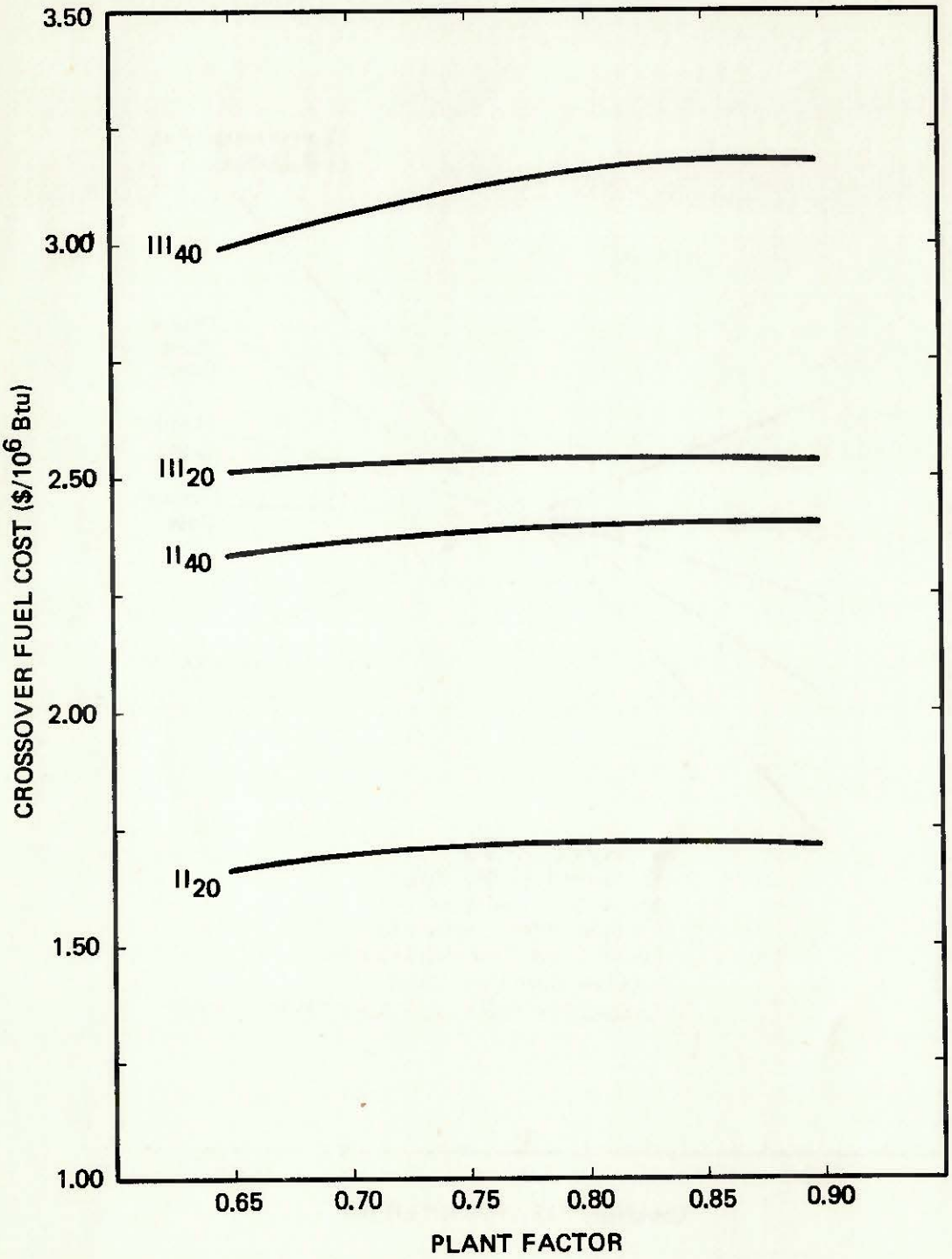

Figure 8-9. Sensitivity of Crossover Fuel Cost to Plant Factor

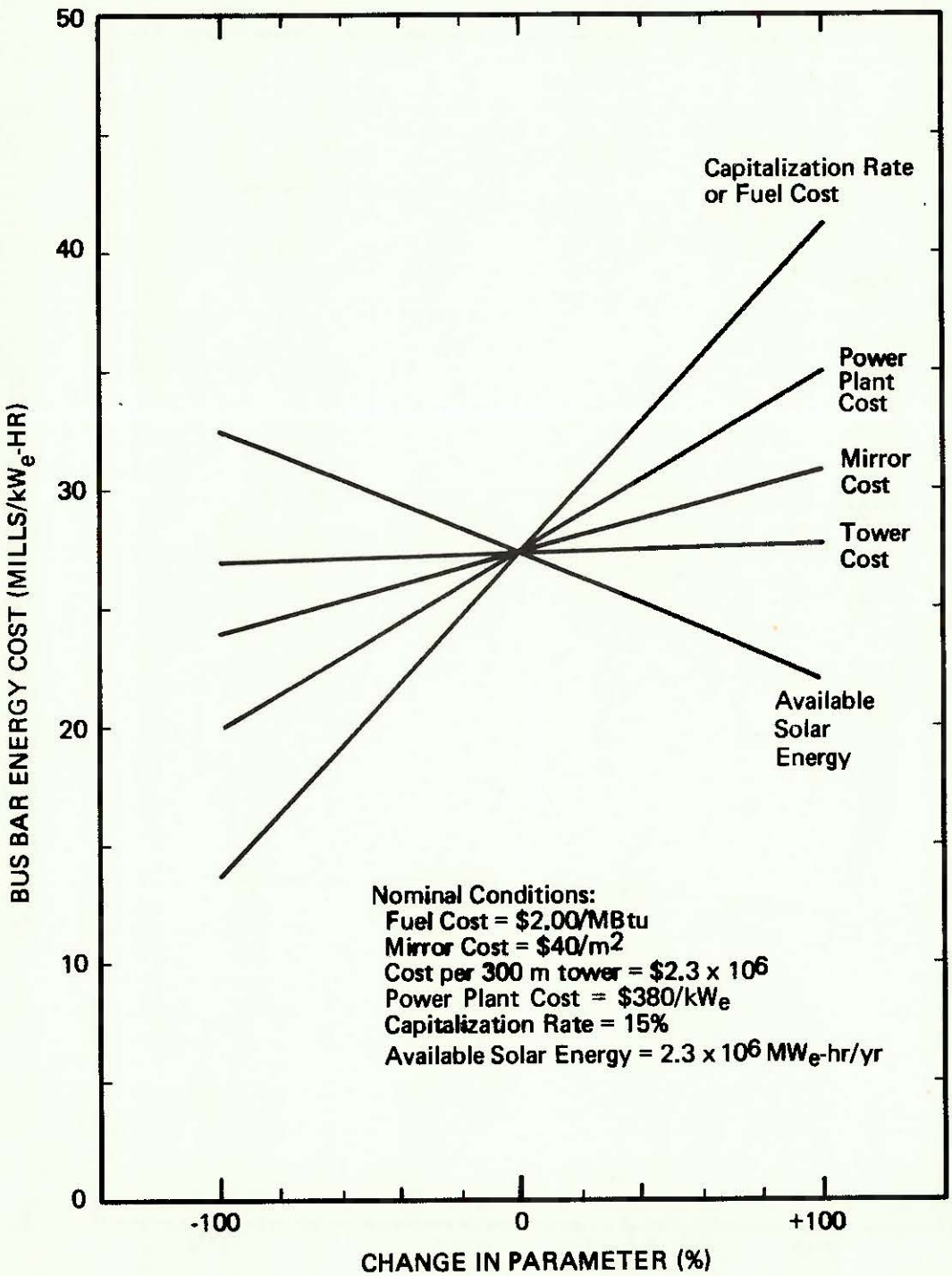

Figure 8-10. Sensitivity of Bus Bar Energy Cost to Various Parameters for Case II

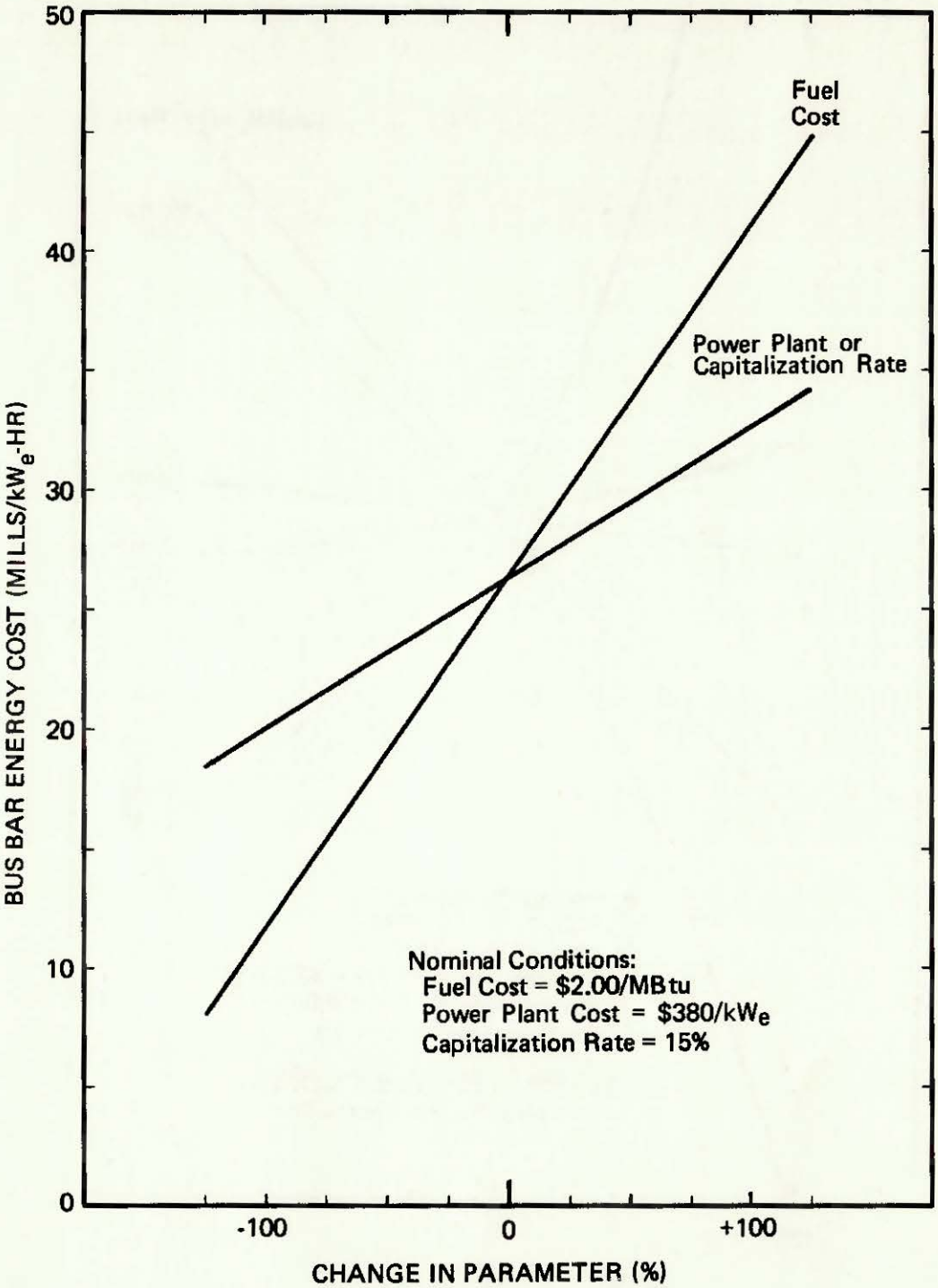

Figure 8-11. Sensitivity of Bus Bar Energy Cost to Various Parameters for Case I

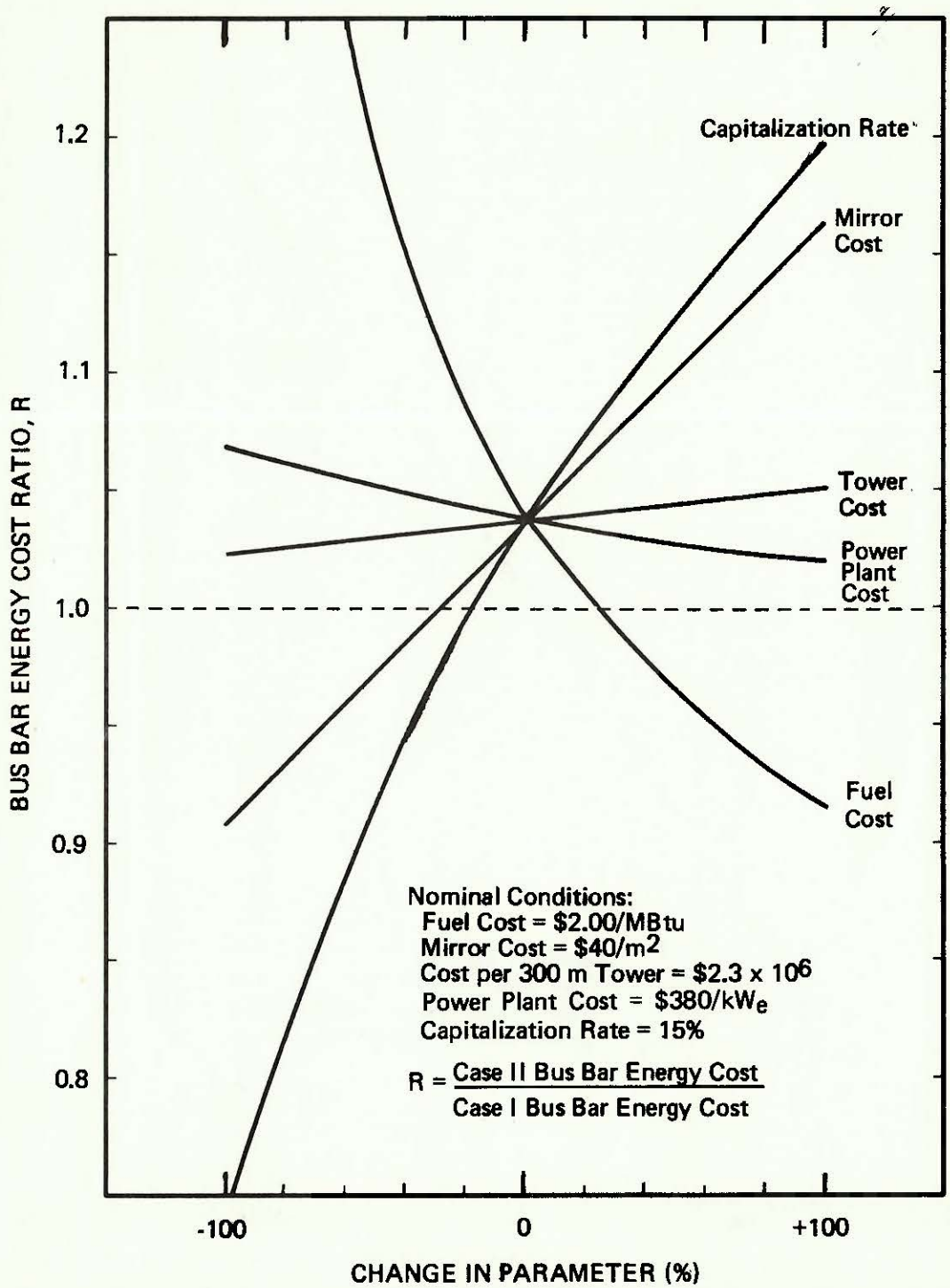

Figure 8-12. Sensitivity of Competitive Energy Costs to Various Parameters for Case II

Summary

The costs used for this study were very preliminary and represent rough approximations. The following inferences were drawn based on this preliminary study of a non-optimized system. Configurations of systems for a specific demand pattern could change the actual cost of power produced.

1. In areas of high insolation, power from solar-fossil hybrid plants (Cases II, III, VI, and VII) would be interesting at a fuel cost of $2.00 per million Btu.

2. The cost of electrical energy from hybrid solar-fossil plants with no thermal storage (Cases II and VI) would be about 10-20 percent higher than that from the fossil counterparts at a fuel cost of $1 per million Btu.

3. Solar-derived thermal energy delivered to the electrical power plant may have a capitalized cost of approximately $2 per million Btu if our assumptions are valid.

4. Solar hybrid systems with thermal storage (Cases III and VII) displace 1-1/2 to 2-1/2 times as much fuel as do hybrids without storage (Cases II and VII), and may produce cheaper bus bar energy at fuel costs above about $2.50 per million Btu.

5. A pure solar system with no thermal storage and no fossil backup has the worst comparative position of all of the systems studied.

BIBLIOGRAPHY

T. D. Brumleve, A High Temperature Solar Energy System, SAND74-8008, Sandia Laboratories, Livermore, July 1974.

T. D. Brumleve, A Solar Energy Collector System, internal working paper, June 1973.

Verbal communications with and unpublished investigations by S. W. Zehr, Thermochemical Techniques for Producing Hydrogen from Water, Sandia Laboratories, Livermore.

F. Trombe and A. Le Phat Vinh, "Thousand KW Solar Furnace Built by the National Center of Scientific Research in Odeillo, France," Solar Energy, Vol. 15, 1973.

J. R. Howell, (J. P. Hartnett and T. F. Irvin, Eds.) "Application of Monte Carlo to Heat Transfer Problems," Advances in Heat Transfer, Vol. 5, 1968.

T. D. Brumleve, Sensible Heat Storage in Liquids, SLL-73-0263, Sandia Laboratories, Livermore, July 1974.

B. F. Fisher, Cost Analysis for H_2O Sensible Heat Storage in Surface Steel Tanks, Sandia internal working paper, December 1972.

Some Results on Solar Thermal Systems Studies, SLA-73-5037, Sandia Laboratories, January 1973.

An Analysis of Linear Focused Collectors for Solar Power, SLA-73-5319A, Sandia Laboratories, August 1973.

A Vector Analysis of the Solar Energy Reflection and Collection Process, SLA-73-5300, Sandia Laboratories, October 1973.

A Solar Community, SC-M-72-0794, Sandia Laboratories, November 1972.

F. Trombe, L. Gion, C. Royere and J. Francois Robert, "First Results Obtained with the 1000 KW Solar Furnace," Solar Energy, Vol. 15, 1973.

R. Segel and J. R. Howell, Thermal Radiation Heat Transfer, McGraw-Hill, 1972.

B. Y. H. Liu and R. C. Jordan, "The Interrelationship of Characteristic Distribution of Direct, Diffuse, and Total Solar Radiation," Solar Energy, Vol. 4, Number 3, 1960, pp. 1-19.

Environmental Science Services Administration, Climatic Atlas of the United States, Environmental Data Service, U. S. Govt. Printing Office, June 1968.

A. P. Bradford and G. Hass, "Solar Reflectance of Unprotected Aluminum Front-Surface Mirrors," Solar Energy, Vol. 9, No. 1, 1965.

Perry, Chilton, Kirkpatrick, Perry's Chemical Engineers Handbook, McGraw-Hill, Fifth Edition, 1973.

Solar Thermal Power Systems Based on Optical Transmission, Univ. of Houston, McDonnell Douglas, NSF/RANN/SE/G1-39456/PR/73/4.

Solar Thermal Conversion Mission Analysis, Aerospace Corporation, Report to NSF ATR-74(7417-05)-1.

Steam-Electric Plant Construction Cost and Annual Production Expenses, 24th Annual Supplement - 1971, Federal Power Commission.

F. Kreith, Principals of Heat Transfer, Intex Press, Inc., Third Edition, 1973.

G. Ya. Umarov, "Problems of Solar Energy Concentration," Geliotekhnika, Vol. 3, No. 5, pp. 32-51, 1967.

H. Everett III, "Generalized Lagrange Multiplier Method for Solving Problems of Optimum Allocation of Resources," Operations Research, 11, 401, 1963.

B. J. Garnier and Atsumu Ohmura, "Evaluation of Surface Variations in Solar Radiation Income," Solar Energy, 13, 22, April 1970.

Manual of Steel Construction, AISC, 7th Edition, 1970.

Wind Forces on Structures, Final Report, Paper No. 3269, ASCE.

E. Cohen and H. Perrin, Design of Multi-Level Guyed Towers: Wind Loading, Proc. Paper No. 1355, ASCE.

E. Cohen and H. Perrin, Design of Multi-Level Guyed Towers: Structural Analysis, Proc. Paper No. 1356, ASCE.

F. H. Hall, Stability Analysis of Multi-Level Guyed Towers, J. Struct. Div. Proc., ASCE Paper No. 3091.

P. Sachs, Wind Forces in Engineering, Pergamon Press, 1972, Chapter 8.

C. W. Stephans, A. M. Haire, "Internal Design Consideration for Cavity-Type Solar Absorbers," ARS Journal, pp. 896-901, July 1961.

V. A. Grilikhes, F. V. Obtemperanskii, "Analysis of Radiative Heat Exchange Processes in Cylindrical Cavity-Type Collectors of Solar Power Plants," Appl. Solar Energy, 5, No. 1-2, pp. 59-65 (1969).

F. V. Obtemperanskii, V. A. Grilikhes, "Approximate Thermal Calculations for Cylindrical Cavity-Type Collectors with Liquid-Metal Heat-Transport Medium," Appl. Solar Energy, 5, No. 3-4, pp. 61-65 (1969).

E. M. Sparrow, R. D. Cess, Radiation Heat Transfer, pp. 163-170, Brooks/Cole Publishing Co., Belmont, CA (1967).

E. M. Sparrow, V. K. Jonsson, "Absorption and Emission Characteristics of Diffuse Spherical Enclosures," Trans. ASME, J. Heat Transfer, C 84, pp. 188-189 (1962).

J. P. Holman, Heat Transfer, Second Edition, McGraw-Hill, New York (1968).

S. M. Selby, Editor, Standard Mathematical Tables, Nineteenth Edition, p. 106, The Chemical Rubber Co., Cleveland (1971).

B. R. Sundheim and J. Greenberg, Rev. Sci. Instru., 27(9), 703 (1956).

B. J. Brough and D. H. Kerridge, J. Chem. and Eng. Data, 11 (2), 260 (1966).

S. V. Volkov and N. I. Buryak, Russ. J. Inorg. Chem., 17 (1), 93 (1972).

W. H. McCulloch, D. O. Lee, W. P. Schimmel, Jr., The Solar Community--Energy for Residential Heating, Cooling, and Electric Power, SLA-74-0091, Sandia Laboratories, Albuquerque, February 1974.

W. P. Schimmel, Jr., The Solar Incidence Factor and Other Geometric Considerations of Solar Energy Collection, SAND74-0026, Sandia Laboratories, Albuquerque, July 1974.

F. A. Blake, Solar/Hydroelectric Combined Power Systems, presentation to American Association for the Advancement of Science Annual Meeting San Francisco, February 26, 1974.

F. A. Blake, Solar Power Conversion System and Applications, presentation to Western Systems Coordinating Council, Albuquerque, New Mexico, September 24 and 25, 1973.

T. Bramlette, C. A. Tarne and R. A. Milby, Solar Energy Storage Systems, RS 8184/41, Sandia Laboratories, Livermore, May 1974.

T. D. Brumleve, Prospects for Solar Energy Utilization, SAND74-8604, Sandia Laboratories, Livermore, June 1974.

R. B. Pope and W. P. Schimmel, Jr., The Solar Community and the Cascaded Energy Concept Applied to a Single House and a Small Subdivision - A Status Report, SLA-73-0357, Sandia Laboratories, Albuquerque, May 1973.

F. D. Newman and D. K. Snediker, The Properties of Potential Low-Cost Heat-Transfer Fluids, FAO 92-6184, Battelle, Columbus Laboratories, March 15, 1974.

R. O. Sundahl and J. C. Miller, Temperature Boosting and Energy Storage by Heat of Dilution, SLL-74-0224, Sandia Laboratories, Livermore, May 1974.

T. D. Brumleve, A High Temperature Solar Energy System, SLL-73-0059, Sandia Laboratories, Livermore, August 1973.

University of Houston and McDonnell Douglas Astronautics Company, Solar Thermal Power Systems Based on Optical Transmission, Report NSF/RANN/SE/GI-39456/PR/73/4, February 15, 1974.

The Aerospace Corporation, El Segundo, California, Solar Thermal Conversion Mission Analysis, Report No. ATR-74(7417-05)-1, January 1974.

University of Minnesota and Honeywell, Research Applied to Solar-Thermal Power Systems, Report: NSF/RANN/SE/GI-34871/PR/72/4, (Covering the period July 1, 1972 to December 31, 1972) Initiated July 1, 1972.

University of Minnesota and Honeywell, Research Applied to Solar-Thermal Power Systems, Report NSF/RANN/SE/GI-34871/PR/73/4, (Covering the period July 1 to December 31, 1973), January 31, 1974.

University of Minnesota and Honeywell, Research Applied to Solar-Thermal Power Systems, Report: NSF/RANN/SE/GI-34871/PR/73/2, (Covering the period January 1 to June 30, 1973), July 31, 1973.

R. W. Palm, Selecting Preferred Sites for a Solar Power Station Using Solar/Climatic Data, Honeywell Inc., October 1973.

G. T. Schjeldahl Company, Solar Power Array for the Concentration of Energy, March 13, 1974.

Honeywell Systems and Research Center, Dynamic Conversion of Solar Generated Heat to Electricity, Report No. F3403-PR5 2852-41404 (Covering the period December 31, 1973 through February 3, 1974) February 13, 1974.

Honeywell Systems and Research Center, Dynamic Conversion of Solar Generated Heat to Electricity, Report No. F3403-PR6 2852-41410, (Covering the period February 4, 1974 to March 3, 1974), March 15, 1974.

Honeywell Systems and Research Center, Dynamic Conversion of Solar Generated Heat to Electricity, Report No. F3403-PR7 2852-41412 (Covering period of March 4, 1974 through March 31, 1974),April 15, 1974.

J. M. Hammer, et al., Honeywell, and J. C. Grosskreutz et al., Black and Veatch, Dynamic Conversion of Solar Generated Heat to Electricity, Report No. F3403-PR8, (Covering the period April 1, 1974 through May 5, 1974) May 15, 1974.

L. C. Fuller, C. A. Sweet, H. I. Bowers, ORCOST - A Computer Code for Summary Capital Cost Estimates of Steam-Electric Power Plants, Oak Ridge National Laboratory ORNL-TM-3743, September 1972.

H. I. Bowers, L. D. Reynolds, R. C. DeLozier, B. E. Srite, Concept - Computerized Conceptual Cost Estimates for Steam-Electric Power Plants, Oak Ridge National Laboratory ORNL-4809, April 1973.

United Engineers and Constructors Inc., Volume 1 Pressurized Water Reactor Plant, 1000-MWE Central Station Power Plants Investment Cost Study, June 1972.

E. G. Bohlmann, Heat Transfer Salt for High Temperature Steam Generation, Oak Ridge National Laboratory, ORNL-TM-3777, December 1972.

E. I. du Pont de Nemours & Co. Inc., Du Pont Hitec Heat Transfer Salt, Chemical Products Sales Division, Explosives Department

UNLIMITED RELEASE - PATENT CAUTION

INITIAL DISTRIBUTION:

Dr. Edward H. Fleming, Jr.
Maj. Gen. Ernest Graves
Dr. Jack Vanderryn
Dr. James C. Bresee
Mr. James E. Rannels (10)
U. S. Atomic Energy Commission
Washington, D. C. 20545

Dr. Donald B. Beattie
Dr. Lloyd O. Herwig
Mr. George Kaplan (7)
National Science Foundation
1800 G. Street
Washington, D. C. 20550

Mr. Dean Graves
D. K. Nowlin
J. R. Cotton
D. W. King
U. S. Atomic Energy Commission
Albuquerque Operations Office
P. O. Box 5400
Albuquerque, New Mexico 87115

Prof. Vernon Albertson
University of Minnesota
Department of Electrical Engineering
Minneapolis, Minnesota 55455

Dr. D. E. Anderson
Mr. Ross A. Stickley
Sheldahl, Inc.
Northfield, Minnesota 55057

Dr. Roderick E. Athey
Mr. Charles Grosskreutz
Black and Veatch
1500 Meadow Lake Parkway
Kansas City, Missouri 64114

Dr. Charles E. Backus
College of Engineering
Arizona State University
Tempe, Arizona 85231

Dr. Douglas Balcomb
Los Alamos Scientific Laboratory
Los Alamos, New Mexico 87544

Dr. Richard Balzhizer
Mr. Dwain Spencer
Electric Power Research Institute
3412 Hillview Avenue
Palo Alto, California 94304

Dr. Charles D. Beach
1515 Mariposa Ave.
Boulder, Colorado 80302

Mr. John E. Bigger
Department of Water & Power
City of Los Angeles
111 No. Hope St.
Los Angeles, Calif. 90025

Mr. Floyd A. Blake
Martin Marietta Aerospace
P. O. Box 179
Denver, Colorado 80122

Mr. John Blewett,
Attn. J. G. Cottingham
Brookhaven National Laboratory
Upton, L. I., New York 11973

Mr. Piet B. Bos
Aerospace Corporation
P. O. Box 92957
Los Angeles, California 90045

Mr. G. W. Braun
Southern California Edison
2244 Walnut Grove Ave.
Rosemead, Calif. 91770

Mr. Elton Buel
Director R&D
Arizona Public Service Co
P. O. Box 21666
Phoenix, Arizona 85036

Dr. John Cummings
ITEK Corporation
10 McGuire Road
Lexington, Massachusetts

Dr. Jesse C. Denton
National Center for Mgt.
University of Pennsylvani
Philadelphia, Pennsylvani

Dr. William Dickinson
Lawrence Livermore Lab
Livermore, California 94

Mr. Kirk Drumheller
Battelle Pacific Northwest
P. O. Box 999
Richland, Washington 993

Dr. John A. Duffie
Director, Solar Energy L
University of Wisconsin
1500 Johnson Drive
Madison, Wisconsin 5370

Dr. S. D. Elliott, Jr.
Code 60223
Naval Weapons Center
China Lake, California 9

Mr. Louis O. Elsaesser
Director of Research
Edison Electric Institute
90 Park Avenue
New Yor, New York 1001

Prof. E. A. Farber
Solar Energy & Energy C
University of Florida
Gainsville, Florida 3261

Mr. Elton Buel
Director R&D
Arizona Public Service Company
P. O. Box 21666
Phoenix, Arizona 85036

Dr. John Cummings
ITEK Corporation
10 McGuire Road
Lexington, Massachusetts 02173

Dr. Jesse C. Denton
National Center for Mgt. & Power
University of Pennsylvania
Philadelphia, Pennsylvania 19104

Dr. William Dickinson
Lawrence Livermore Laboratory
Livermore, California 94550

Mr. Kirk Drumheller
Battelle Pacific Northwest Laboratory
P. O. Box 999
Richland, Washington 99352

Dr. John A. Duffie
Director, Solar Energy Laboratory
University of Wisconsin
1500 Johnson Drive
Madison, Wisconsin 53706

Dr. S. D. Elliott, Jr.
Code 60223
Naval Weapons Center
China Lake, California 93555

Mr. Louis O. Elsaesser
Director of Research
Edison Electric Institute
90 Park Avenue
New Yor, New York 10016

Prof. E. A. Farber
Solar Energy & Energy Conversion Laboratory
University of Florida
Gainsville, Florida 32611

Dr. Peter E. Glaser
Arthur D. Little, Inc.
Acorn Park
Cambridge, Massachusetts 02140

Dr. S. William Gouse, Jr.
Director of Energy R&D
Department of the Interior
Washington, D.C. 20240

Mr. Richard S. Greeley
Mitre Corporation
1820 Dolley Madison Blvd.
McLean, Virginia 22101

Mr. Ray Hallet
Mr. C. R. Easton
McDonnel Douglas
5301 Balsa Ave.
Huntington Beach, California

Dr. Alvin F. Hildebrandt
Dr. Loren L. Vant Hull
Department of Physics
University of Houston
3801 Cullen Boulevard
Houston, Texas 77004

Mr. Peter Hindley
Pacific Gas & Electric
77 Beale Street
San Francisco, California

Mr. Sig Hansen
Mr. Les Hill
State of California
Energy Planning Council
1127 L Street
Sacramento, California

Dr. Richard Hill
Federal Power Commission
441 G Street, N.W. - Room 4005
Washington, D.C. 20426

Mr. Wallace B. Huffman
Bonneville Power Administration
P. O. Box 3621
Portland, Ore. 97208

Mr. Russ Humphreys
Salt River Project
P. O. Box 1980
Phoenix, Ariz.

James Johnson, Jr.
Oak Ridge National Laboratory
Oak Ridge, Tennessee 37830

Dr. S. Karaki
Department of Civil Engineering
Engineering Research Center
Colorado State University
Fort Collins, Colorado 80521

Mr. Ed Kist
Public Service of New Mexico
P. O. Box 2267
Albuquerque, New Mexico 87103

Mr. Ron Larson
Congress of the United States
Office of Technology Assessment
Washington, D.C. 20501

Dr. George Löf
158 Fillmore Street
Suite 204
Denver, Colorado 80206

Mr. John Martin
Argonne National Laboratory
Argonne, Illinois 60439

Prof. Aden B. Meinel
Optical Sciences Center
University of Arizona
Tucson, Arizona 85721

Mr. Russ Miner
Pacific Gas & Electric
Department of Engineering Research
3400 Crow Canyon Road
San Ramon, California 94583

Dr. Frederick H. Morse
College of Engineering
University of Maryland
College Park, Maryland 20472

Mr. M. C. Noland
Midwest Research Institute
425 Volker
Kansas City, Missouri 64114

Mr. Jerry Powell
Mr. R. N. Schmidt
Honeywell Systems & Research Center
2600 Ridgeway Parkway
Minneapolis, Minnesota 55413

Mr. Mel Simmons
Mr. Michael Wahlig
Lawrence Berkeley Laboratory
Berkeley, California 94720

Mr. Terry E. Walsh
Ernest Y. Lam
Scientific Development
Bechtel Corporation
50 Beal Street
San Francisco, California 94119

Mr. J. D. Walton
Chief, High Temperature Materials Division
Engineering Experiment Station
Georgia Institute of Technology
Atlanta, Georgia 30332

Dr. Alvin M. Weinberg, Director
Office of Energy R&D
Federal Energy Administration
4025 NEOB
17th and Pennsylvania
Washington, D. C. 20461

Dr. Jerome Weingart
Associate of the Center for Government Education Relations
1755 Massachusetts Avenue, N. W.
Washington, D. C. 20036

Mr. Robert J. Zoschak
Foster Wheeler Corporation
110 South Orange Avenue
Livingston, N. J. 07039

M. Sparks, 1
W. J. Howard, 2
C. Winter, 4010
H. G. Pierce, 4140
D. B. Shuster, 4700
A. Narath, 5000
J. H. Scott, 5700
G. E. Brandvold, 5710

R. H. Braasch, 5712
R. P. Stromberg, 5717
T. B. Cook, Jr., 8000
L. Gutierrez, 8100
A. N. Blackwell, 8110; Attn: A. F. Baker, M. Abrams, 8111
C. S. Hoyle, 8113
D. E. Gregson, 8150
R. A. Baroody, 8160
C. S. Selvage, 8180
R. J. Tockey, 8181
D. N. Tanner, 8182
R. I. Peterson, 8183
A. C. Skinrood, 8184 (60)
T. D. Brumleve, 8184
C. M. Potthoff, 8185
C. H. DeSelm, 8200
B. F. Murphey, 8300
R. H. Meinken, 8310; Attn: D. R. Adolphson, 8312
J. H. Swisher, 8313
D. K. Ottesen, 8313
T. S. Gold, 8320, Attn: R. L. Rinne, 8321
J. D. Hankins, 8322
G. W. Anderson, 8330
J. L. Wirth, 8340; Attn: E. H. Barsis, 8342
J. F. Barham, 8360

W. C. Scrivner, 8400
R. D. Cozine, 8410; Attn: R. M. Hargreaves, 8413
L. E. Davies, 8420; Attn: M. O. Jones, 8423
G. C. Newlin, 6011 (3)
Technical Publications and Art Division, 8265, for T. I. C (2)
F. J. Cupps, 8265/Library Systems and Technical Processes Division, 3141
Library Systems and Technical Processes Division, 3141 (4)
Library and Security Classification Division, 8266-2 (5)

SUBSEQUENT DISTRIBUTION - April 9, 1975

T. Brumleve, 8184 (80)

Org.	Bldg.	Name	Rec'd by*	Org.	Bldg.	Name	Rec'd by*

*Recipient must initial on classified documents.